FERMILAB-THESIS-1994-21

UR-1349
ER-40685-799

The Charge Asymmetry in W Boson Decays Produced in $p\overline{p}$ Collisions

by

Mark Dickson

Submitted in Partial Fulfillment

of the

Requirements for the Degree

Doctor of Philosophy

Supervised by Professor A. Bodek

Department of Physics and Astronomy

College of Arts and Science

University of Rochester

Rochester, New York

1994

Curriculum Vitae

The author was born in Fort Lauderdale, Florida · He graduated with a Bachelor of Science degree in 1987 from the University of California at Davis where he spent the following year working for the High Energy Physics department on the AMY experiment at the TRISTAN accelerator at KEK. In the fall of 1988 he entered the University of Rochester where he continued working on the AMY experiment for the first couple years of his graduate carreer in Particle Physics. After receiving his M.A. in 1990 he joined the CDF experiment at the Tevatron accerator at Fermilab where he finished his PhD work under the supervision of Prof. Arie Bodek.

Acknowledgements

The primary inspiration for this analysis was my advisor Arie Bodek. He was able to see, early on, that this analysis, which did not look very promising based on earlier results, had a real potential to contribute to our understanding of the proton's structure. I also appreciated that he allowed me the freedom to find my own way through the details, concentrating on helping me to understand the relevance of the results in the context of the existing data on this subject. And last (and perhaps least), Arie proved to be an ideal advisor when it came to the onerous task of proofing the thesis, doing it in what may well be record time and all at long distance.

Also I would like to thank all the people working on the W mass measurement at CDF. In particular, Dr. Young-Kee Kim was always willing to spend time discussing the technical problems of W identification, and Randy Keup, a fellow graduate student, was a great help with the muon related portion of this analysis.

Additionally, many people helped to make my life as new father who happened to be graduate student, not necessarily the easiest situation to find oneself in, more pleasant. Kaori Maeshima provided us with everything from a table to eat on to warm clothes for our children to wear when we first arrived in Chicago. Jim and Hanna Volk, who I knew from my years as an undergraduate in California, were also very generous, going so far as to give us our first christmas tree.

Finally I would like to thank my entire family for their support, particularly in the last four years. They always gave me a sense of security which was very important after the children were born. And both Heidrun's and my parents have also been an immense

help just by giving us a place to go for a vacation, allowing us to unwind and spend more time together.

Heidrun, thank you for being so patient and understanding. Laura and Rebecca, sorry I was gone so much of the time while I worked on this thesis; hopefully by the time you can read this you will have long forgotten this period of our life.

Abstract

The charge asymmetry as a function of lepton rapidity, $A(y)$, has been measured at $\sqrt{s} = 1.8$ TeV for $|y| < 1.8$, using the W decays to electrons and muons recorded by the CDF detector during the 1992-93 run of the Tevatron Collider. The large sample of 19,039 $W \to l\nu$ events ($\sim 20\ pb^{-1}$ of integrated luminosity) and detector improvements have made discrimination between sets of modern parton distributions possible, for the first time, using $p\overline{p}$ collider data. The asymmetry data is sensitive to the ratio of the d/u quark momentum distributions in the proton. The data favor the most recent parton distributions and demonstrate the value of collider data in the measurement of the proton's structure. In particular it is found that of the two current sets, those of Martin, Roberts and Stirling (MRS) are favored over the sets produced by the CTEQ collaboration; this difference is seen even though both sets are found to agree, at the level of the nuclear shadowing corrections, with the recent measurements of F_2^n/F_2^p performed by NMC. This measurement probes the quark distributions to $x < 0.01$ at $Q^2 = M_W^2$, where nonperturbative effects are minimal.

Contents

Acknowledgements **iii**

1 Introduction **1**

1.1 Theoretical Overview 1

1.2 Hadronic Production of W Bosons 3

1.3 The Asymmetry's Relation to Structure Functions 6

1.4 W Boson Decay 8

1.5 Asymmetry Analysis Overview 12

2 Experimental Apparatus **14**

2.1 Tracking 17

2.2 Muon Chambers 21

2.3 Calorimetry 22

2.4 The Trigger System 27

3 Central $W \to e + \nu$ **29**

3.1 Central Electrons 29

3.2 Tracking in the Central Region 36

3.3 Central Electron Efficiencies 40

3.4 Central W Electron Backgrounds 42

3.4.1 QCD 42

3.4.2 Vector Boson 46

3.5 Central High P_T Electron Triggers 48

4 Plug $W \rightarrow e + \nu$ **51**

4.1 Plug Electrons 52

4.2 Tracking into the Plug Region 56

4.3 Plug Electron Efficiencies 59

4.4 Plug W Electron Backgrounds 61

4.4.1 QCD 61

4.4.2 Vector Boson 63

4.5 Plug Electron Triggers 64

5 Central $W \rightarrow \mu + \nu$ **67**

5.1 Central Muons 68

5.2 Tracking 72

5.3 Central Muon Efficiencies 75

5.4 Central Muon Backgrounds 75

5.4.1 QCD 75

5.4.2 Cosmic Ray 77

5.4.3 Vector Boson 79

5.5 The High P_T Muon Trigger 81

6 The $W \to l + \nu$ Charge Asymmetry **83**

6.1 Detector Related Systematic Errors 85

6.2 Background Related Systematic Errors 88

6.3 The Corrected Charge Asymmetry 93

7 What the Asymmetry Says about PDFs **98**

7.1 Theoretical Predictions 98

7.2 Comparisons with Predictions 100

7.3 Measuring the Proton Structure 104

8 Conclusions **109**

A False Curvature Corrections **111**

B QCD Background Estimation **115**

C Plug Tracking Efficiency **117**

D PEM Gas Gain Stability **119**

E The CTEQ and MRS Distributions **121**

Bibliography **125**

List of Tables

1.1 The fundamental particles of the Standard Model 2

2.1 Summary of CDF calorimeter properties 22

3.1 $Z \rightarrow e^+e^-$ i.d. cuts for tracking studies. 38

3.2 Central Electron Tracking Efficiencies 39

3.3 Central Electron i.d. Efficiencies 40

4.1 Plug Tracking Efficiency 58

4.2 Plug Electrons i.d. Efficiencies. 59

5.1 Central μ Stub Finding. 74

5.2 Central μ i.d. Efficiencies. 75

6.1 Plug Trigger Corrections 86

6.2 Summary of Backgrounds 88

6.3 Total Number of W Candidates 94

6.4 Charge Asymmetry and Associated Errors 94

7.1 χ^2 Comparisons 104

A.1 ϕ Dependent Correction Coefficients 113

List of Figures

1.1 $p\overline{p} \rightarrow W^+X$ 4

1.2 $W^{\pm} \rightarrow l^{\pm}\nu$ 9

1.3 W versus Lepton Charge Asymmetry 11

1.4 Charge Asymmetry Predictions 12

2.1 Layout of Fermilab 15

2.2 The Detector 16

2.3 CTC Endplate 17

2.4 CTC Event Display 18

2.5 Central Calorimeter Wedge 23

2.6 Plug Calorimeter Quadrant 24

2.7 Plug Calorimeter Proportional Tubes 25

2.8 Calorimetry Event Display 26

3.1 Central-Central $Z \rightarrow ee$ 31

3.2 Central $W \rightarrow e\nu$ M_T Spectrum 37

3.3 Charge Independence of Tracking in the Central Region 39

3.4 Central e i.d. variables 41

3.5 Central e QCD background 44

3.6 Photon Conversions 45

3.7 Central $\not\!\!E_T$ Trigger 48

3.8 Central Track Trigger 49

3.9 Central $W \rightarrow e\nu$ Trigger 50

4.1 Central-Plug $Z \rightarrow ee$ 54

4.2 Plug $W \rightarrow e\nu$ M_T Spectrum 57

4.3 Charge Independence of Tracking into the Plug 58

4.4 Plug e i.d. variables 60

4.5 Plug e QCD background 62

4.6 Plug Electron Trigger 64

4.7 Central $\not\!\!E_T$ Trigger 65

5.1 J/ψ *and* $\Upsilon \rightarrow \mu\mu$ Mass Spectra 69

5.2 Central $W \rightarrow \mu\nu$ M_T Spectrum 73

5.3 Charge Independence of Tracking in the Central Muon Sample 74

5.4 Central μ i.d. Variables 76

5.5 Central μ Cosmic Ray and QCD Background 78

5.6 Central Muon Trigger 81

6.1 Plug Trigger Effect 85

6.2 Detector Effects 87

6.3 $W \rightarrow \tau\nu$ Charge Asymmetry 90

6.4 Lost Z Charge Asymmetry 91

6.5 Asymmetric Backgrounds 92

6.6 The Uncorrected Charge Asymmetry 95

6.7 The Charge Asymmetry from Run 1a 96

7.1 NLO Compared to LO Calculations 99

7.2 Comparisions with Different PDF's Predictions 101

7.3 Comparisions with Recent PDF's Predictions 102

7.4 Lepton-W Rapidity 105

7.5 d/u and F_2^n/F_2^p 106

7.6 d/u and F_2^n/F_2^p from Recent PDF's 108

A.1 False Curvature Effects 112

B.1 QCD Background Estimation Stability 116

C.1 Plug Tracking Efficiency 118

D.1 Stability of the Plug Gas Gain 120

E.1 MRS D_0' and CTEQ 1M 122

E.2 MRS D_-' and CTEQ 2MS 123

E.3 MRS H and CTEQ 2M 124

Chapter 1

Introduction

1.1 Theoretical Overview

Since its introduction the quark model of Gell-Mann [1] and Zweig [2] has enjoyed considerable success. Today the existence of the "up" (u), "down" (d), "strange" (s), "charm" (c) and "bottom" (b) quarks is virtually indisputable, and it is generally accepted that the sixth and final quark (if every quark doublet has a massless neutrino associated with it [3]) will be discovered in the upcoming runs of the Tevatron at Fermilab.

The Standard Model of Particle Physics describes all fundamental interactions except gravity, which is too weak to play a significant role in short range particle interactions. This model is a collection of related theories; Quantum Chromodynamics (QCD) [4, 5, 6, 7], which describes the interaction of the quarks, and the Glashow-Weinberg-Salam [8, 9, 10] theory of Electroweak (EWK) interactions, which unifies quantum electrodynamics (QED) and the weak nuclear interaction. In this theory all matter is composed of quarks and leptons (spin 1/2 fermions), which interact via the

Fundamental Particles							
Fermions							Bosons
Quarks			Q ($\|e\|$)	Leptons			Q ($\|e\|$)	$W^{\pm}, Z^{o}, \gamma,$
u	**c**	**t**	$+2/3$	$\nu_{\mathbf{e}}$	ν_{μ}	ν_{τ}	0	8 gluons (g)
d	**s**	**b**	$-1/3$	**e**	μ	τ	-1	Higgs (H)
• Quarks and gluons carry color (R,G,B)								
• Leptons, $W^{\pm}$,Z^{o}, γ are colorless								
• The quarks and leptons also have antiparticle counterparts								

Table 1.1: The fundamental particles of the Standard Model grouped by generation. Only the existence of the top quark and the Higgs boson remain in doubt.

spin 1 gauge bosons. Table 1.1 illustrates the manner in which the various fermions are grouped into families within the Standard Model. To date there have been no experimental tests which the Standard Model has not passed with flying colors.

The existence of structure within the proton was established in the early 1970's by the deep inelastic scattering experiments (DIS) performed at the Stanford Linear Accelerator Center. Subsequent experiments have verified the existence of all the leptons and quarks, with the exception of the top quark. DIS experiments also indicate that about half the momentum of the proton is carried by chargeless particles, the gluons. The most direct evidence for the existence of the gluon comes from e^+e^- colliders. At high center-of-mass energies the interaction $e^+e^- \rightarrow q\overline{q} \rightarrow$ *hadrons* gives rise to jets of particles. There are distinct categories of final states with two or more jets apparent in the detector. The existence of three jet events is explained by the bremsstrahlung of a hard gluon from either the q or $\overline{q}$. Particles such as the Δ^{++} (uuu) reveal another feature of the strong interaction. If the Pauli Principle is not to be violated, the Δ^{++} implies that each flavor of quark has an additional degree of freedom. Independent evidence of the existence of this degree of freedom (first proposed by O.W. Greenberg [11] and

referred to as color) comes from the exactly calculable decay $\pi^{\circ} \rightarrow \gamma\gamma$ and the ratio $R = \frac{\sigma(e^+e^- \longrightarrow hadrons)}{\sigma(e^+e^- \longrightarrow \mu^+\mu^-)} = 3\Sigma Q_q^2$ measured at e^+e^- colliders (ΣQ_q^2 is the sum of the square of the quarks' charge).

QCD, the theory of quarks and gluons, unlike its counterpart QED, is a non-abelian theory. This results in the incalculability by means of perturbation expansions of many fundamental quantities. It is therefore necessary to include in any perturbative QCD calculation of a physical quantity certain parameters coming from experiments. One such set of parameters which must be measured are the parton distribution functions (PDF's). These functions are parameterizations of the momentum distribution of the constituent quarks and gluons in a hadron. Typically these distributions are measured in deep inelastic scattering experiments where a high energy lepton is scattered off a nuclear target. At center of mass energies high enough to permit the production of the intermediate vector bosons, another method of studying the quarks' momentum distribution functions becomes available.

1.2 Hadronic Production of W Bosons

In order to calculate the cross section for any process at a hadron collider it is necessary to convolute the partonic cross section with the momentum distributions of the partons within the proton. The generic $p\overline{p}$ cross section can be written as,

$$\sigma_{tot}(P + \overline{P} \rightarrow X) = \sum_{ij} \int dx_i dx_j f_P^i(x_i) f_{\overline{P}}^j(x_j) \hat{\sigma}(p_i p_j \rightarrow X)$$

where the sum is over all possible partons; $\hat{\sigma}(p_i p_j \rightarrow X)$ is the cross section for parton

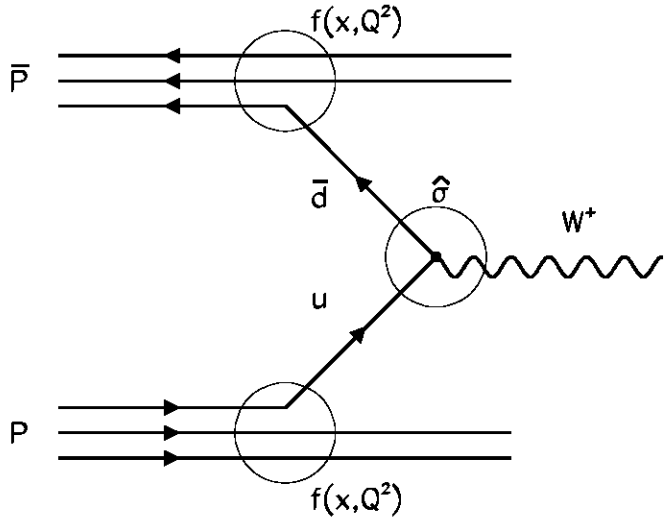

Figure 1.1: A leading order graph for the process $p\overline{p} \rightarrow W^+X$. $\hat{\sigma}$ is the partonic cross-section and f(x,Q^2) is the parton distribution function.

i with momentum p_i and parton j with momentum p_j to create X, and $f(x_k)$ is the probability of finding parton k in the proton carrying a momentum fraction of $x_k = p_k/P_{proton}$. The $f(x_k)$ distributions are different for the various partons (gluons and quark flavors) and are a function of $x = p/P_{proton}$ and Q^2 (the square of the momentum transfer). These functions are measured at low Q^2 and then evolved to higher Q^2 using the Alterelli-Parisi equations.

At a $p\overline{p}$ collider, the W boson is primarily produced by the interaction of a u and d quark ($u + \overline{d} \longrightarrow W^+$ or $\overline{u} + d \longrightarrow W^-$). At lowest order the differential cross section for W^+ production is:

$$\frac{d\sigma}{dy}(p\overline{p} \rightarrow W^+X) = K(y)\frac{2\pi G_F}{3\sqrt{2}}x_1x_2\{u(x_1)d_c(x_2) + \overline{d_c}(x_1)\overline{u}(x_2)\}$$

where

$$d_c(x) = d(x)cos\theta_c + s(x)sin\theta_c$$

and y is the rapidity of the W, $y = \frac{1}{2}\ln\left(\frac{E+P_z}{E-P_z}\right)$ (with $+z$ defined in the proton direction), G_F is the weak coupling constant, θ_c is the Cabibbo angle, and partons from the proton (antiproton) carry momentum fraction x_1 (x_2). The functions $u(x)$, $d(x)$ and $s(x)$ are the quark momentum distributions evaluated at $Q^2 = M_W^2$. $K(y)$ [12] is the so-called K-factor and includes higher-order QCD corrections similar to the Drell-Yan K-factor. Over the rapidity range $0 < |y| < 2.5$, $K(y)$ is basically independent of y,

$$K(y) \simeq 1 + \frac{8\pi}{9}\alpha_s(M_W^2)$$

where $\alpha_s(M_W^2)$ is the running strong coupling constant evaluated at $Q^2 = M_W^2$. The kinematic constraints:

$$x_1 x_2 = \frac{M_W^2}{s}$$

and

$$x_1 - x_2 = X_W$$

when combined with the definition of rapidity lead to the following relationship between x_1, x_2 and y (the rapidity at which the W is produced)

$$x_{1,2} = \frac{M_W}{\sqrt{s}}e^{\pm y}$$

where $\sqrt{s} = 2E_{beam}$. These relationships make it clear that the measurement of the

rapidity distribution of the W's produced at a collider gives fairly direct information on the differences between the u and d quark distribution functions.

1.3 The Asymmetry's Relation to Structure Functions

Modern parton distribution functions (PDF's) are determined by fitting existing deep inelastic scattering data, which was taken over many years by many different experiments. To better understand how the charge asymmetry relates to the momentum distributions of the proton's constituent quarks, it is convenient to make a few approximations. The W production charge asymmetry is defined as:

$$A(y_W) \equiv \frac{\sigma_W^+(y) - \sigma_W^-(y)}{\sigma_W^+(y) + \sigma_W^-(y)},$$

where $\sigma_W^{\pm}(y)$ is the cross section for W^+ or W^- as a function of W rapidity. If one assumes an SU(2) symmetric sea ($\overline{u}(x) = \overline{d}(x) = s(x) = \overline{s}(x)$) one finds [15, 16]:

$$A(y_W) \simeq \frac{u_1 d_2 - d_1 u_2}{u_1 d_2 + d_1 u_2 + 2 s_1 s_2} \simeq \left(\frac{u_1 - d_1}{u_1 + d_1}\right) - \left(\frac{u_2 - d_2}{u_2 + d_2}\right), \tag{1.1}$$

where $u_1 \equiv u_{val}(x_1) + s(x_1)$ etc., $x_{1,2} = \frac{M_W}{\sqrt{s}} e^{\pm y}$, and the parton distributions are evaluated at $Q^2 = M_W^2$. Making the approximation $\frac{u-d}{u+d} \simeq 1 - 2d(x)/u(x)$ (where terms of order $d^2(x)/u^2(x)$ and higher have been dropped) one finds:

$$A(y_W) \simeq 2\left(\frac{d_2}{u_2} - \frac{d_1}{u_1}\right) \tag{1.2}$$

Therefore $A(y_W)$ is related to the slope of the $d(x)/u(x)$ ratio at low x and high Q^2.

Currently the main source of information on the $d(x)/u(x)$ ratio in the x range of 0.01-0.3 (the range over which W production at the Tevatron occurs) comes from the measurement of $F_2^n/F_2^p = 2F_2^d/F_2^p - 1$ [13] (where what is actually measured is the structure function F_2 of deuterium and hydrogen). This ratio has been measured very accurately, but there are uncertainties due to higher twist at low Q^2 and shadowing effects in the deuteron [14]. As shown in [15, 16]:

$$1 - \frac{F_2^n}{F_2^p} \simeq \left(\frac{u-d}{u+d}\right) B,$$

where $B \simeq 1$ in the x region in which W's are produced at the Tevatron. When this approximate identity is combined with Eq. (1.1) one finds that:

$$A(y_W) \simeq B \left[\frac{F_2^n(x_2)}{F_2^p(x_2)} - \frac{F_2^n(x_1)}{F_2^p(x_1)}\right], \tag{1.3}$$

i.e. the asymmetry is approximately equal to the slope of F_2^n/F_2^p. One should keep in mind that this relation only holds for an SU(2) symmetric sea. The F_2^n/F_2^p measurement by the New Muon Collaboration (NMC) has been used to compute the Gottfried sum [17], which under the assumption of isospin symmetry between the proton and the neutron is:

$$S_G = \frac{1}{3} + \frac{2}{3}\int_0^1 [\overline{u}(x) - \overline{d}(x)]dx,$$

where $\overline{u} \equiv \overline{u}^p = \overline{d}^n$ and $\overline{d} \equiv \overline{d}^p = \overline{u}^n$ [18]. If the assumption of an SU(2) symmetric sea is valid then $S_G = \frac{1}{3}$. However, NMC found that $S_G = 0.240 \pm 0.016$, indicating $\overline{u}(x) \neq \overline{d}(x)$, so one can expect the relation 1.3 not to hold exactly. Therefore, in comparisons

between measurements and theory predictions, the full NLO calculations will be used. Eq. (1.2) shows that $A(y)$ is related to the slope of the $d(x)/u(x)$ ratio in a region of x which has only recently become accessible via the F_2^p and F_2^d measurements by NMC. However, the asymmetry measurement has an advantage; it probes the structure functions at high Q^2, where nonperturbative effects are negligible.

1.4 W Boson Decay

Since the W is extremely short lived, one must identify it by the products of its decay. The largest fraction of the cross section is $W \to q + \overline{q}$, but because of the large QCD background it it not practical to make use of this part of the cross section. At CDF W's are found primarily by their decay $W \to e + \nu$ and $W \to \mu + \nu$. The W decays to the third lepton, τ, are also observed; however there are large backgrounds. For this reason only the leptonic decays into e and μ are used in the asymmetry analysis.

When W production involves a valence quark (as do ~85% of the W's produced at the Tevatron), the W is polarized in the $\overline{p}$ direction. This polarization, in combination with the V-A nature of the W decay, results in a lepton angular distribution

$$\frac{d\hat{\sigma}}{d\cos\hat{\theta}} \sim (1 + \cos\hat{\theta})^2,$$

where $\hat{\theta}$ is the angle between the electron (positron) and the proton (antiproton) directions in the W rest-frame. The V-A description of weak interactions has been tested in recent $\mu \to e\nu\nu$ decay experiments [19], as well as compared to data from $W \to e + \nu$ decays at UA1 [20], and found consistent with the data. The transformation into the

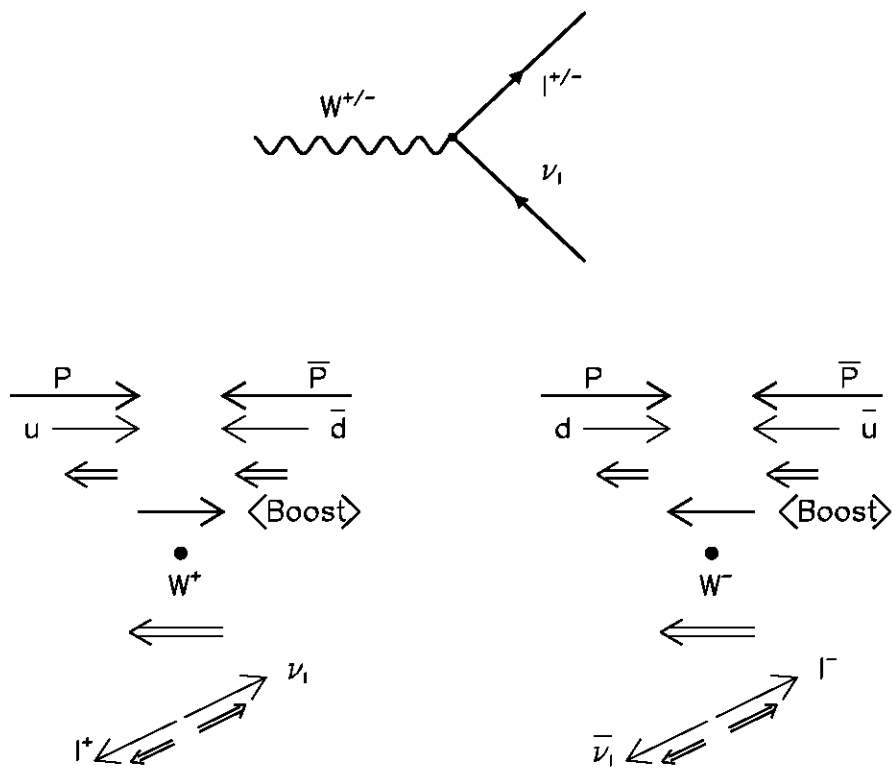

Figure 1.2: $W^{\pm} \to l^{\pm}\nu$. Arrows represent momenta and double arrows represent helicities (spin in the case of the W).

W's rest frame requires full knowledge of the electron's and neutrino's momentum. At a hadron collider only the transverse component of the neutrino's momentum is well measured; thus UA1 used the constraint $M_W^2 = (E_l + E_\nu)^2 - (P_l + P_\nu)^2$ to calculate P_z^ν assuming the mass of the W. This constraint gives two solutions for P_z^ν; at CERN energies the correct solution was usually the smaller of the two. At the Tevatron however, the two solutions are equally likely, so it is not possible to transform into the W rest frame. Therefore it is necessary to study not the W asymmetry but the lepton asymmetry observed in the lab frame. In the W rest frame, the differential cross section

for the process $u\overline{d} \to l^+\nu$ can be written as:

$$\frac{d\hat{\sigma}}{d\cos\hat{\theta}} = \frac{|V_{ud}|^2}{8\pi}\left(\frac{G_F M_W^2}{\sqrt{2}}\right)^2 \frac{\hat{s}(1+\cos\hat{\theta})}{(\hat{s}-M_W^2)^2 + (,_W M_W)^2},$$

where $\hat{s}$ is the subprocess kinematic invariant $\hat{s} = (u+\overline{d})^2$, $\hat{\theta}$ is the angle between the $\overline{d}$ and the e^+ (in the W rest frame), V_{ud} is the KM matrix element and $,_W$ is the W width. In terms of pseudo-rapidity of the W^+ decay lepton[1] ($\eta_l = 1/2\ln\left(\frac{|\vec{P}|+P_z}{|\vec{P}|-P_z}\right)$) in the lab frame, the angular distribution is:

$$\frac{d\sigma^+(\eta_l)}{d\eta_l} = 1/3\int_0^1 dx_1 \int_0^1 dx_2 \{u(x_1)d_c(x_2) + \overline{d_c}(x_1)\overline{u}(x_2)\}\left[\frac{d\hat{\sigma}}{d\cos\hat{\theta}}\sin^2\hat{\theta}\right], \qquad (1.4)$$

where η_l is related to $\hat{\theta}$, x_1 and x_2 by:

$$\eta_l = -\ln(\tan(\frac{\hat{\theta}}{2})) + 1/2\ln(x_1/x_2).$$

So the lepton rapidity measured in the lab frame is the sum of the rapidity due to the V-A decay of the W and the rapidity due to the boost imparted to the W by the difference in the u and d quark momentum distributions (see Figure 1.2). It is known from DIS measurements that the u quark momentum distribution is harder than that of the d quark, so a W^+ produced by a $u\overline{d}$ interaction has, on average, a boost in the proton direction, opposite to the direction favored by the V-A decay.

Figure 1.3 shows the effect of measuring the asymmetry of decay leptons rather

[1]For W decay leptons $\eta \approx y$ is a very good approximation because their energy is much greater than their mass. In general $\eta = y$ will be assumed for high P_T electrons and muons.

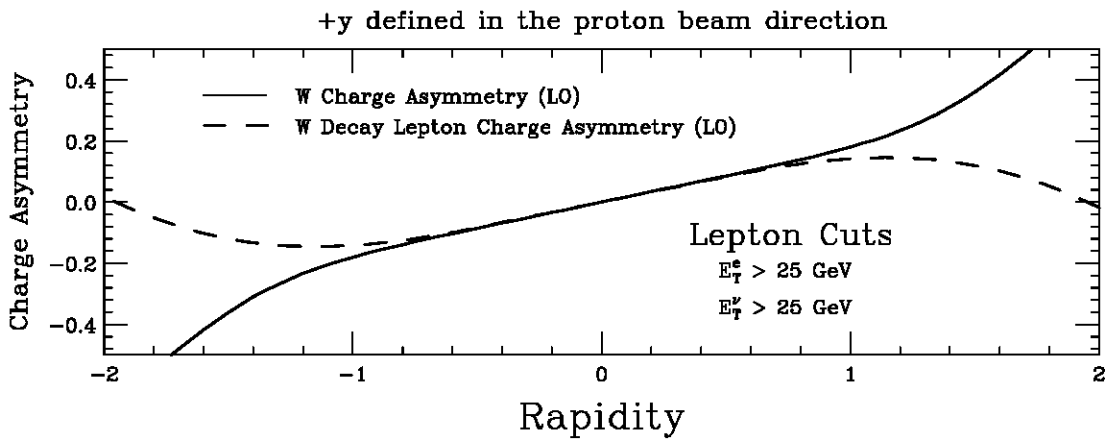

Figure 1.3: The W asymmetry is a function of only y and $\sqrt{s}$. The lepton asymmetry is additionally a function of the kinematic cuts used to select the events.

than the W's directly. It should be noted that while the W production asymmetry is a function only of y_W and $\sqrt{s}$, the lepton charge asymmetry is additionally a function of the kinematic cuts (on the transverse momentum of the leptons) used to select the events. This sensitivity comes about through the dependence of Eq. (1.4) on $\hat{\theta}$. The symmetry about $y = 0$, $A(y) = -A(-y)$, is due to CP invariance, and in future plots only $A(y > 0)$ will be shown.

In principle, the asymmetry of the decay leptons carries as much information on the momentum distribution of the quarks as does the W production asymmetry, because the W couplings are well known. Figure 1.4 shows the variation in predicted lepton charge asymmetries (calculated using the Dyrad program [21]) given by various sets of PDF's. Also shown (for the MRS D_0' PDF) is the effect of varying the coupling constants of the W to their 90% C.L. limits [22]. It is clear that any discrepancy found in this analysis, between the measured charge asymmetry and that which is predicted, can be attributed

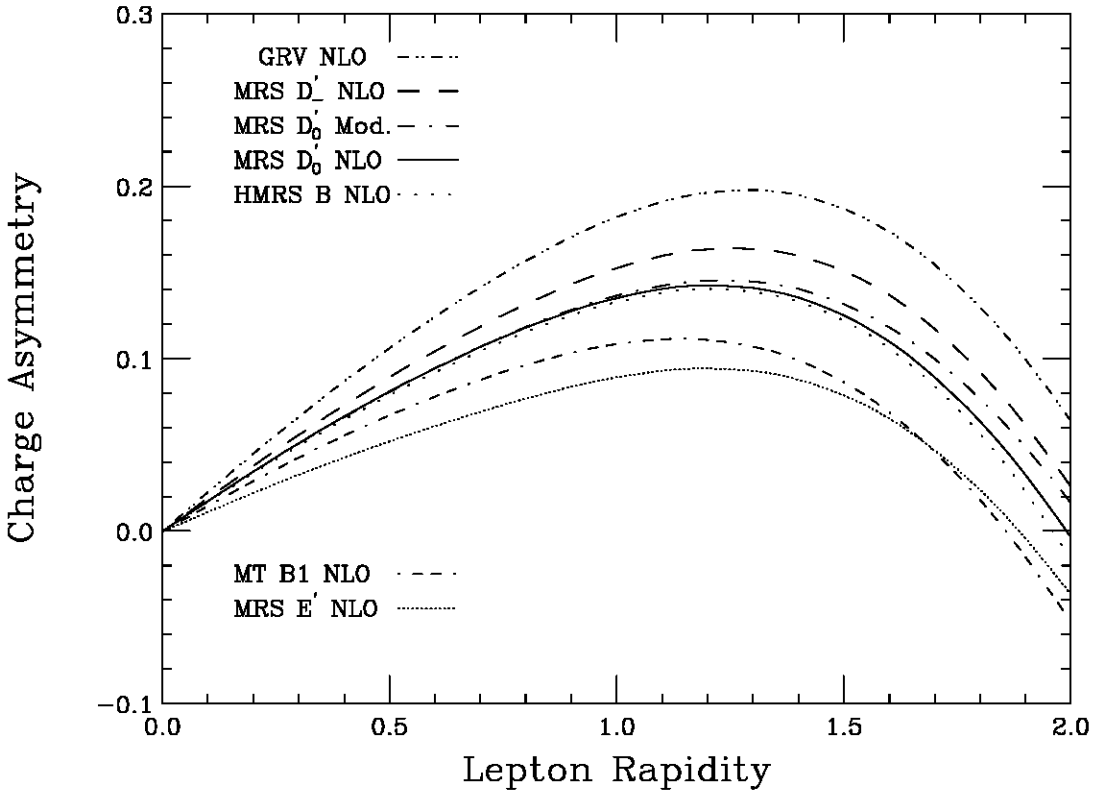

Figure 1.4: The variation due to choice of PDF. All calculations are done to NLO using the standard W couplings except for the curve MRS D_0' *Mod.* which shows the effect of allowing the W coupling constants to go to their 90% C.L. limits.

entirely to the PDF's used in the calculation.

1.5 Asymmetry Analysis Overview

After a brief discussion of the various detector components used in the asymmetry analysis, the data sets are defined and the backgrounds in each determined. The data was divided by the detector subsystem in which the lepton (either electron or muon) was found, because the selection criteria and the backgrounds differ due to various detector characteristics.

The lepton charge asymmetry is defined as:

$$A(y_l) = \frac{d\sigma^+/dy_l - d\sigma^-/dy_l}{d\sigma^+/dy_l + d\sigma^-/dy_l}, \tag{1.5}$$

where $d\sigma^+$ ($d\sigma^-$) is the cross section for W^+ (W^-) decay leptons as a function of lepton rapidity (positive rapidity is defined in the proton beam direction). As long as the acceptance and efficiencies for detecting l^+ and l^- are equal, this ratio of cross sections becomes simply the difference in the number of l^+ and l^- over the sum (all efficiencies and acceptances as well as the luminosity cancel). Further, because the asymmetry at positive rapidity is equal in magnitude and opposite in sign to that at negative rapidity, the value at positive eta is combined with that at negative eta, reducing the effect of any overall differences in the efficiencies for l^+ and l^-. The asymmetry is calculated after small corrections due to the backgrounds and detector effects have been determined.

The interest in this analysis lies in its connection to the parton distributions, so comparisons will be presented with the next-to-leading order theory predictions. Conclusions on the relative accuracy of the u and d quark distributions, which have been derived from essentially the same sets of modern DIS data, will be reached and the outlook for this and similar analyses discussed.

Chapter 2

Experimental Apparatus

The analysis described in this thesis was made using data gathered by the CDF detector during the 1992-93 run of the Tevatron collider at Fermilab. The CDF detector is a general purpose detector, symmetric azimuthally and longitudinally, designed to study the physics of high energy $p\overline{p}$ collisions. These collisions are provided by the Tevatron, a synchrotron two kilometers in diameter utilizing a ring of superconducting magnets. It does not operate alone, but is the final stage of a process composed of many individual accelerators. Figure 2.1 gives an overview of the various machines used to accelerate, store and collide the beams of protons and antiprotons at Fermilab. At the beginning is a bottle of hydrogen gas; at the end are the highest energy (900 GeV) protons and anti-protons available at any laboratory. The acceleration chain begins with doubly charged negative ions which are accelerated by a Cockcroft-Walton electrostatic accelerator to 750 KeV. The electrons are then stripped from the hydrogen ions and the protons transferred to a 500 ft. linear accelerator (LINAC) where they acquire 200 MeV and are sent on to the Booster Ring. This ring is a synchrotron of diameter 500 feet

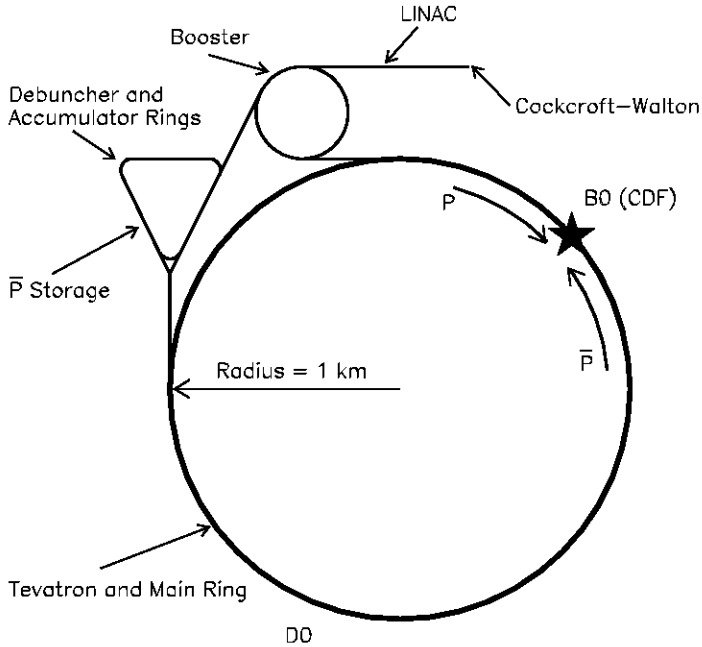

Figure 2.1: A schematic diagram of the layout of the various accelerators used at Fermilab to provide $p\bar{p}$ collisions at a center of mass energy of 1.8 TeV.

which boosts the protons to 8 GeV. At this point the protons are injected into the Main Ring, a two kilometer diameter synchrotron, composed of conventional magnets. The Main Ring increases the protons' energy to 150 GeV and then either transfers them to the Tevatron, where they are accelerated to 900 GeV, or directs them at a tungsten target for the production of anti-protons.

The anti-protons are collected in the Debuncher Ring where they are stochastically cooled before being stored in the Accumulator. Once there are a sufficient number of anti-protons cooled and stored, the $\bar{p}$ beam is transferred to the Main Ring where it is accelerated to 150 GeV and injected into the Tevatron. Both beams circulate in the same magnetic and RF fields which produce helical orbits. The beams intersect at

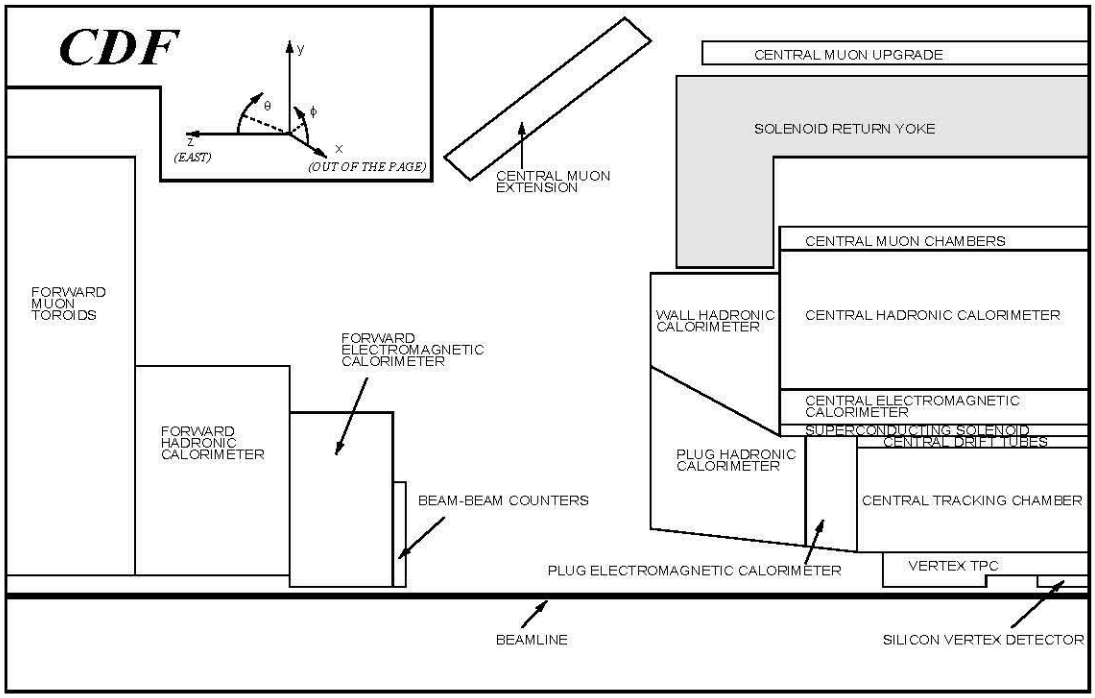

Figure 2.2: A cut-away diagram of the various components of the CDF detector (the interaction point is in the lower right corner). The coordinate system is defined by the proton beam momentum being in the $+z$ direction.

four points, but the large transverse size of the beam minimizes collisions. Quadrupole magnets are then used to focus the beams to a diameter of $\sim 40\mu m$ at the B0 and D0 collision halls, and electrostatic separators prevent collisions at the remaining collision points during normal running. The rate at which collisions between protons and anti-protons took place during the 1992-93 run was approximately five times greater than in the previous run at the Tevatron, resulting in $\sim 20\ pb^{-1}$ of data recorded by CDF at a center of mass energy of 1.8 TeV.

CDF is particularly well suited for the study of leptons with large transverse momenta. Figure 2.2 shows a cutaway view of a quarter of the CDF detector; it is essentially symmetric in ϕ and η ($\eta = -ln[tan(\theta/2)]$ where θ is measured relative to the proton

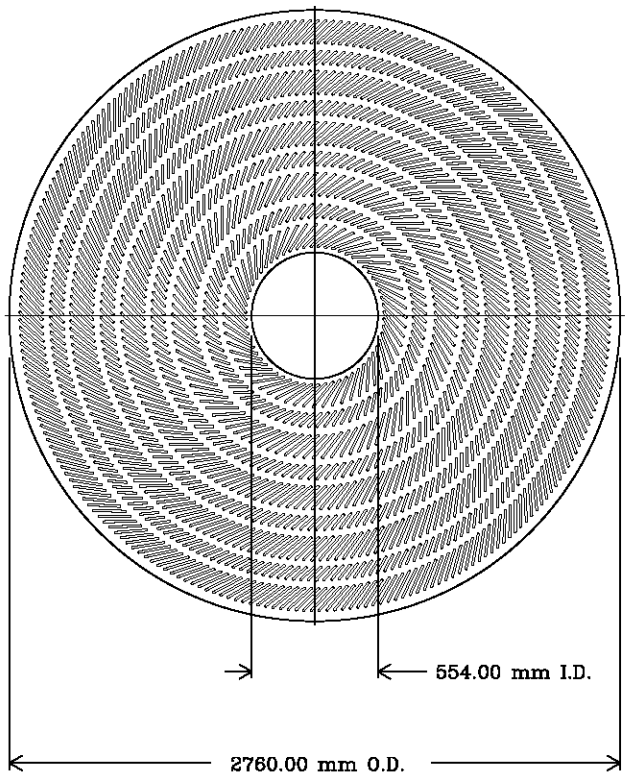

Figure 2.3: The central tracking chamber.

beam direction). The following are descriptions of the various detector elements relevant to the measurement of the W charge asymmetry. For a thorough description of CDF in its entirety see Ref. [23].

2.1 Tracking

CDF is equipped with several charged particle tracking systems which are immersed in a 1.4116 T axial magnetic field provided by a 4.8 m long superconducting solenoid of radius 1.5 m. This magnetic field is crucial for the measurement of the charge asymmetry as it enables the determination of the decay lepton's charge. It also provides a means to calibrate the central electromagnetic calorimeter, using the energy/momentum

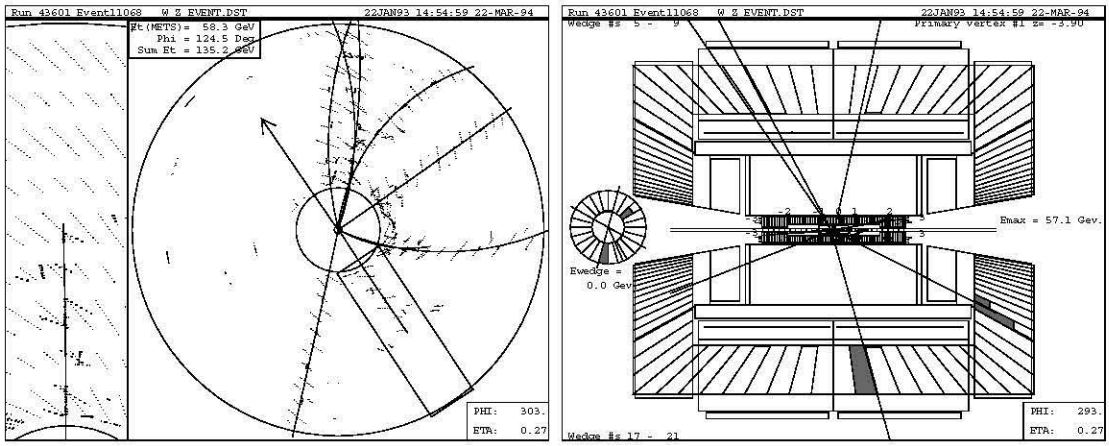

Figure 2.4: The r-ϕ and r-z view of the central tracking chamber for a WZ candidate. The arrow in the r-ϕ view indicates the direction of the $\not{E}_T$. Darkened points indicate hits on the individual wires of the CTC. The short line segment shows the track which is associated with the plug W and the leftmost window is a close-up view of this track (which exits the CTC in the fifth superlayer). The remaining two stiff tracks are consistent with the decay of a Z boson. The r-z view shows, in addition to the tracks, the energy seen by the calorimeters (the third energy cluster is not visible in this ϕ slice).

(E/P) distribution of a large number of electrons with an easily measured quantity, the magnetic field strength. The magnetic field strength is determined by the current flowing in the superconducting solenoid and is independently monitored by a NMR probe which is accurate to one part in 10^4.

The Central Tracking Chamber

In this analysis the primary limiting factor for electrons (beyond statistics) is the η coverage provided by the central tracking chamber (CTC). The CTC is a 84 layer drift chamber which has its drift cells divided into nine "superlayers". Five of the superlayers have their sense wires parallel to the beamline and interleaved with these layers are four layers with their wires at an angle, $\pm 3^\circ$, for reconstruction in the r-z view. For tracks at 90°, $\frac{\delta P_T}{P_T} = 0.0010 \times P_T$ in GeV/c and the z resolution is ~ 4 mm. Figure 2.3 shows the

pattern drilled into the endplate; the superlayers (five axial and four stereo) are clearly visible. To determine the charge of the W boson, the decay lepton must traverse three superlayers of the CTC to make a reliable determination of the track's curvature. This translates roughly into the requirement that the electromagnetic (EM) cluster have a pseudorapidity in the region $|\eta| < 1.7$. Figure 2.4 shows the CTC event display for a $W + Z \rightarrow e^+\nu_e + e^+e^-$ candidate. The curvature of the tracks in the r-ϕ view is inversely proportional to the P_T of the lepton, and tracks are straight lines in the r-z view because the magnetic field lines run parallel to the beamline. The r-z view shows the ϕ slice of the detector, which includes two of the high P_T tracks as well as the calorimeter energy clusters at which the tracks point.

The Vertex Detector

The determination of the rapidity of the leptons requires the event vertex to be well measured. This is accomplished by a vertex time projection chamber (VTX), which tracks charged particles in the r-z plane out to $|\eta| < 3.5$. The VTX is made up of eight octagonal modules with sense wires running perpendicular to the beamline. Each module is divided in two by a central high voltage grid, creating $\sim$ 15 cm long drift regions. The VTX is able to measure the z of the the interaction point, which has $\sigma = 25$ cm, to 1 mm. However, the ϕ resolution of the VTX is limited to knowing which octant the track traversed, so using it for a charge determination is impossible. The r-z view in Figure 2.4 shows the VTX as a series of vertical lines at the center of the CTC. The inner section of the VTX has a cavity built into it which contains the Silicon Vertex Detector (shown as two small rectangles located in the center of the VTX).

Silicon Vertex Detector

The Silicon Vertex Detector (SVX) consists of four layers of silicon strip detectors extending ± 25 cm in z at a radius of 2.9 to 7.9 cm just inside the VTX. The SVX plays only a peripheral role in this analysis. The beamline in a given run was determined to a very high degree of accuracy, $\sigma_{xy} = 40\ \mu m$, using a large number of tracks coming from various positions in z. This resolution in the x-y plane is not dominated by the resolution of the SVX, of order 15 μm, but is the natural spread in the proton and antiproton beams. The measurement of the beamline is important for the muon channel in particular, since the track associated with the μ is constrained, in three dimensions, to have originated from the interaction point. This additional constraint improves the track P_T resolution considerably. Beam constrained (BC) tracks are also important in the plug region as the addition of this point in the track fit, with its long lever arm, can have dramatic effects on the P_T resolution when only a few superlayers are traversed before the electron exits the CTC. The event shown in Figure 2.4 is a good example of the value of the beam constraint. The high P_T track which exits the CTC in the fifth superlayer ($\eta = 1.4$) is associated with a 25 GeV E_T EM energy cluster; its transverse momentum is determined to be 8 GeV/c without and 20 GeV/c with the beam constraint applied. Clearly the beam constraint greatly improves the momentum measurement in the plug region.

2.2 Muon Chambers

For muons the limiting factor is the coverage provided by the central muon drift chambers (CMU) and the central muon extension chambers (CMX) (see Figure 2.2). CDF has a forward muon system which covers the region $2 < |\eta| < 3.6$ and has a pair of toroids for momentum and charge determination, but because of large backgrounds and trigger inefficiencies as well as containing only a small fraction of the total W cross section, the asymmetry measurement is not performed using these data.

Central Muon Chambers

There are two sets of muons chambers in the central, $|\eta| < 0.6$, region of the CDF detector. Each consists of four layers of drift chambers which have their sense wires offset to allow resolution of the track ambiguity and determination of drift velocities. TDC's measure the azimuthal direction and η is determined by charge division. The central muon chambers (CMU) cover 85% in ϕ and are located just behind the hadronic section of the central calorimeter, which provides ~ 5 absorption lengths. The central muon upgrade chambers (CMUP) cover 80% in ϕ and are located behind ~ 8 absorption lengths of steel.

Central Extension Muon Chambers

In the region $0.6 < |\eta| < 1.0$ two pairs of free standing conical arches support the central extension muon chambers (CMX). These chambers provide coverage of 67% in ϕ and are located behind the central and wall calorimeters as well as the return yoke of the solenoid (~ 6 absorption lengths of steel). Because of a high trigger rate due to a

Calorimeter	η Coverage	Energy Resolution	Depth
CEM	$\lvert\eta\rvert < 1.1$	$13.7\%/\sqrt{E_T} \oplus 2\%$	18 X_0
PEM	$1.1 < \lvert\eta\rvert < 2.4$	$22\%/\sqrt{E} \oplus 2\%$	18-21 X_0
FEM	$2.2 < \lvert\eta\rvert < 4.2$	$26\%/\sqrt{E} \oplus 2\%$	25 X_0
CHA	$\lvert\eta\rvert < 0.9$	$50\%/\sqrt{E_T} \oplus 3\%$	4.5 λ_0
WHA	$0.7 < \lvert\eta\rvert < 1.3$	$75\%/\sqrt{E} \oplus 4\%$	4.5 λ_0
PHA	$1.3 < \lvert\eta\rvert < 2.4$	$106\%/\sqrt{E} \oplus 6\%$	5.7 λ_0
FHA	$2.4 < \lvert\eta\rvert < 4.2$	$137\%/\sqrt{E} \oplus 3\%$	7.7 λ_0

Table 2.1: CDF calorimetry is divided into EM (xEM) and hadronic (xHA) detectors, which together cover all ϕ and $|\eta| < 4.2$. The symbol $\oplus$ signifies that the constant term is added in quadrature in the resolution. Energy resolutions were determined at a testbeam using electrons for the electromagnetic calorimeters and isolated pions for the hadronic calorimeters. The "Depths" are given in radiation lengths for the electromagnetic and interaction lengths for hadronic calorimeters.

problem with the beampipe design, the CMX trigger was rate limited during the first half of the run (midway through the run the beampipe was replaced reducing the CMX triggers to a manageable rate). This problem resulted in poor statistics for this region, in the muon sample.

2.3 Calorimetry

CDF is equipped with EM and hadronic calorimeters which provide full coverage in ϕ out to $|\eta| < 4.2$. The calorimeters utilize lead as an absorber for the EM sections and iron for the hadronic sections. The active sampling medium is either scintillator, in the central region ($|\eta| < 1.1$), or gas proportional chambers in the plug ($1.1 < |\eta| < 2.4$) and forward ($2.4 < |\eta| < 4.2$) regions. Table 2.1 summarizes the properties of the various detectors of which CDF calorimetry is comprised. In the asymmetry measurement, the most prominent effect due to the construction of the calorimeters is the lack of data

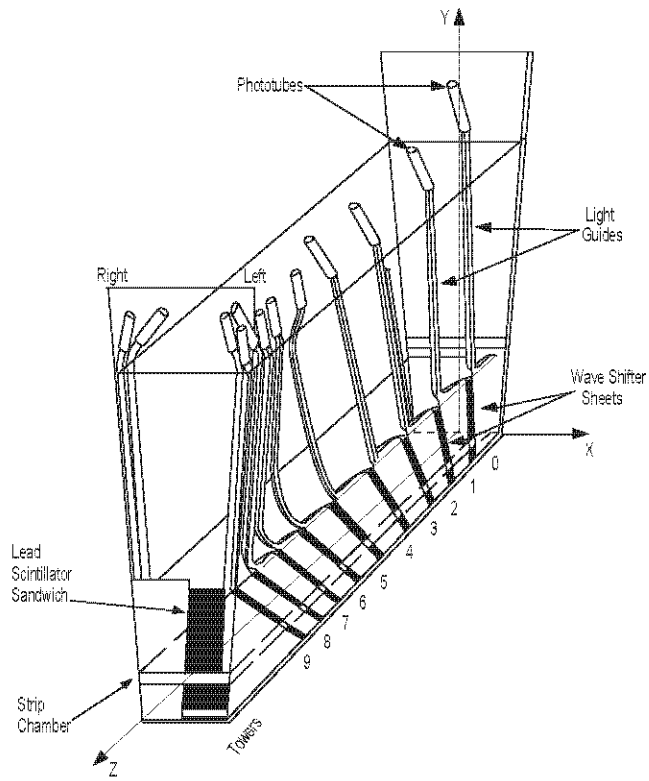

Figure 2.5: The central EM calorimeter wedge uses lead as absorber and scintillator as the active medium. It is followed by the hadronic compartment which uses iron as the absorber. The EM compartment contains a strip-wire proportional chamber which is used for position determination.

in the region $1.1 < |\eta| < 1.2$. This effect is due to the gap between the central and plug EM calorimeters. In the analysis this region's data is removed because of its poor energy resolution.

Central

The central calorimeter is made up of a series of wedges, each covering 15° in ϕ and containing an electromagnetic (CEM) section followed by a hadronic section (CHA). The EM section contains a proportional wire chamber (CES) at shower max which is used for electron identification (using the energy shower's profile) and position determination.

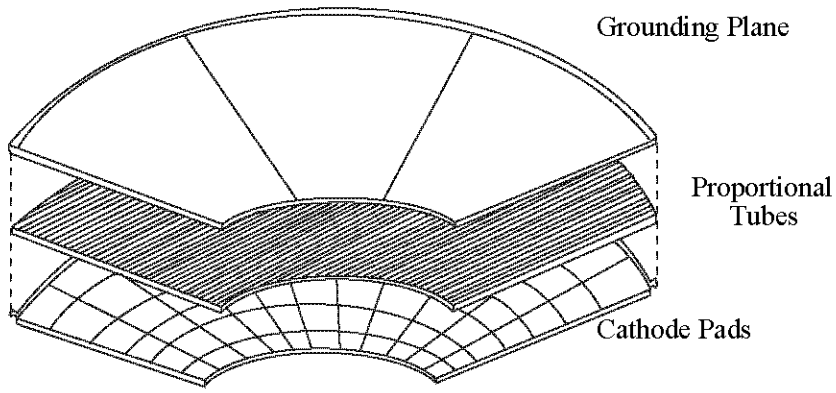

Figure 2.6: The Plug Calorimeter maintains the projective tower geometry found in the central region. The active medium is argon-ethane and the absorber is lead in the EM section and iron in the hadronic section. The gain was actively stabilized by varying the high-voltage to compensate for changes in the temperature and pressure.

Each of the wedges is divided into ten projective towers, each covering 0.1 units in $\Delta\eta$. Figure 2.5 shows the anatomy of an individual central calorimeter wedge.

To fill the gap between the hadronic sections of the central and plug calorimeters, the "End Wall" hadronic calorimeter (WHA) covers the region $0.7 < |\eta| < 1.3$. Like the central calorimetry, these calorimeters use scintillator as the active medium and are divided into towers of $15^\circ \times 0.1$ unit of η.

Plug and Forward Calorimeters

The plug EM calorimeter (PEM) is disk shaped with a diameter of 2.8 m and a depth of 50 cm. It is located 1.73 m in z from the nominal interaction point and covers $1.1 < |\eta| < 2.4$. It consists of 34 layers of proportional tubes sandwiched between lead plates. Each layer has a set of pads and anodes readout (see Figure 2.6), and ten layers have finely grained (0.01 units in $\Delta\eta$ and 1° in $\Delta\phi$) strips etched into the back of the pad G10 boards for position and shower shape determination. These strip chambers

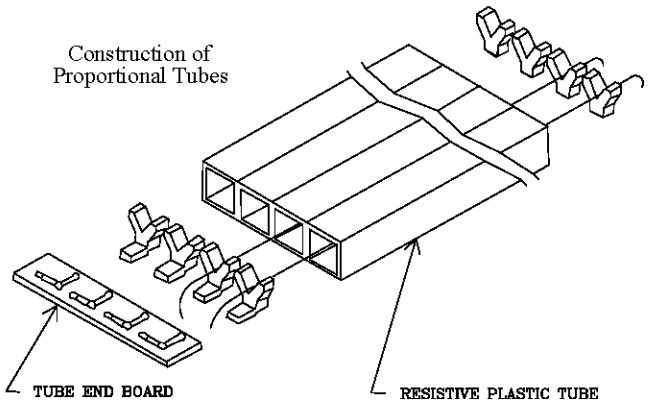

Figure 2.7: The plug calorimeters use conductive plastic proportional tubes sandwiched between 2.7 mm thick lead absorber panels. The anodes (50 μm gold-plated tungsten) of each layer are ganged together by quadrant for readout. The longitudinal energy profile in the PEM is used in the trigger and in the offline reconstruction to reject non-electron events.

(PES) extend out to $|\eta| < 1.8$ and are located at shower maximum. Since the CTC can determine the charge of tracks out to $\sim |\eta| < 1.7$, only the outer half of the PEM (which is covered by the strip chambers) will play a significant role in the measurement. The PEM is directly followed by the plug hadronic calorimeter (PHA). It too employs gas proportional tubes, and like the CHA it is important for electron/hadron separation in this analysis.

The forward calorimeters also are based on gas proportional chambers with cathode-pad readout. These chambers cover the region $2.2 < |\eta| < 4.2$; since this is well beyond the region covered by the CTC, these detectors are of only peripheral importance to the asymmetry measurement (they are used in the $\not\!\!E_T$ determination). The forward EM (FEM) and hadronic (FHA) detectors, as well as the PEM and PHA, were placed on "high-voltage feedback" to maintain a constant gain throughout the run.

"High-voltage feedback" refers to a method developed by CDF to maintain constant

gain in the gas calorimeters. The temperature and atmospheric pressure were monitored, and the high voltage applied to the calorimeters' anodes was varied automatically in such a way as to maintain a constant gas gain. This method was tested and calibrated during the 1991 testbeam.

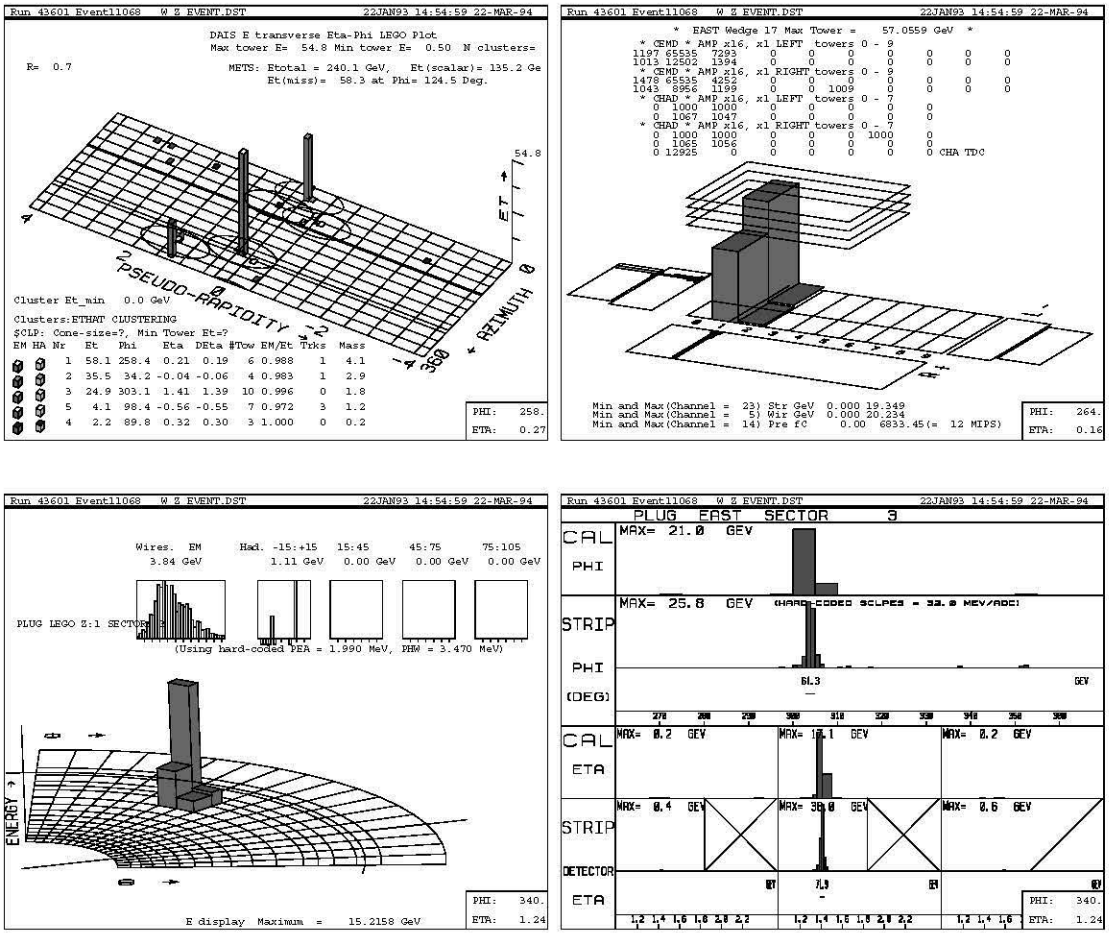

Figure 2.8: The CDF calorimeter display of the WZ candidate. The four views show the energy deposition as measured by: all the towers of the calorimeters (upper left), the two photo multiplier tubes, strip chambers and preradiator in the central wedge (upper right), the cathode pads and anode wires of a plug quadrant (lower left) and the ϕ and η shower maximum strip chamber of a plug quadrant (lower right).

Figure 2.8 shows the CDF calorimetry display for the WZ candidate. In both the central and plug regions good electrons are identified by the sharing of energy between

adjacent towers and the shower profile measured by the shower maximum detectors. Also the matching between the extrapolated track position and the position of the EM shower, as determined by the strip chambers, is used to reduce electron fakes.

2.4 The Trigger System

The CDF trigger is a three level system. The lowest level required that there be a tower in the calorimeter over a modest threshold (or hits in the muon chambers) and, in the first half of the run, that there be hits in the beam-beam counters (the position of these simple scintillator based detectors is shown in Figure 2.2). As the luminosity of the collider increased this coincidence requirement was dropped as the probability of an interaction per crossing exceeded one. At typical luminosities this trigger had an accept rate of about two kHz.

The level two trigger is a fastbus based hardware trigger system. It is at this level that the largest number of events are rejected, so careful study of its performance was necessary. In both levels one and two, towers are defined as $15^\circ \times 0.2$ unit of η. At level two, unlike level one, clusters of energy are formed by the hardware "cluster finder", and tracks reconstructed by the Central Fast Tracker (CFT). The tracks found by the CFT are matched to EM clusters in the central region or muon track segments to form the central electron and muon triggers. The CFT is only able to find tracks in the central region of the detector, so no attempt is made to match tracks with EM clusters in the plug. The cluster finder also determines the $\not{E}_T$ in the event; this is used for triggering on W's by both the central and plug electron triggers. The two kHz input

rate is reduced to about 20 Hz, and these events are passed on to the third level trigger.

The level three trigger was a silicon graphics "farm" with 1000 MIPS of computing power. It was comprised of 48 CPU's, running in parallel, each with the ability to have an event being read in or written out of its buffer space while a second event was being processed. The software run was essentially the complete offline reconstruction code with the majority of the time being taken up by the track reconstruction. The primary difference between the quantities cut on in the offline analyses and those used by level 3 were: E_T was calculated using $z = 0$ and final database constants for tracking and calorimetry were not available. The output from level three was written to 8mm tapes at about four Hz. A fraction of the events, satisfying tight cuts, was flagged for immediate offline processing. These so called "Express Stream" events were used in this analysis after reprocessing with the final database constants (at which point they were referred to as "Stream 2" events).

Chapter 3

Central $W \rightarrow e + \nu$

3.1 Central Electrons

During the course of 1992-93 run, several data sets were stripped from the data stream for immediate processing. The data used in the asymmetry analysis was from one of these "stream 2" data sets, as was the $Z \rightarrow ee$ data which was used to check the performance of the detector. The timely processing of the data allowed quick identification of problems in the reconstruction code and the detector calibration constants, allowing the analysis to be completed shortly after the data taking ended. This central $W \rightarrow e + \nu$ data set is also being used for the W mass measurement at CDF.

Energy Corrections

Several energy corrections were made to the raw energy associated with an electron striking the central calorimeter. The "mapping" correction flattened out the response of an individual tower based on the electron's position within the tower, as determined

by the CES. The mapping response functions for each tower were determined using testbeam electrons [24]. The tower-to-tower variations were determined using E/P from a large sample of central electrons taken during the run. Then, finally, the global energy scale was determined using E/P from the central $W \rightarrow e + \nu$ events, where tight quality cuts were placed on the track associated with the electron, and careful modeling of the electrons' radiation was performed. These corrections yielded an absolute energy response of the CEM to electrons of about 0.1% for the region of the CEM used in the W mass analysis [25]. Because the asymmetry is not very sensitive to the energy resolution, a looser definition of "fiducial" was used in this analysis. To check that the average energy scale was not significantly modified, Figure 3.1 shows a fit (allowing the Z width to float) to the central-central Z sample selected using the same definition of fiducial as used in the asymmetry analysis. The mean, 90.52 GeV/c^2 $\pm$ 0.15, is within 1% of the LEP value, 91.18 GeV/c^2 [26]. Since the energy scale has only a small effect on the asymmetry, the 1% offset will be taken as an error rather than a correction (the effects due to backgrounds and nonlinearities make the interpretation of the 1% as a scale correction slightly uncertain).

W Selection Criteria

E_T > 25 GeV: E_T is the clustered electron energy transverse to the beam direction,

$$E_T = \sum_i E_i sin(\theta_i)\hat{\mathbf{n}}_\mathbf{i}, \tag{3.1}$$

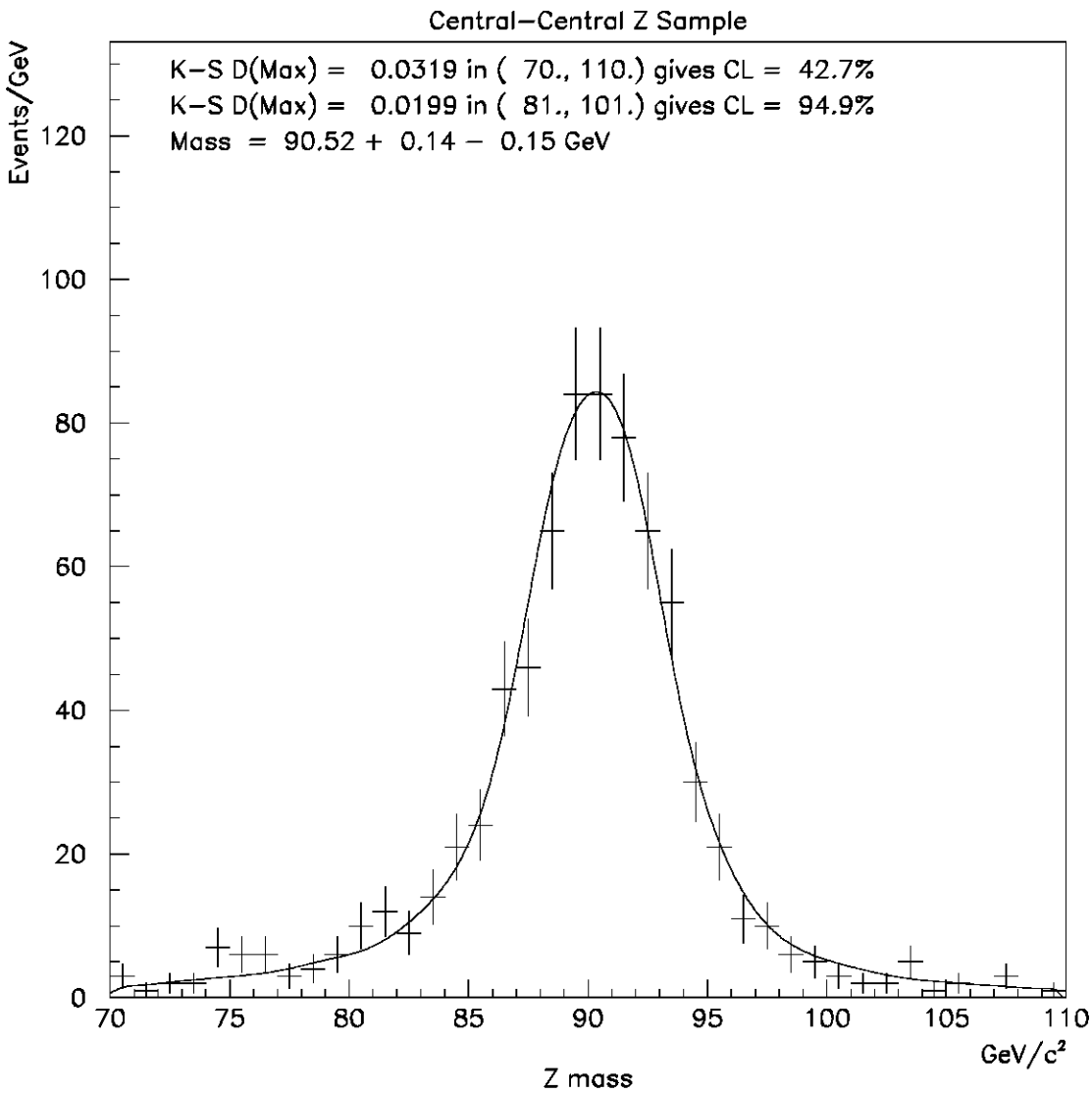

Figure 3.1: A fit for the Z mass, taking radiative corrections into account, for central-central $Z \rightarrow ee$. Also shown are the Kolmogorov-Smirnov test results for the unbinned data in the ranges $70 < Z\ mass < 110$ and $81 < Z\ mass < 101$.

where the polar angle θ_i and the unit vector in the transverse plane $\hat{\mathbf{n}}_\mathbf{i}$ are measured relative to the interaction point, determined by the VTX, and the center of the tower. The sum is over all the calorimeter towers associated with the EM energy cluster.

$\not{E}_T > 25$ GeV: $\not{E}_T$ is the missing E_T in the event defined by,

$$\vec{\not{E}}_T = -\sum_i E_T^i \hat{\mathbf{n}}_\mathbf{i}, \qquad \text{i = calorimeter tower number with } |\eta| < 3.6 \tag{3.2}$$

where $\hat{\mathbf{n}}_\mathbf{i}$ is a unit vector perpendicular to the beam axis and pointing at the ith calorimeter tower.

$E_T^{jet} < 20$ GeV: The jet energy is defined by the calorimeter energy (not associated with the electron) contained in a cone, centered on the jet centroid, of $R = 0.7$ ($R = \sqrt{(\Delta\eta)^2 + (\Delta\phi)^2}$).

$P_T^{high} < 10$ GeV: The highest P_T track not associated with the electron was required to be less than 10 GeV. This cut removes Z events as well as some QCD background.

E_{Had}/E_{EM}: The ratio of the energy in the hadronic and electromagnetic sections of the calorimeter associated with the energy cluster was required to satisfy,

$$E_{Had}/E_{EM} < 0.055 + \frac{0.045 * E\ (GeV)}{100\ GeV}, \tag{3.3}$$

where E is the total energy of the cluster. The linear term takes into account the additional leakage associated with high energy electrons.

***LShr* < 0.2:** This variable is a measure of the lateral shower profile of the electron candidate. It is defined as,

$$LShr = C \sum_i \frac{E_i - T_i}{\sigma_i} \tag{3.4}$$

where $E_i \equiv \frac{Energy\ in\ Adjacent\ Tower\ i}{Energy\ in\ Seed\ Tower}$, $T_i \equiv E_i\ from\ testbeam$ and $C \equiv Scale\ Factor = 0.14$.

***Isolation* < 0.1:** The isolation variable is a measure of the energy surrounding the electron. It is defined as,

$$Isolation = \frac{E_T(0.4) - E_T}{E_T} \tag{3.5}$$

where $E_T(0.4)$ is the energy in a cone of radius 0.4 in $\eta - \phi$ space, and E_T is the electron's transverse energy.

χ_s^2 < 10: The χ^2 of the lateral shower shape measured at shower maximum by the strip chambers was required to be consistent with 50 GeV/c electrons measured at the testbeam.

0.5 < *E/P* < 2.5: The ratio of the EM energy and the momentum of the track associated with the energy cluster was required to be consistent with that of a single charged particle. On average this is 1.0 for electrons, but because of the possibility

for the electron to radiate there is a long tail to the distribution.

15 GeV $< P_T <$ 200 GeV: The transverse momentum (P_T) was required to be consistent with a W decay electron as well as in a range where the charge can be reliably determined. P_T is measured relative to the beam line and is determined by the track's curvature in the CTC. Note: the quantities P and P_T always refer to measurements made using the CTC, while E and E_T refer to the measurements made using the calorimeters.

***CurSig* > 2.0:** The curvature significance is defined as,

$$CurSig = Cur/\sigma_{cur} \tag{3.6}$$

where Cur is the curvature of the track and σ_{cur} is the error on the curvature measurement. This cut rejects tracks whose charge determination is questionable.

$|\delta X| <$ 1.5 cm: The difference between the X ($X = R_{strip} * \phi$) position measured by the strip chambers and the extrapolation of the track from the CTC was required to be less than 1.5 cm.

$|\delta Z| <$ 3.0 cm: The difference between the Z position measured by the strip chambers and the extrapolation of the CTC track was required to be less than 3.0 cm.

$|D_0| <$ 0.2 cm: The absolute value of the impact parameter $|D_0|$ is the distance of closest approach of the track to the z-axis. This cut removes events which are not consistent with originating from the interaction region (such events are most likely decays in flight or cosmic rays).

$|Z_o| < 60$ cm: The event vertex, as determined by the VTX, was required to be within approximately 2σ of the center of the detector.

In addition, the electron candidate was required to be in the fiducial region of the calorimeter wedge, which is defined as $|z| < 230$ cm and $|x| < 21$ cm as measured by the strip detector. Also the runs were checked against a list of known bad runs (i.e. runs where there were detector or DAQ failures). This cut leaves approximately 19.6 pb^{-1} in the data set.

The previous cuts were applied to a data set, consisting of 28107 events, which had been filtered from the primary data stream by satisfying the following initial cuts on the raw (uncorrected) variables:

$E_T > 22\ GeV$

$P_T > 13\ GeV$

$E_{Had}/E_{EM} < 0.10$

$\not{E}_T > 22\ GeV$.

To study the detector, an analogous stream 2 data set of $Z \rightarrow ee$ events were used. These Z events were selected by satisfying:

First electron candidate:

Found in the CEM

$E_T > 22\ GeV$

$P_T > 13\ GeV$

$E_{Had}/E_{EM} < 0.10$

Second electron candidate:

$E_T > 20,\ 15,\ 10\ GeV$ in CEM, PEM or FEM respectively

$Isolation < 0.1$

$\chi^2_{PEM} < 3.0$ if in the PEM

$E_{Had}/E_{EM} < 0.05$.

Events in both data sets had their CTC tracks refitted after the Tevatron run was completed to take advantage of new CTC wire alignment positions, which were determined using the high statistics available from the inclusive central electron data. Figure 3.2 shows the transverse mass ($M_T^2 = 2E_T^e E_T^\nu[1 - cos\Delta\phi^{e\nu}]$, where $\phi^{e\nu}$ is the angle between the electron and neutrino) spectrum of the 10244 events which pass all the selection cuts.

3.2 Tracking in the Central Region

In the central region tracks are well identified, $\frac{\delta P_T}{P_T} = 0.0010 \times P_T$ in GeV/c at 90°; therefore the determination of the W decay lepton's charge is not expected to be a problem. To determine the probability that the track reconstruction code misidentifies the charge of the lepton in the central region, a sample of $Z \rightarrow e^+e^-$ events were selected from the stream 2 Z sample. The events passed the cuts listed in Table 3.1, plus the second electron passed the same tracking related cuts (P_T, E/P, δX, δZ, D_0, and $CurSig$) as applied to the W asymmetry data sample. These cuts provided a clean sample of Z's where the first electron was well isolated in the tracking chamber (only one track was allowed to point at the calorimeter cluster), and the second was representative of the tracks found in the W sample. None of the 648 Z candidates had two tracks of

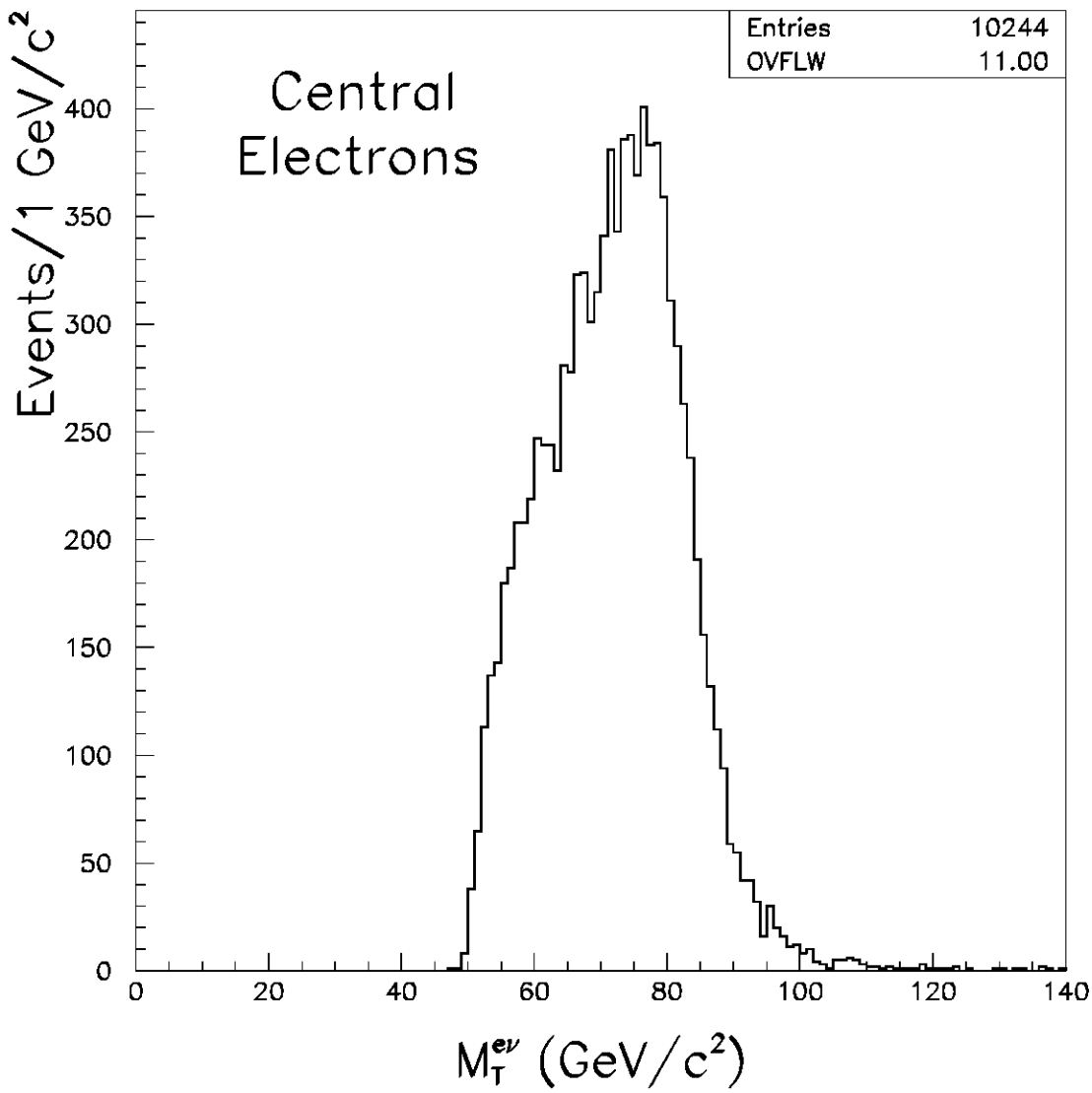

Figure 3.2: The transverse mass spectrum of the central electron W candidates to be used in the asymmetry analysis.

Variable	Cut value
Z mass	> 65 and < 115
First Leg:	
E_{Had}/E_{EM}	$< 0.055 + 0.00045 * E$
$Isolation$	< 0.1
$LShr$	< 0.2
χ^2_s	< 15
# 3d tracks [1]	$= 1$
E/P	< 2.5
δX	< 3.0
δZ	< 5.0
Second Leg:	
E_T	> 20 GeV
E_{Had}/E_{EM}	< 0.05
W track cuts	
Both legs:	
$\|Z_0\|$	< 60 cm
common vertex	$\|\Delta Z_0\| < 10$ cm
$CurSig$	< 2.0
Conversion Cut	

Table 3.1: $Z \rightarrow e^+e^-$ i.d. cuts for tracking studies.

the same charge associated with the calorimeter clusters, implying an upper limit of

$$p^{\pm} < 0.46\% \ (90\% \ C.L.) \tag{3.7}$$

on the probability of misidentifing the lepton's charge.

A charge dependence in the measurement of the P_T of a lepton can be produced by the misalignment of the CTC wires. The result of this misalignment is a "false curvature" which is systematically added to the curvature of the measured CTC tracks, thereby increasing the momentum of one charge and decreasing the momentum of the

[1] "# 3d tracks" refers to the number of 3-dimensionally reconstructed tracks which point at a calorimeter tower associated with the electron's energy cluster.

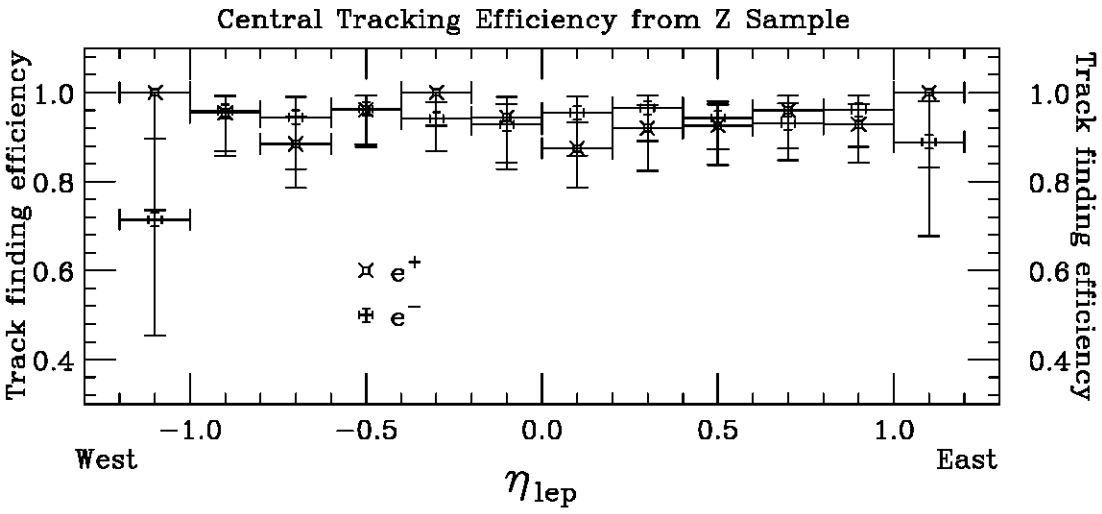

Figure 3.3: The charge independence of tracking in the central region as determined using the second (unbiased) leg of central-central Z's. The charge of the track is determined by the first leg.

	ϵ^+	ϵ^-	ϵ^{tot}
West	$95\%^{+2\%}_{-3\%}$	$93\%^{+2\%}_{-3\%}$	$94\% \pm 2\%$
East	$93\%^{+2\%}_{-3\%}$	$95\%^{+2\%}_{-3\%}$	$94\% \pm 2\%$
Total	$94\% \pm 2\%$	$94\% \pm 2\%$	$94\% \pm 1\%$

Table 3.2: Central electron track finding efficiencies from the unbiased leg of central-central $Z \to ee$ events.

opposite charge. This effect was taken out on average, but there remained a false curvature as a function of both η and ϕ which could, in principle, affect the charge asymmetry measurement through the P_T and E/P cuts. In the case of the electrons this is a very small effect because the cuts are quite loose, but the muon measurement, with its tighter P_T cut, could be slightly affected; therefore the false curvature was removed by correcting P_T and E/P before the cuts were applied (see Appendix A).

The second, unbiased leg, in the Z events was also used to determine the charge

	ϵ^+	ϵ^-	ϵ^{tot}
E_{Had}/E_{EM}	$99.0\% \pm 0.2\%$	$99.4\% \pm 0.2\%$	$99.2\% \pm 0.2\%$
$LShr$	$98.1\% \pm 0.3\%$	$98.1\% \pm 0.3\%$	$98.1\% \pm 0.2\%$
$Isolation$	$98.9\% \pm 0.3\%$	$99.0\% \pm 0.3\%$	$98.9\% \pm 0.2\%$
χ^2_s	$95.3\% \pm 0.5\%$	$94.6\% \pm 0.5\%$	$94.9\% \pm 0.3\%$
δX	$96.5\% \pm 0.4\%$	$96.6\% \pm 0.4\%$	$96.6\% \pm 0.3\%$
δZ	$97.8\% \pm 0.4\%$	$98.5\% \pm 0.4\%$	$98.1\% \pm 0.2\%$
total	$89.2\% \pm 0.7\%$	$89.1\% \pm 0.7\%$	$89.2\% \pm 0.5\%$
Conversion Cut[2]	$97.3\% \pm 0.4\%$	$98.0\% \pm 0.4\%$	$97.6\% \pm 0.3\%$

Table 3.3: Central electron efficiencies from tight central $W \to e\nu$ events.

independence of finding a central track which passes the selection requirements ($CurSig$, D_0, E/P and P_T cuts). Because the Z decay leptons have slightly more P_T than the W decay leptons, the P_T cut was increased by a factor of M_Z/M_W to 17 GeV. Table 3.2 lists the total as well as the charge and $\eta\pm$ separated efficiencies and Figure 3.3 shows the efficiencies as a function of η (the binning is identical to that which will be used for the asymmetry measurement). No significant charge or η dependent differences in the efficiencies for finding a track are found.

3.3 Central Electron Efficiencies

To verify the charge independence of the electron i.d. efficiencies, a clean sample of W events was selected from the central $W \to e\nu$ data set by requiring $\not{E}_T > 30$ GeV, $E_T > 30$ GeV, $M_T^W < 100$ GeV and the highest E_T jet was < 5 GeV (as well as the fiducial electron and event cuts). A very loose E_{Had}/E_{EM} cut was also applied (but it is known to be greater than 99% efficient for electrons from testbeam measurements).

[2]Only the relative efficiencies are meaningful as there are real as well as fake conversions being removed by this cut.

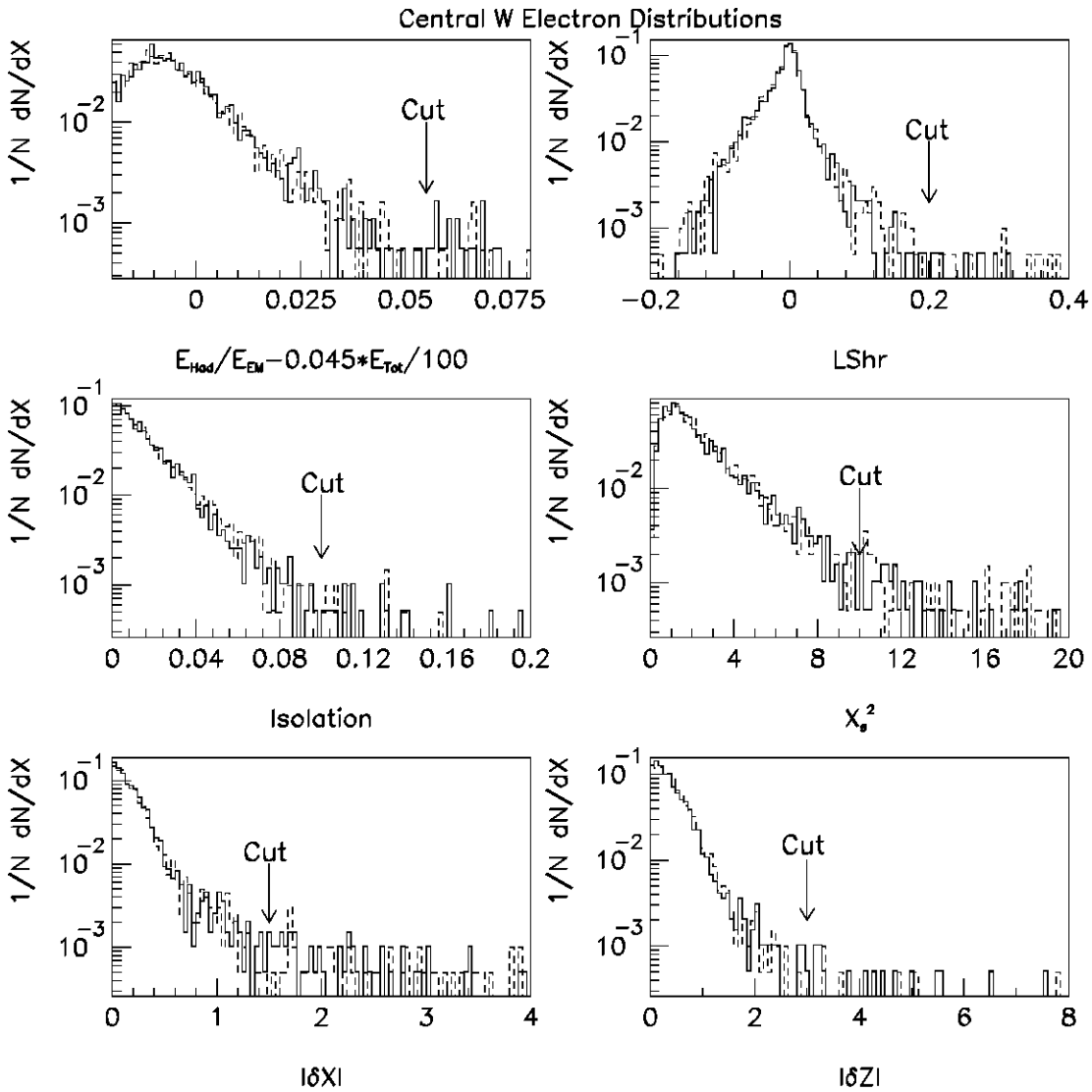

Figure 3.4: Distributions of the central e i.d. variables for good W decay electrons. The solid histograms are for e^+ and the dashed for e^-, as expected the distributions are the same for the two charges. The arrows indicate the value at which the cuts were applied.

There is a small non-electron background in this sample (estimated to be $< 0.5\%$). However, this poses no problem because the backgrounds are expected to be charge symmetric, and only the relative efficiencies for e^+ and e^- are relevant to this analysis. Table 3.3 lists all the efficiencies for the cuts used, and no charge dependent effects are evident. Figure 3.4 shows distributions of the electron i.d. variables for this sample of clean e^+ and e^- from W decays.

3.4 Central W Electron Backgrounds

3.4.1 QCD

General QCD processes can fake a W decay when one jet is mismeasured, due to either a calorimeter measurement fluctuation or a calorimeter crack (producing the required $\not\!\!E_T$) in conjunction with a jet being misidentified as an electron. This misidentification can occur by: the overlapping of a π° and a charged particle, a semileptonic decay of a heavy quark ($b \to ce\nu$ *or* $c \to se\nu$) or a "charge exchange" process via the reaction $\pi^- + p \to \pi^\circ + n$ (or $\pi^+ + n \to \pi^\circ + p$). Because there is invariably jet activity in such events, the cut on the maximum jet E_T greatly reduces these backgrounds.

To estimate the amount of QCD background remaining in the W data, two "control" samples, which contain little contamination from real W events, were used. These samples were made by initially selecting events which had an electron candidate, which passed all the i.d. cuts except the isolation requirement, and contained $\not\!\!E_T < 10$ GeV. Z candidates were explicitly removed and the two control samples (the second sample is a subset of the first) were selected by requiring a jet which satisfied:

QCD Sample 1: $E_T^{jet} > 10$ GeV and $E_{EM}/E_{Tot} < 0.8$

QCD Sample 2: $E_T^{jet} > 20$ GeV and $E_{EM}/E_{Tot} < 0.8$,

where E_{EM}/E_{Tot} is the ratio of electromagnetic to total energy associated with the jet; this cut insures that the jet is hadronic. Then three separate regions in the *Isolation* versus $\not{E}_T$ plane were defined:

1) *Isolation* < 0.1 and $\not{E}_T < 10$ GeV

2) *Isolation* > 0.3 and $\not{E}_T < 10$ GeV

3) *Isolation* > 0.3 and $\not{E}_T > 25$ GeV.

The cut, *Isolation* > 0.3, defines a region which is supposed to be signal free. In principle a W decay electron could radiate at a large angle and thus appear non-isolated, resulting in an overestimate of the QCD background. This effect was investigated (see Appendix B) and it was found that the background estimation was stable with regard to this non-isolation criteria. The background in the signal region was then determined by:

$$\frac{QCD\ contamination}{\#Events\ in\ region\ 3} = \frac{\#events\ in\ region\ 1}{\#events\ in\ region\ 2}(From\ control\ samples)$$

under the assumption that $\not{E}_T$ and *Isolation* are independent variables. Figure 3.5 shows the *Isolation* distributions for the control samples and the signal sample. One sees that the average isolation for low $\not{E}_T$ is essentially flat, supporting the assumption used in this background estimation.

The two control samples yielded backgrounds of $(0.41 \pm 0.08)\%$ and $(0.36 \pm 0.07)\%$. Taking the average of these numbers and interpreting the spread as a systematic uncertainty, the QCD related background was found to be $(0.4 \pm 0.1)\%$ of the central electron

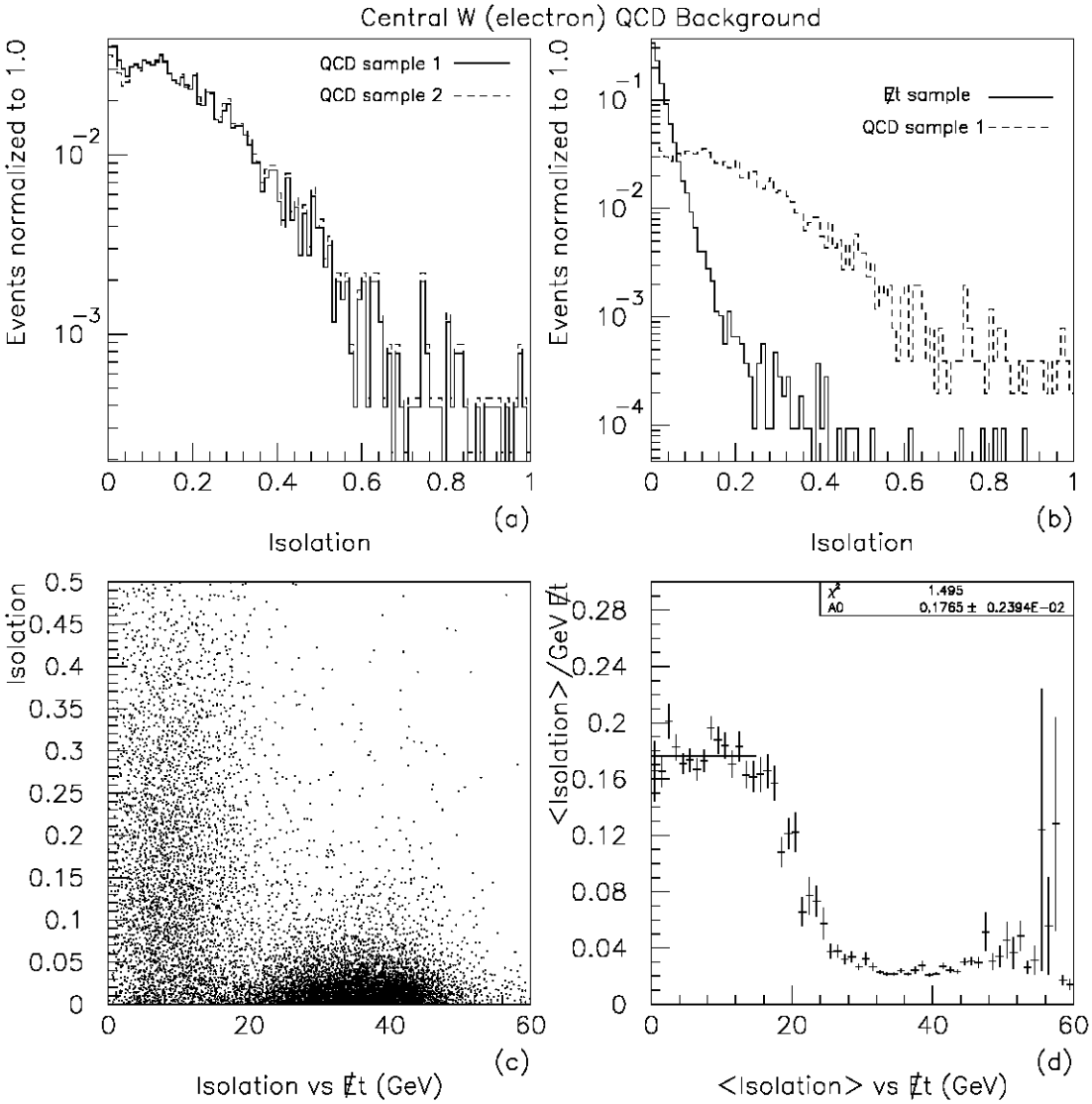

Figure 3.5: a) Isolation in a cone of R=0.4 (*Isolation*) for the two central W QCD background samples, b) for the signal sample (minus the isolation cut) and the control sample 1. c) A scatter plot of *Isolation* vs $\not\!\!E_T$ in the inclusive central electron sample and d) the average *Isolation* as a function of $\not\!\!E_T$.

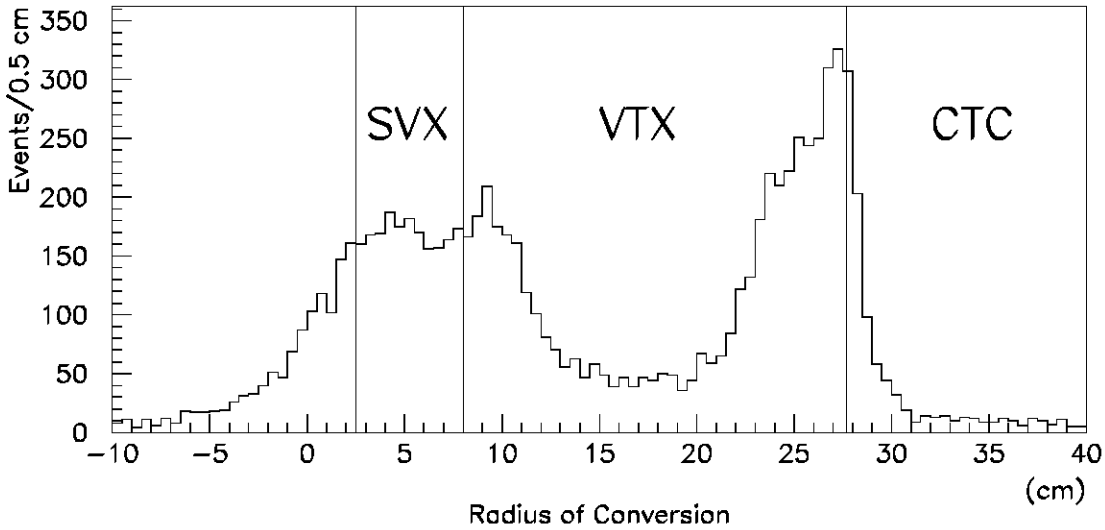

Figure 3.6: The primary sources of conversion electrons are the walls between various tracking chambers and the bulk silicon of the SVX.

data sample.

Conversions

QCD processes can also produce electrons through photon conversions ($\gamma \rightarrow e^+e^-$) which take place in the material inside the CTC, primarily, the beampipe, SVX, VTX and the inner wall of the CTC (see Figure 3.6). These conversion electrons were explicitly removed by searching for a second track which, when combined with the primary electron track, was consistent with coming from the conversion of a photon into an e^+e^- pair. This condition is determined by pairing the electron track with all other tracks of opposite charge. Two conditions were then checked for each pair of tracks: the difference $|\Delta cot(\theta)| < 0.06$ radians, and $S < 0.2$ cm, where S is the distance, in the x-y plane, between the tracks at the point where the two helixes are tangent.

3.4.2 Vector Boson

The backgrounds in the W data due to $W \rightarrow \tau\nu$, $Z \rightarrow l^+l^-$ ($l = \mu$ *or* e) where one lepton is lost, and $Z \rightarrow \tau\tau$ followed by a τ decay to a μ *or* e were estimated using a Monte Carlo generator and detector simulation. The uncertainties associated with these backgrounds are due primarily to uncertainties in the parton distribution functions (PDF's), and in the case of the lost Z decay lepton, the tracking efficiency in the plug region. Three sets of distributions were used, MRS E′, HMRS B and GRV HO, and the plug tracking efficiency was varied by $\pm 10\%$ (the statistical error on the measured efficiency is $< 3\%$). The choices of PDF's were made to cover the extremes in asymmetry predictions (see Figure 1.4). The variation due to PDF choice was found to be less than 10% in all the channels.

$W \rightarrow \tau\nu$

The background due to $W \rightarrow \tau\nu \rightarrow e\nu\nu\nu$ decays was estimated using a Monte Carlo which correctly handled the polarization of the τ and W (it also included a detector model) [27]. Equivalent luminosities of $W \rightarrow \tau\nu$ and $W \rightarrow e\nu$ events were generated. Then the fraction (%) of τ events, relative to $W \rightarrow e\nu$ events, which pass the selection criteria was determined to be $bg^\tau = (2.0 \pm 0.2)\%$, where the error is the spread due to PDF choice (the statistical error on the samples was negligible).

$Z \rightarrow e^+e^-$

Z's were explicitly removed from the data samples by rejecting events which, when combined with another EM cluster, formed an invariant mass between 60 and 120 GeV.

The cut on the P_T of the second track removed most of the remaining Z events (it is almost 100% efficient out to $|\eta| < 1.7$). Events where the invariant mass is poorly reconstructed are further removed by the E_T^{jet} cut (an EM cluster also forms a jet cluster) and the $\not{E}_T$ cut. Z's survive these cuts only when one of the electrons strikes a crack in the calorimeter outside the tracking volume. A Monte Carlo generator, HERWIG [28], plus the CDF detector simulation was used to generate $Z \to e^+e^-$ events. The tracking efficiency in the plug region was not correctly modeled, so the efficiency was determined using the plug W sample (see Appendix C). For electrons, varying the tracking efficiency by $\pm 10\%$ had no noticeable effect because the calorimeter found most of the electrons in the affected η regions. Equal numbers of W's and Z's were generated. The Z's were then normalized to the W's using the ratio $R \equiv \sigma(W \to e\nu)/\sigma(Z \to ee) = 10.6$ (as measured by CDF [29]), and the fraction (%) of Z events passing all cuts relative to W events was determined. It was found that, in the electron case, this background is negligible. Only $bg^Z = (0.18 \pm 0.01)\%$ of the central electron W sample is estimated to come from this process.

$Z \to \tau^+\tau^-$

These events can fake a W when one of the τ's decays to an electron or its hadronic decay fakes an electron. Again the HERWIG Monte Carlo generator and detector simulation were used and the total number of $Z \to \tau^+\tau^-$ events passing the selection cuts normalized, by R, to the generated W sample. The background is estimated to be $bg^{Z\to\tau\tau} = (0.07 \pm 0.01)\%$ of the central W sample, which is negligibly small.

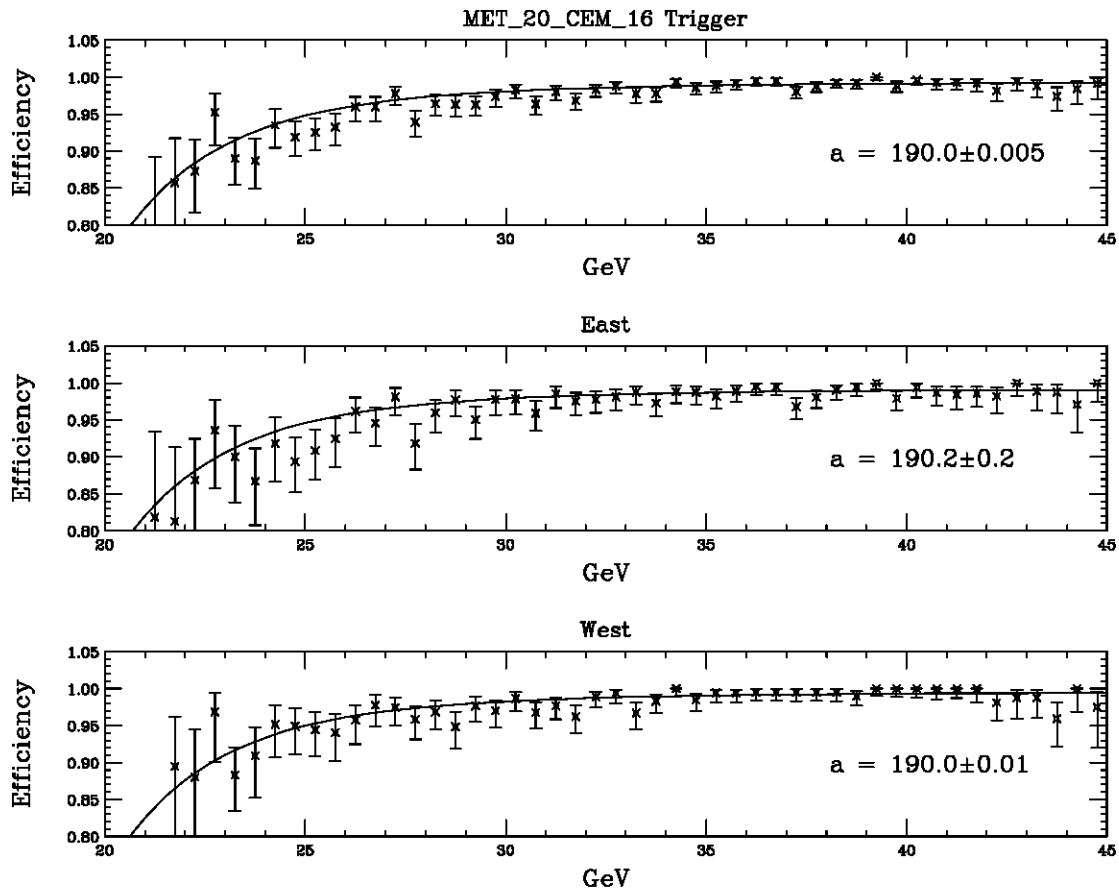

Figure 3.7: The efficiency of the "MET_20_CEM_16" trigger as function of E_T for events with $\not{E}_T > 25$ GeV. The curves are fits to $(1+41000)/(exp(a/E_T)-41000)$. The fitted coefficient "a" is the same in both arches, indicating no systematic differences between arches for high E_T electrons exists.

3.5 Central High P_T Electron Triggers

The high P_T lepton triggers can affect the asymmetry measurement by modifying the acceptance as a function of E_T (or P_T). Since the asymmetry is a ratio of cross sections any overall inefficiencies in the triggers cancel; only the shape and the relative efficiencies for positive and negative electrons are important.

The central $W \rightarrow e\nu$ events are primarily accepted by the "MET_20_CEM_16"

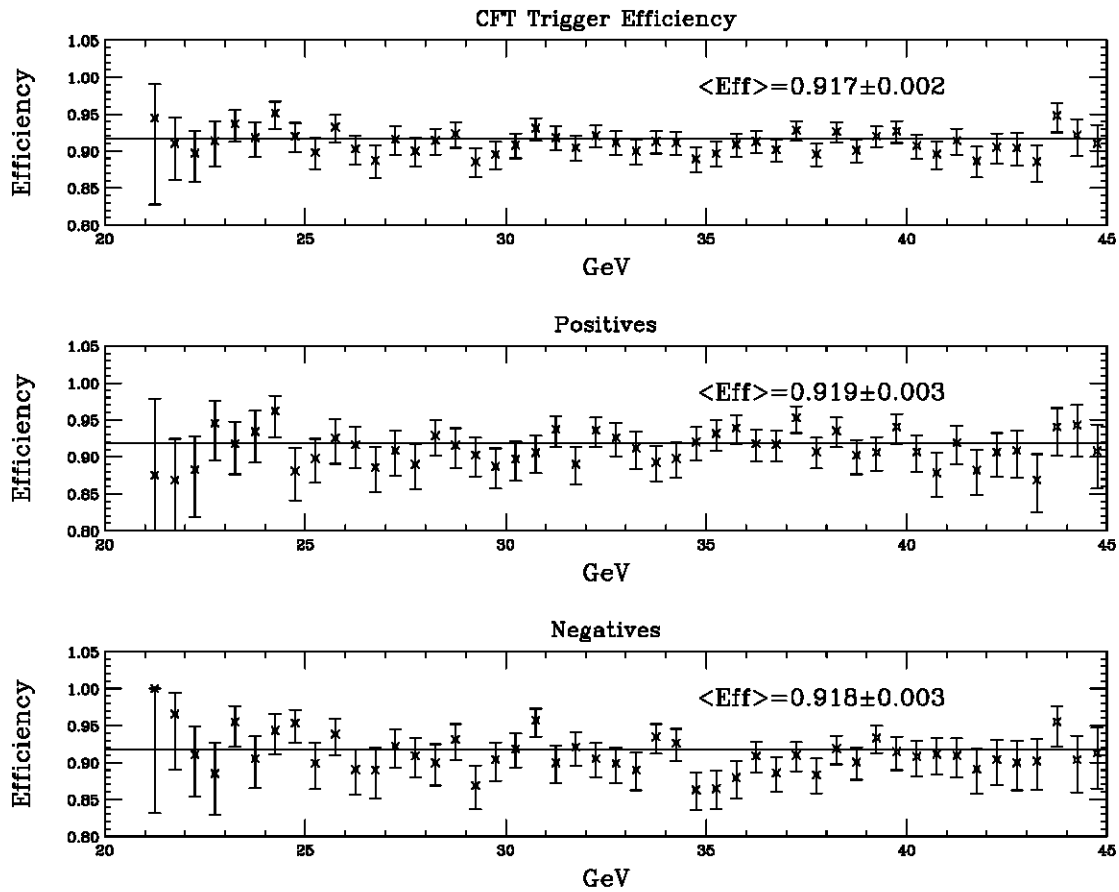

Figure 3.8: The efficiency of the CFT based trigger as a function of E_T and charge of the tracked lepton. The curves show that this trigger is flat in E_T and is charge independent for electrons with $E_T > 25$ GeV.

trigger when $\not\!\!E_T > 25$ GeV and $E_T > 25$ GeV are required. Since this trigger is based solely on calorimeter information, no charge dependence is expected, but the East and West arches of the central calorimeter may have different trigger saturation properties. Figure 3.7 shows the E_T dependence of the two halves separately for data which pass the $\not\!\!E_T$ cut. No difference between the two halves is seen and this trigger alone is found to be greater than 90% efficient at 25 GeV.

There is a second trigger which relies on the CFT as well as lower E_T requirements

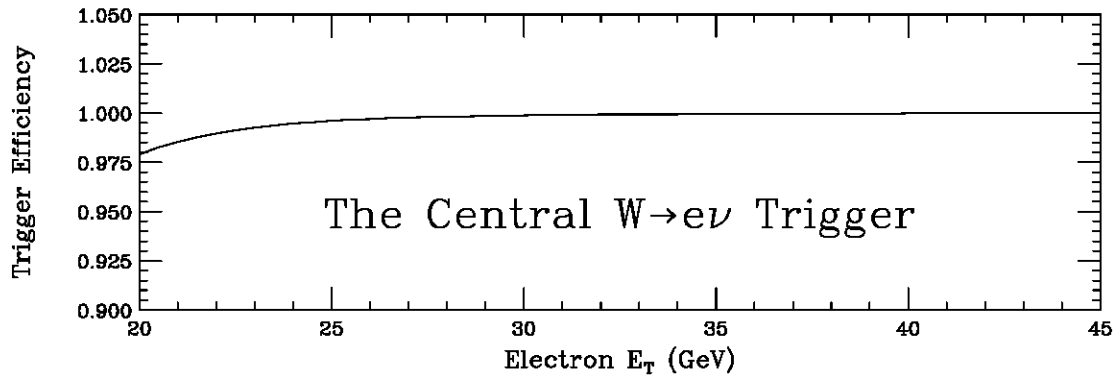

Figure 3.9: The efficiency, as a function of electron E_T, of the logical OR of the $\not\!\!E_T$ and CFT based triggers is essentially flat for $E_T > 25$ GeV. Therefore no trigger related corrections are necessary for the central electron sample.

which fills in the low edge of the "MET_20_CEM_16". This trigger requires a CFT track with $P_T > 9.2$ GeV matched to a central EM cluster of $E_T > 9$ GeV at trigger level two. Figure 3.8 shows the CFT trigger's efficiency as a function of E_T and charge. One sees that this trigger's efficiency is flat in E_T, at 92%, and independent of the lepton's charge.

The asymmetry analysis makes use of the logical OR of these two triggers, which is essentially flat in E_T and greater than 99% efficient, as shown in Figure 3.9. Therefore no correction for the central electron trigger efficiency is needed in the asymmetry analysis.

Chapter 4

Plug $W \rightarrow e + \nu$

The asymmetry analysis uses as much of the CDF calorimetry as the CTC coverage allows; this includes a portion of the plug electromagnetic calorimeter. Many improvements were made to the PEM and its trigger since the previous asymmetry analysis at CDF [30]. The PEM had repairs done which mitigated surface currents, and had special level two trigger hardware, the "spike-killer", installed to reduced neutron induced EM triggers. In the previous run ($\sim 4\ pb^{-1}$ of data), these two sources of noise resulted in spurious triggers at a high rate; as a result, the outer η rings of the PEM had to be removed from the trigger. Additionally, active stabilization of the gas gain (high-voltage feedback) and improving the tower-to-tower energy calibrations improved the level two trigger's energy resolution for the current data set. These modifications resulted in a greatly improved PEM electron trigger, yielding a factor of two more usable W events per pb^{-1} than in the prior Tevatron run.

4.1 Plug Electrons

Like the central electron data set, the plug electron $W \rightarrow e + \nu$ events were initially stripped from the primary data stream for immediate processing. Since the asymmetry analysis was the only one to use the plug W data set, the data were removed from the central computer and stored on five 8 mm tapes (in a compressed data format the entire data set fit easily on a single workstation's disk). Because this data was selected by requiring very loose electron i.d. cuts, the initial data set of greater than 40,000 events yielded fewer than 3000 plug W candidates. However, the loose cuts prevented any serious difficulties in recovering from problems uncovered early in the run.

Energy Corrections

Three corrections were made to the raw energy measured by the PEM. A tower-to-tower response map for each of the plug detectors was determined using 100 GeV electrons at a testbeam [31]. The absolute energy scale and a nonlinearity correction were also determined at the testbeam using an "energy scan" performed with 25-175 GeV electrons. During the course of the run several anode layers lost high voltage for various reasons. The effect of these failures was taken out, on average, by correcting the measured energy based on the average longitudinal shower shape, which had been measured at the testbeam. This "dead layer" correction was also incorporated into the level two trigger. Early in the run it became evident that the overall energy scale was incorrect (about 7% low) by looking at the invariant mass of Z's, where one electron was found in the CEM and the other in the PEM (central-plug Z's). Therefore the energy scale

was modified to yield the correct Z mass. The invariant mass of the central-plug Z's is shown in Figure 4.1. The fit, which uses the entire run's Z sample and takes radiative corrections into account, indicates that the overall PEM energy scale is accurate at the same level as the CEM's (1%).

There was concern about the online correction (see page 25) which was performed throughout the run to stabilize the PEM's response for variations in temperature and pressure. The same Z data was also used to address this question and to verify that the quadrant-to-quadrant variations (observed to be as large as 10% in the 1988-89 run) were removed by the deadlayer and map corrections (see Appendix D). All the online corrections were found to be correct, and no post-processing of the data was necessary.

W Selection Criteria

The E_T, $\not{E}_T$, E_T^{jet}, $Isolation$, P_T^{high}, $CurSig$, D_0 and Z_0 variables and cut values are the same as used in the central region and are described in detail on pages 30-35. The following variables are specific to electrons found in the plug EM calorimeter.

$\boldsymbol{E_{Had}/E_{EM} < 0.05}$**:** Unlike the central calorimeter, no linear correction is made to the ratio of hadronic to EM energy. This cut helps to remove non-electron backgrounds.

$\boldsymbol{\chi^2_{PEM} < 3.0}$**:** The χ^2 of 3x3 profile of the EM shower is defined as,

$$\chi^2_{PEM} = 1/9 \left(\sum_i^{3\times3} \left(\frac{E_i^{meas} - E_i^{pred}}{\Delta E_i^{meas}} \right) \right),$$

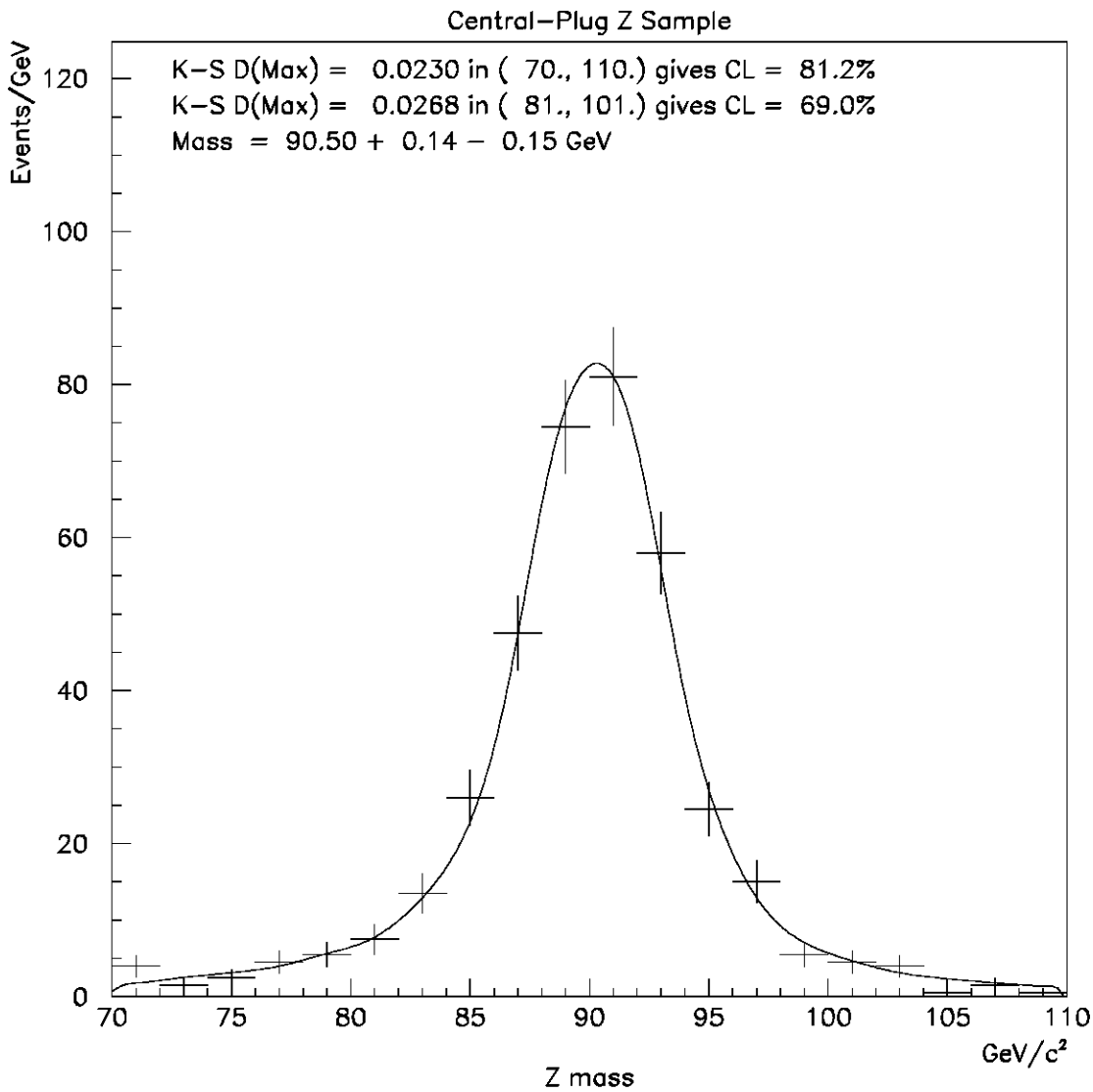

Figure 4.1: A fit for the Z mass taking radiative corrections into account, for central-plug $Z \rightarrow ee$. Also shown are the Kolmogorov-Smirnov test results for the unbinned data in the ranges $70 < Z\ mass < 110$ and $81 < Z\ mass < 101$.

where E_i^{pred} is the expected energy in a tower based on the transverse shower profiles measured at the testbeam.

1 GeV $< P_T <$ 200 GeV: The momentum resolution of a track in the plug region is quite poor and depends on Z_0 and η_{det} of the electron. Therefore P_T is not a good variable to cut as tightly on in the plug as in the central region.

$|\delta\phi| <$ 0.04 rad: The distance (in radians) between the extrapolated CTC track and the position of the EM energy cluster centroid, as determined by the plug strip chamber (PES), was required to be consistent with a high P_T electron.

$|\delta R| <$ 10.0 cm: The distance (in cm) between the extrapolated CTC track and the radial position of the EM energy cluster centroid, as determined by the strip chamber, had a loose cut applied because the stereo reconstruction by the CTC can be very poor in the plug region.

$VTX_{occ} >$ 0.5: The VTX occupancy is the ratio of expected to found hits on the wires of the vertex detector along the "road" between the calorimeter cluster and the event vertex.

In addition, the electron candidate was required to be in the fiducial region of the calorimeter, which is defined as $1.2 < |\eta_{det}|$ and the cluster centroid, as determined by the PES, is greater than 5 cm from the nearest 90° crack (the PEM quadrant boundaries). The EM cluster was also required to be in a region where charge determination by the CTC is possible, $|\eta_{det}| < 1.7$. Approximately 19.5 pb^{-1} remained in the data set after the removal of bad runs (i.e. runs where there were detector or DAQ failures).

The previous cuts were applied to a data set, consisting of 43584 events, which had been filtered from the primary data stream by satisfying the following initial loose cuts on the raw (uncorrected) variables:

$E_T > 20\ GeV$

$\chi^2_{PEM} < 3.0$

$E_{Had}/E_{EM} < 0.05$

$\not{E}_T > 20\ GeV.$

The events in the sample had their CTC tracks refitted after the Tevatron run was completed, using the same CTC wire alignment positions which were used for the refitting of the tracks in the central W and Z samples. Figure 4.2 shows the transverse mass spectrum of the 2705 events which pass all the selection cuts.

4.2 Tracking into the Plug Region

The PEM and the CTC only partially overlap. Electrons further out in η will traverse fewer layers of the CTC before exiting the tracking volume. The charge identification roughly requires that the lepton have $|\eta_{det}| < 1.7$. To determine the probability that the charge of the electron is misidentified, a sample of Z's, satisfying the cuts listed in Table 3.1 (plus the plug electron had a $\chi^2_{PEM} < 3.0$), was selected where the second leg passed the plug W track requirements. None of the 332 Z candidates had same sign leptons, implying an upper limit of

$$p^{\pm} < 0.90\% \ (90\%\ C.L.)$$

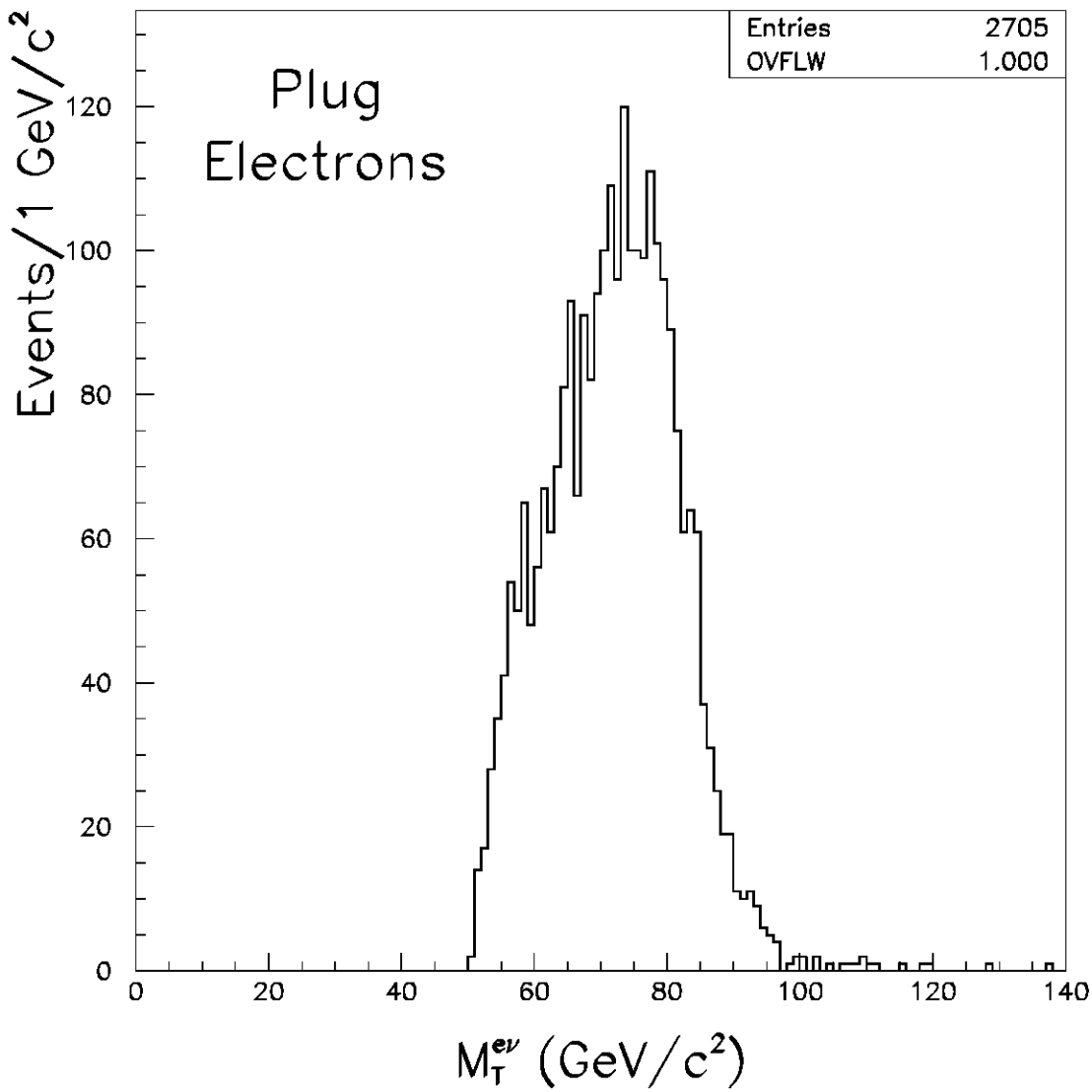

Figure 4.2: The transverse mass spectrum of the plug electron W candidates to be used in the asymmetry analysis.

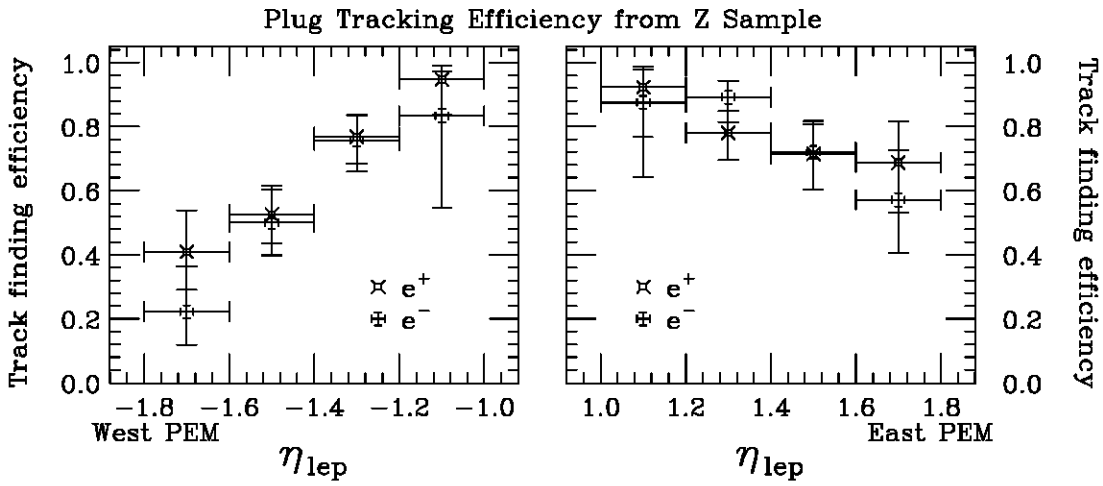

Figure 4.3: The charge independence of tracking into the plug region is tested using the central-plug Z sample. The charge of the plug track is determined by the central track.

	ϵ^+	ϵ^-	ϵ^{tot}
West	$65\% \pm 5\%$	$56\% \pm 6\%$	$62\% \pm 4\%$
East	$77\% \pm 5\%$	$79\% \pm 5\%$	$77\% \pm 3\%$
Total	$70\% \pm 3\%$	$67\% \pm 4\%$	$69\% \pm 3\%$

Table 4.1: Track finding efficiencies for plug electrons ($1.0 < |\eta_{lep}| < 1.8$).

on the probability of misidentifing the lepton's charge.

Further, since the track finding efficiency falls rapidly for $1.4 < |\eta_{det}|$, the same set of Z's was used to determine the efficiencies as a function of charge (as determined by the central leg) and η. Because a second track was no longer required in this efficiency study, the following additional cuts were required to keep the level of background low. The invariant mass cut was tightened to be within 15 GeV of the Z (91 GeV) and a tighter E/P cut was applied to the central leg ($0.8 < E/P < 1.5$). The track finding efficiencies are shown in Figure 4.3, and Table 4.1 lists the overall efficiencies for the West and East PEM. The difference in the efficiencies between the East and West PEM

	ϵ^+	ϵ^-	ϵ^{tot}
E_{Had}/E_{EM}[1]	$98\% \pm 1\%$	$97\%^{+1\%}_{-2\%}$	$97.7\%^{+.7\%}_{-1\%}$
χ^2_{PEM}	$95\%^{+1\%}_{-2\%}$	$92\% \pm 2\%$	$93.7\%^{+1\%}_{-1\%}$
$Isolation$[2]	$99.2\%^{+.3\%}_{-.5\%}$	$99.1\%^{+.4\%}_{-.6\%}$	$99.1\% \pm .3\%$
VTX_{occ}	$89.3\% \pm 1.4\%$	$91.6\% \pm 1.2\%$	$90.5\% \pm 0.9\%$
$\delta\phi$	$97.3\%^{+.6\%}_{-.8\%}$	$97.8\%^{+.6\%}_{-.7\%}$	$97.6\%^{+.4\%}_{-.5\%}$
δR	$98.0\%^{+.6\%}_{-.7\%}$	$96.6\%^{+.6\%}_{-.9\%}$	$97.3\% \pm 0.5\%$
total	$84.1\% \pm 1.5\%$	$86.6\% \pm 1.4\%$	$85.4\% \pm 1.0\%$
Conversion Cut[3]	$98.5\%^{+.5\%}_{-.7\%}$	$98.4\%^{+.5\%}_{-.7\%}$	$98.5\%^{+.4\%}_{-.5\%}$

Table 4.2: Plug W decay electron efficiencies found using central-plug Z's and tight plug W's.

is due to the offset in z of the average interaction point ($\sim$ 2 cm). Electrons which are detected in the East PEM traverse a larger fraction of the CTC and exit at a larger radius, on average, than do those detected in the West PEM for a given value of $|\eta_{lep}|$ (the pseudorapidity calculated from the event vertex). This results in the higher efficiencies seen in the East PEM. Again, as long as the efficiencies are the same for e^+ and e^- the charge asymmetry remains unaffected. No significant differences in the tracking efficiencies for e^+ and e^- are found.

4.3 Plug Electron Efficiencies

As in the case of the central detector, a sample of W candidates which passed tight kinematic cuts (see page 40) was selected from the plug W data sample. This sample already had the E_{Had}/E_{EM} and χ^2_{PEM} cuts applied to the data; therefore the

[1]The E_{Had}/E_{EM} and χ^2_{PEM} efficiencies were found using the plug leg of central-plug Z's from in the inclusive central electron sample.

[2]The $Isolation$, VTX_{occ}, $|\delta\phi|$ and $|\delta R|$ efficiencies were found using a tight plug W electron data sample which had the E_{Had}/E_{EM} and χ^2_{PEM} cuts already applied.

[3]Only the relative efficiencies are meaningful as there are real as well as fake conversions being removed by this cut.

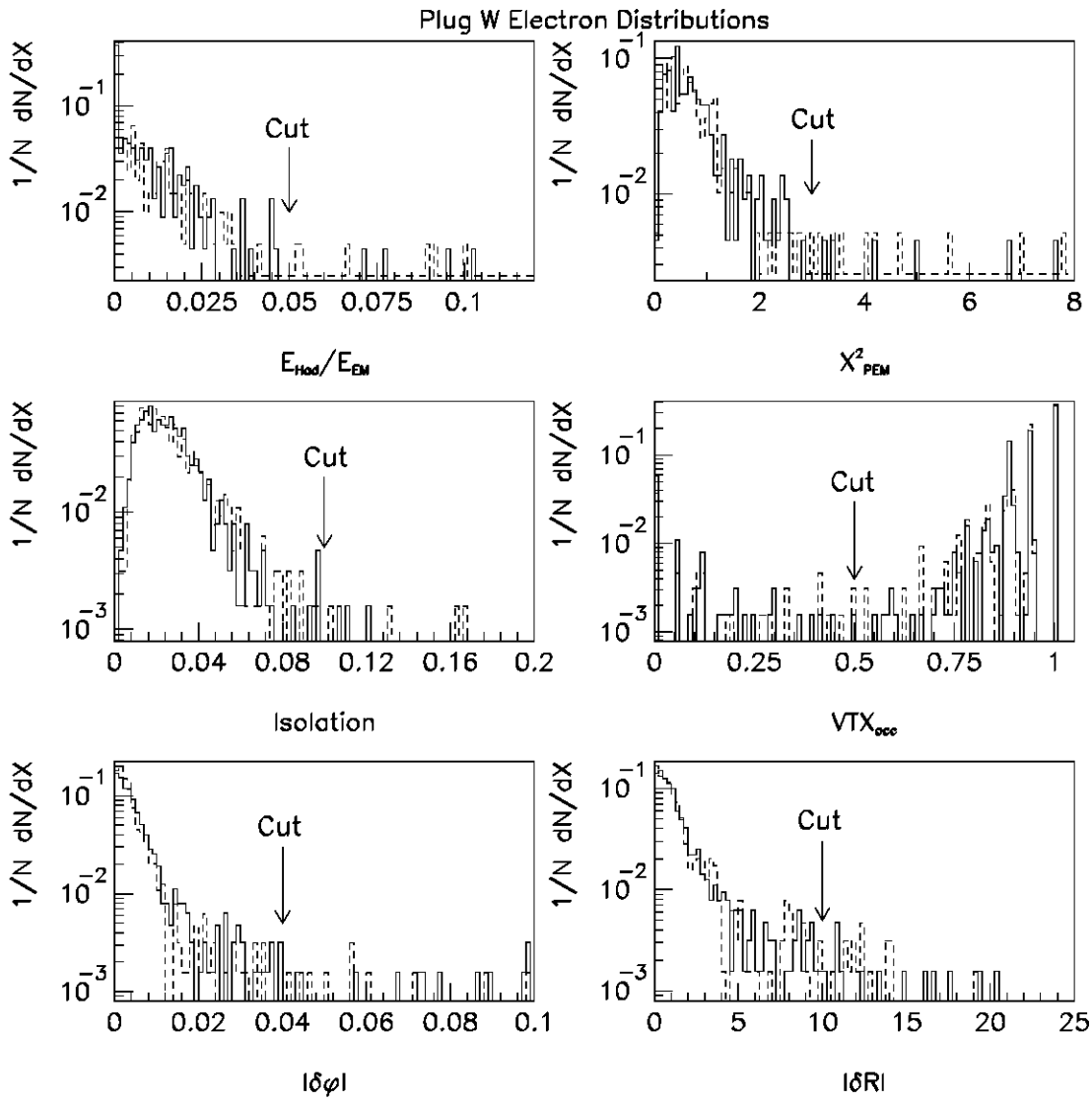

Figure 4.4: Distributions of the plug electron i.d. variables for W decay electrons. The solid histograms are for e^+ and the dashed for e^-, as expected the distributions are the same for the two charges. The arrows indicate the value at which the cuts were applied.

efficiencies for these cuts were determined using the central-plug Z's. Figure 4.4 shows the distributions of the plug variables for e^+ and e^- separately, and Table 4.2 lists the efficiencies of the cuts; no significant differences are found.

4.4 Plug W Electron Backgrounds

4.4.1 QCD

Essentially the same method of determining the QCD background was used in the plug region as was used in the central region (see page 42). The one small difference was the cut used to define the non-isolated region; $Isolation > 0.15$ was used rather than $Isolation > 0.3$ (see Appendix B). Figure 4.5 shows the $Isolation$ distributions for the plug W sample and the QCD control samples. Again, the $Isolation$ and $\not\!\!E_T$ variables are seen to be independent. After extrapolating from the non-isolated region into the signal region, a background of $(4.2 \pm 0.9)\%$ and $(3.9 \pm 0.8)\%$ (of the plug W sample) is found using control samples 1 and 2 respectively. Taking the average and adding in a systematic uncertainty, based on the spread of the two numbers, the QCD background is determined to be $(4.1 \pm 0.9)\%$.

Part of the reason the fractional QCD background is larger in the plug region than in the central region is that the W cross-section is rapidly falling for $|\eta| > 1.0$ and the background is relatively flat. Another cause of this difference is the inefficiency of the conversion filter for tracks at large $|\eta|$.

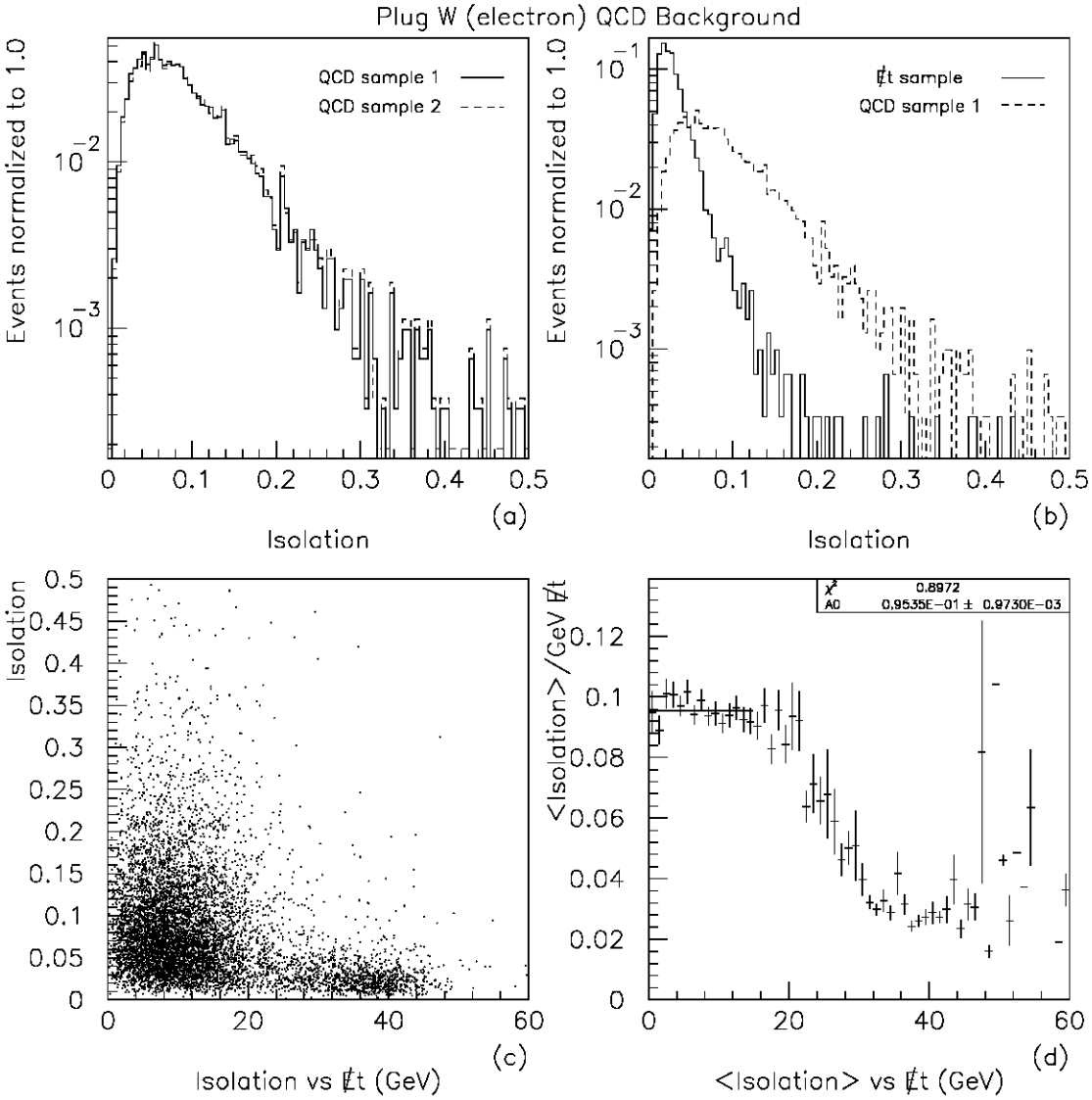

Figure 4.5: a) Isolation in a cone of R=0.4 for the two plug QCD background samples, b) for the signal sample (minus the isolation cut) and the control sample 1. c) A scatter plot of $Isolation$ vs $\not\!\!E_T$ in the inclusive plug electron sample and d) the average $Isolation$ as a function of $\not\!\!E_T$.

Conversions

In addition to the method described on page 45, the requirement that the VTX have 50% of expected hits, on the "road" between the interaction point and the calorimeter cluster, was also used to reject photon conversions. This additional method was employed because the poor tracking efficiency into the plug region limits the usefulness of the first method (where tracks are paired together). However, as Figure 3.6 shows, a fair fraction of the conversions take place in the SVX and the inner wall of the VTX. The occupancy method fails to identify these events, resulting in the larger QCD backgrounds seen in the plug data.

4.4.2 Vector Boson

The methods used to estimate the $W \to \tau\nu$, $Z \to e^+e^-$ and $Z \to \tau\tau$ backgrounds are identical to that used in the central region (see page 46). The results are very similar to those found for the central electron sample:

$\boldsymbol{W \to \tau\nu}$**:** $bg^{\tau} = (2.0 \pm 0.2)\%$,

$\boldsymbol{Z \to e^+e^-}$**:** $bg^{Z} = (0.24 \pm 0.07)\%$,

$\boldsymbol{Z \to \tau^+\tau^-}$**:** $bg^{Z\to\tau} = (0.10 \pm 0.06)\%$.

As in the central electron case, the backgrounds are given relative to the number of $W \to e\nu$ events passing the selection requirements. Again the Z related backgrounds are negligibly small. However, corrections for the QCD and $W \to \tau\nu$ backgrounds will be made to the observed asymmetry.

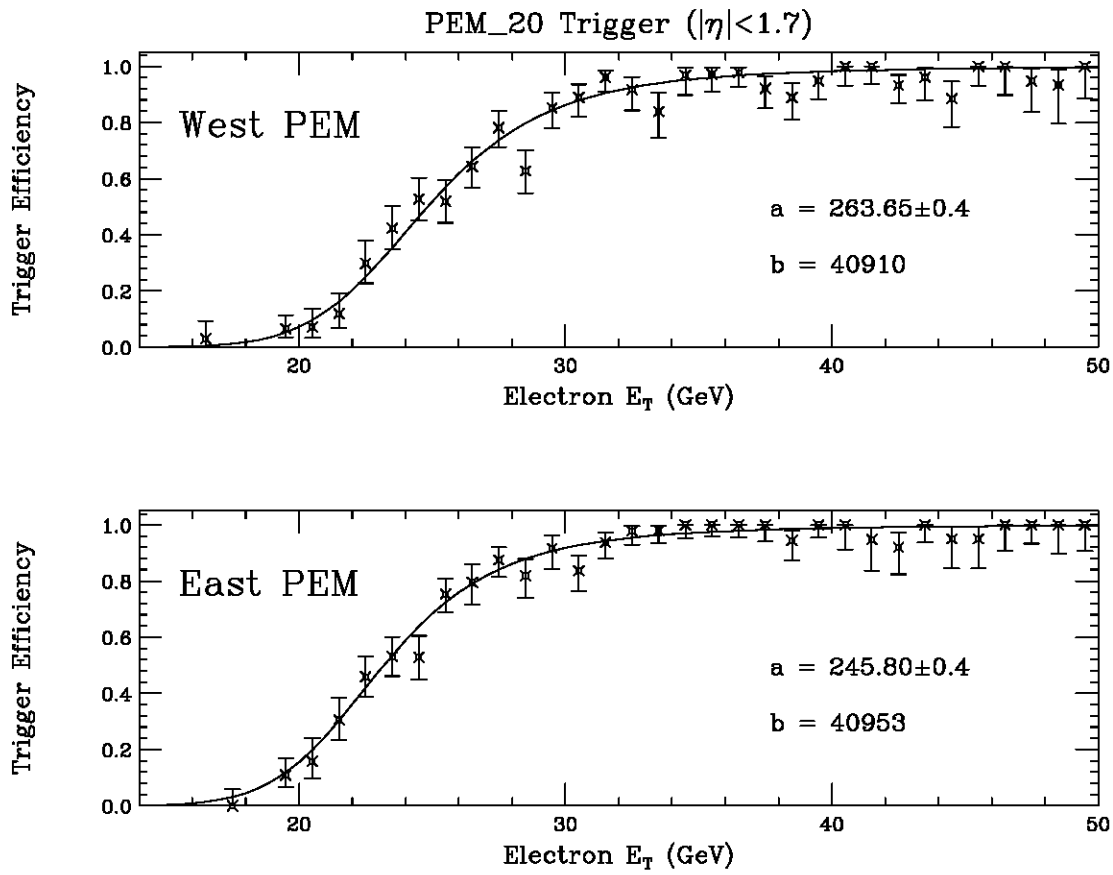

Figure 4.6: The primary electron trigger in the PEM requires a 20 GeV EM cluster of energy with $E_{Had}/E_{EM} < 0.125$. The curve is a fit to $(1+b)/(exp(a/E_T) - b)$.

4.5 Plug Electron Triggers

Two triggers fed the plug W sample, the "PEM_20" and "PEM_15_MET_15". The PEM_20 trigger required an EM cluster with $E_T > 20$ GeV and $E_{Had}/E_{EM} < 0.125$ at level two. Figure 4.6 shows this trigger efficiency as a function of E_T and a fit to the data. These efficiencies were determined using events which contained good plug electrons, but were accepted by a non-plug trigger. The level two trigger's energy scale was incorrectly set before the Tevatron run was begun, resulting in an effective threshold of ~ 25 GeV. Also, the z position of the event vertex, which has a $\sigma \approx 25$ cm, was not

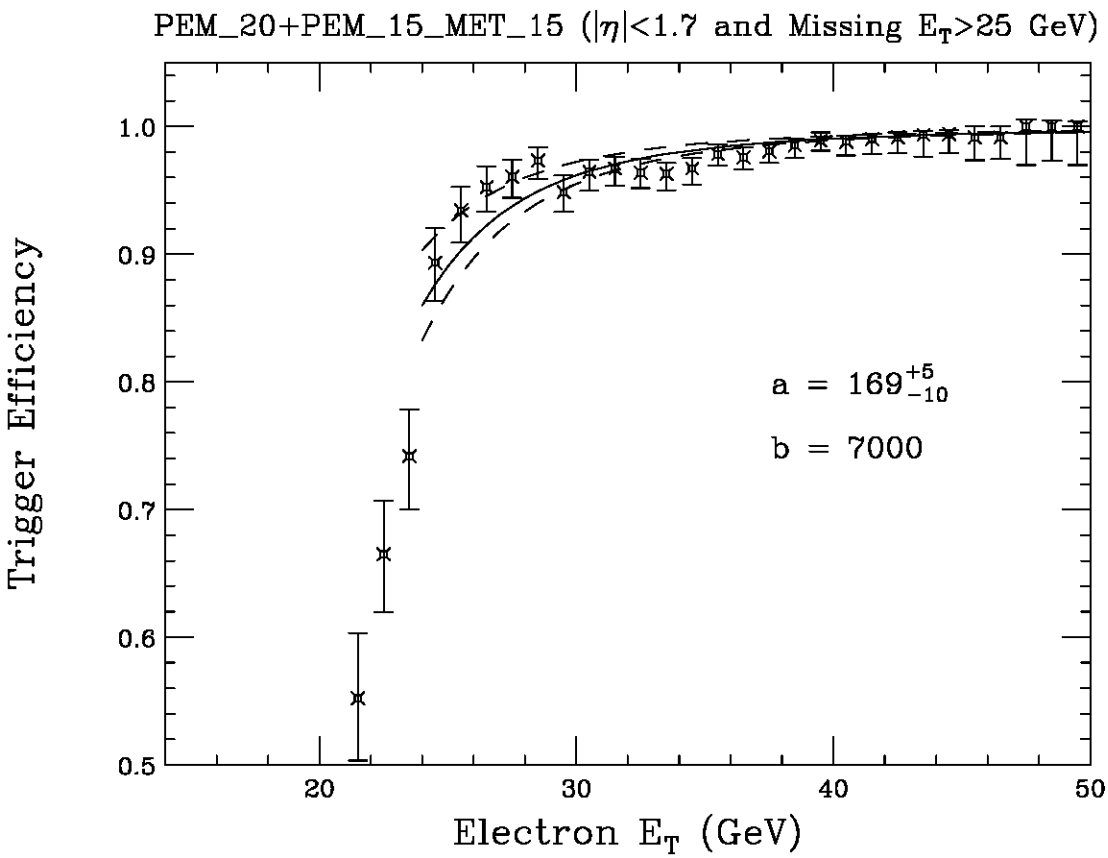

Figure 4.7: The efficiency of the logical OR of the PEM_20 and the PEM_15_MET_15 triggers for events with greater than 25 GeV of $\not\!\!E_T$. The curve is a fit to $(1+b)/(exp(a/E_T)-b)$.

available at level two, resulting in a slow trigger turn-on. The East and West PEM have slightly different efficiency curves due to differing numbers of dead layers and the offset, in z, of the average event vertex.

Fortunately there was a second trigger which accepted W candidates in the plug, the PEM_15_MET_15. This trigger required, in addition to an EM energy cluster of greater than 15 GeV, at least 15 GeV of $\not\!\!E_T$ at level two. Figure 4.7 shows the efficiency for the logical OR of the two plug triggers for events with $\not\!\!E_T > 25$ GeV. No significant difference for $E_T > 25$ GeV was found between the East and West PEM, so the combined data

was fit to $(1+b)/(exp(a/E_T)-b)$, and the resulting curve was used to determine the error induced in the asymmetry measurement. The PEM_15_MET_15 efficiency was found using data accepted by the PEM_20 trigger and the parameterizations shown in Figure 4.6. The error shown in Figure 4.7 is dominated by the uncertainty in the PEM_20 parameterizations [32].

Chapter 5

Central $W \rightarrow \mu + \nu$

The asymmetry analysis benefited from the addition of the central muon extension (CMX), which extended the coverage from $|\eta| < 0.6$ to $|\eta| < 1.0$. Unfortunately, there were unanticipated problems with this new system, the most serious being the high trigger rate. The high rate originated from low momentum charged particles, produced mostly in secondary interactions in a steel flange on the beampipe, scattering off the forward detectors and back into the CMX. During the first half of the Tevatron run, the CMX trigger rate was limited by a prescale factor which was a function of the instantaneous luminosity. Fortunately, a long shut down made it possible for the beampipe to be replaced. The new beampipe greatly reduced the trigger rate, thus allowing the removal of the rate limit. In addition to the CMX, the central muon upgrade (CMP) was installed prior to the run. The CMP chambers cover essentially the same region in $|\eta|$ as the old central muon chambers (CMU) but are located behind more steel, thus allowing the P_T thresholds to be reduced in the trigger. Since the threshold was never a problem for high P_T muons from $W \rightarrow \mu\nu$ events, this change did

not benefit the asymmetry analysis. In fact, because a CMU-CMP match was required in the trigger, the geometric acceptance of the W trigger was slightly reduced.

5.1 Central Muons

As was the case with the electron samples, the central $W \rightarrow \mu\nu$ events were flagged by the level three trigger for immediate processing. In general, the muon samples are cleaner (i.e. they contain fewer non-muon events) than the electron samples. This is because the requirement that the particle traverse at least five absorption lengths of steel rejects the vast majority of the hadronic backgrounds. Muons are identified by matching a "stub" (correlated hits in the four layers of the muon chamber) with a high P_T track in the CTC. In addition, the energy deposited in the calorimeter towers traversed by the muon is required to be consistent with that of a single minimum ionizing particle.

Momentum Measurements

The energy of the muon is determined from its P_T (as measured by the CTC). In this analysis muons were required to have P_T greater than 25 GeV. This high P_T is much greater than the muon mass and therefore $P_T \approx E_T$ is a very good approximation ($P_T = E_T$ is assumed throughout this analysis). The momentum scale is determined from the magnetic field as monitored by the current flowing in the solenoid. It was checked against the mass of J/ψ and Υ resonant events decaying to muon pairs. The fitted mass peaks, shown in Figure 5.1, imply that the momentum scale is known to about 0.07% [33] (when compared to the world averages [34]). The assumption that the P_T measured in the CTC is equal to the E_T of the muon when it was initially produced

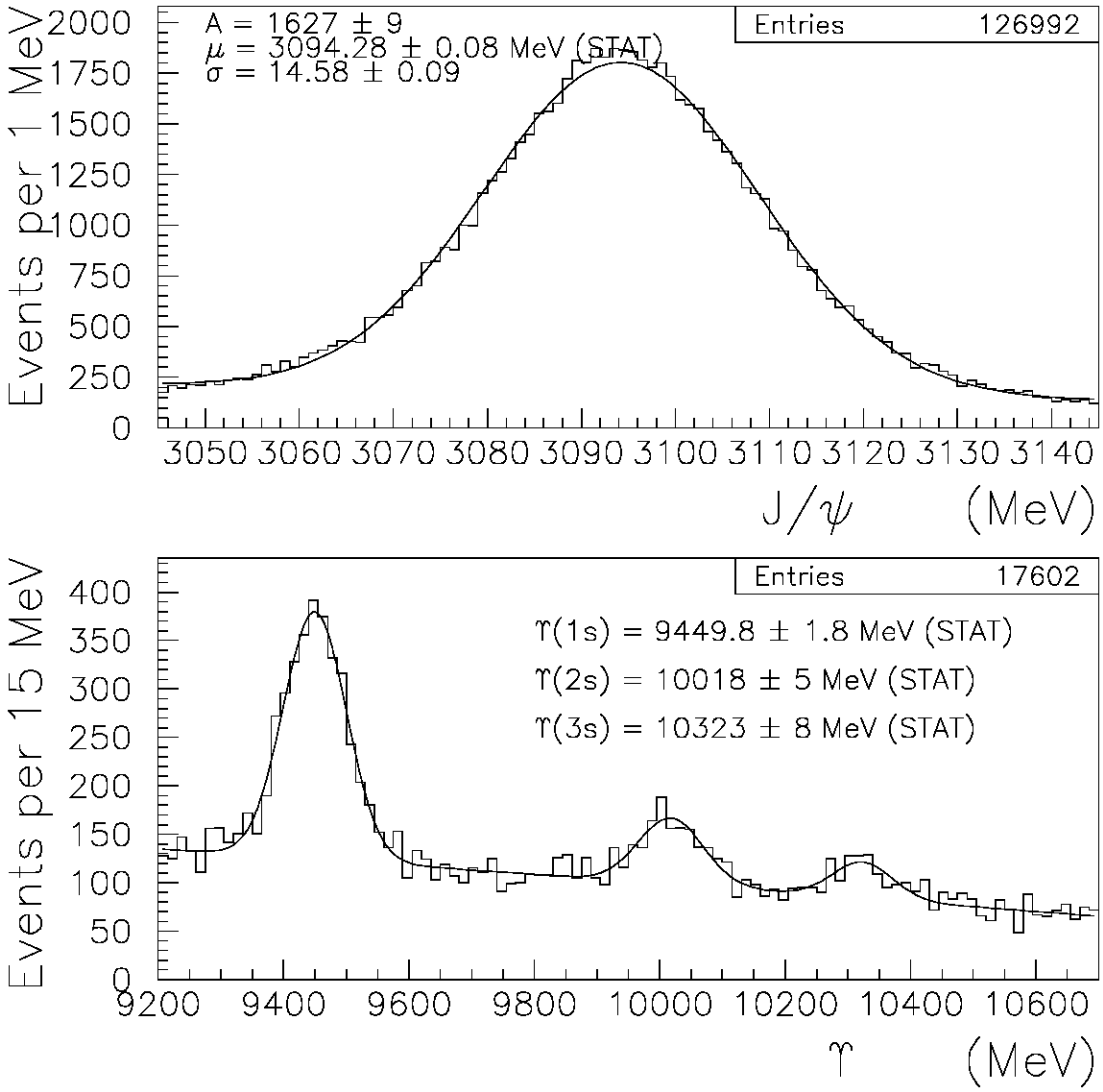

Figure 5.1: The invariant mass spectra of J/ψ and $\Upsilon \rightarrow \mu\mu$ as used to check the momentum scale.

could lead to an error in the case of γ radiation by the muon. This was not corrected for in the muon asymmetry calculation, but was included in the systematic error. In the case of $W \rightarrow e\nu$, this effect is not a problem because the radiated energy is measured in the calorimeter and clustered together with the electron's electromagnetic shower. In the case of muons, the radiated photons are lost, and the measured P_T is systematically low. The size of this systematic was estimated to be about 100 MeV on average. Since this is a small effect no corrections were made. Instead the small systematic error due to a 1% momentum scale uncertainty (the same as in the electron measurement) was used in the muon analysis.

W Selection Criteria

The E_T^{jet}, P_T^{high}, $CurSig$ and Z_0 (event vertex) variables and cut values are the same as used in the electron data selection and are described in detail on pages 30-35. The following variables are specific to muons which are identified by the central muon detectors.

25 GeV $< P_T <$ 150 GeV: The momentum of the beam constrained track was required to be less than 150 GeV. This cut rejects cosmic ray events while still being perfectly efficient for W decay muons.

$\not{E}_T >$ 25 GeV: The $\not{E}_T$ is calculated (see Equation 3.1) after removing the energy contained in the calorimeter tower traversed by the muon and then adding the muon's P_T, as measured by the CTC, to the E_T in the calorimeter.

***Isolation* < 0.1:** Isolation is defined in the equivalent way as was done in the electron case:

$$Isolation = \frac{E_T(0.4) - E_T^{\mu tower}}{P_T^{\mu}} \tag{5.1}$$

where $E_T(0.4) - E_T^{\mu tower}$ is the energy in a cone of radius 0.4 in $\eta - \phi$ space minus the energy in the tower ($R = 0.13$) traversed by the muon. P_T^{μ} is the muon's transverse momentum.

E_{Had} < 6 GeV, E_{EM} < 2 GeV and $E_{EM} + E_{Had}$ > 0.5 GeV: The energy in the calorimeter tower (both EM and hadronic sections) traversed by the muon was required to be consistent with a minimum ionizing particle.

CMU $|\delta X|$ < 2.0 cm, CMP $|\delta X|$ < 5.0 cm and CMX $|\delta X|$ < 4.0 cm: The difference between the position in X ($X = \phi R$) of the reconstructed muon stub and the extrapolated CTC track was required to be less than 2.0, 5.0 and 4.0 cm when the muon is found in the CMU, CMP and CMX respectively.

$|Z_o^{VTX} - Z_o^{track}|$ < 5 cm: The z coordinate of the intercept of the track and the beam-line was required to be within 5 cm of the event vertex as determined by the VTX. This cut helps remove cosmic rays and decays in flight.

In occasional runs there were oscillations in the preamplifier circuits for the muon chambers. Such runs and other "bad" runs were removed from the asymmetry data set, leaving approximately 19.2 pb^{-1} of good data.

These cuts were applied to the initial data set of 64,677 events, which were split from the primary data stream by satisfying the following initial requirements:

$P_T^{\mu} \geq 18$ GeV

$E_{Had} \leq 6$ GeV

$|\delta X| \leq 10$ cm if the muon is in the CMU

$|\delta X| \leq 20$ cm if the muon is in the CMP

$|\delta X| \leq 20$ cm if the muon is in the CMX

No other requirements were necessary because the muon data set is inherently clean. As in the electron case, the tracks were refit when the Tevatron run was completed. In addition the data were used to align the muon chambers with respect to the CTC and the track-stub matching was redone at the same time. Figure 5.2 shows the transverse mass spectrum of the 6114 events which passed all the muon selection cuts.

5.2 Tracking

The track recognition for muons is expected to be virtually identical to that of central electrons. Therefore, the probability of misidentifing the muon's charge is no larger than that found for central electrons, $p^{\pm} < 0.46\%$ (90% $C.L.$). In addition, the $Z \rightarrow ee$ data (see page 39) were used to determine the efficiencies of the muon track selection criteria for positive and negative tracks. The P_T cut was increased by a factor M_Z/M_W to 28 GeV to account for the difference in the P_T spectra of W and Z bosons; otherwise the identical track related cuts ($CurSig$, D_0 and P_T) were applied to the electron from a Z decay as if it were a muon from a W decay. Figure 5.3 shows the efficiencies for track reconstruction as a function of η and charge. If any false curvature (see Appendix A) remained in the data, the efficiencies for the two charges would have

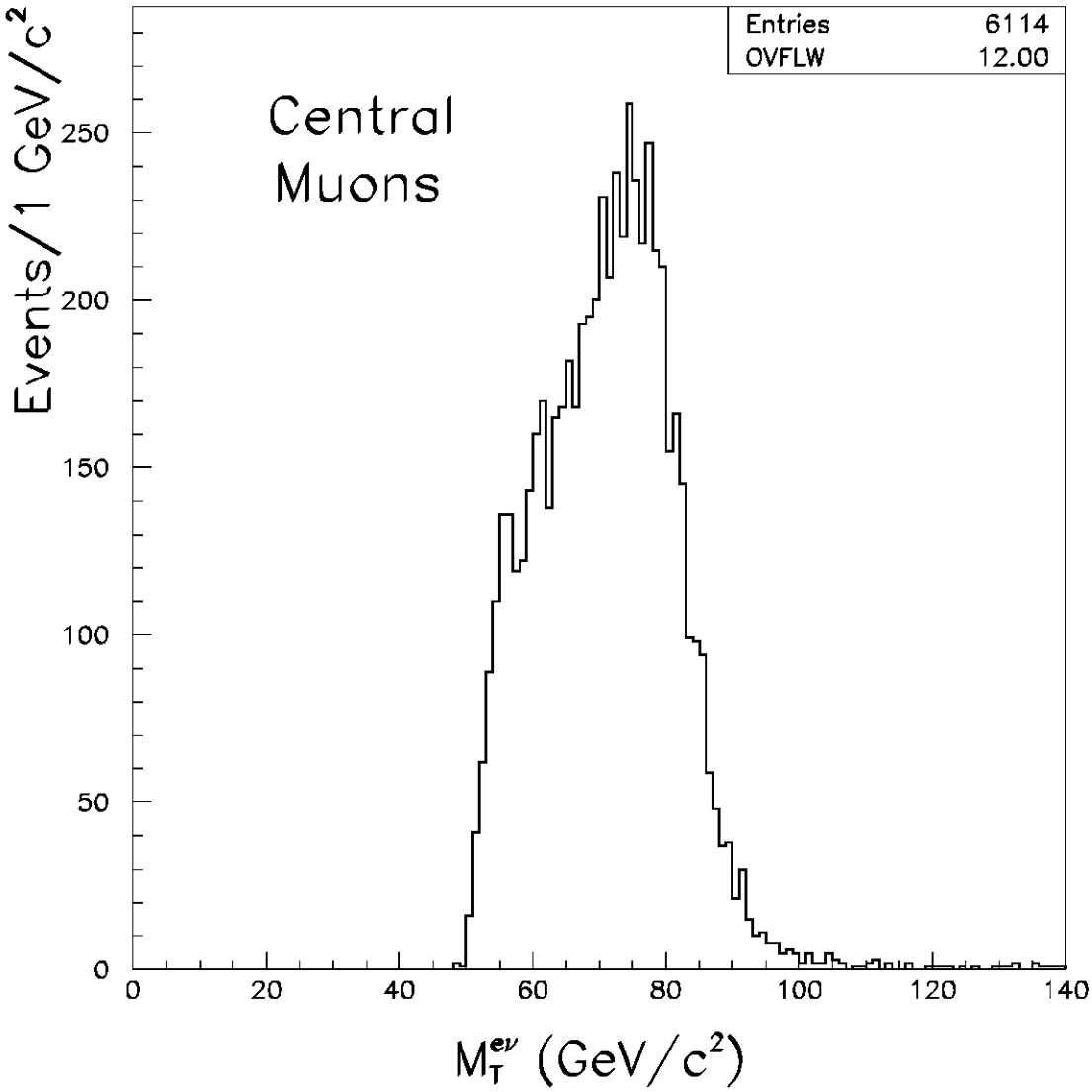

Figure 5.2: The transverse mass spectrum of the central muon W candidates used in the asymmetry analysis.

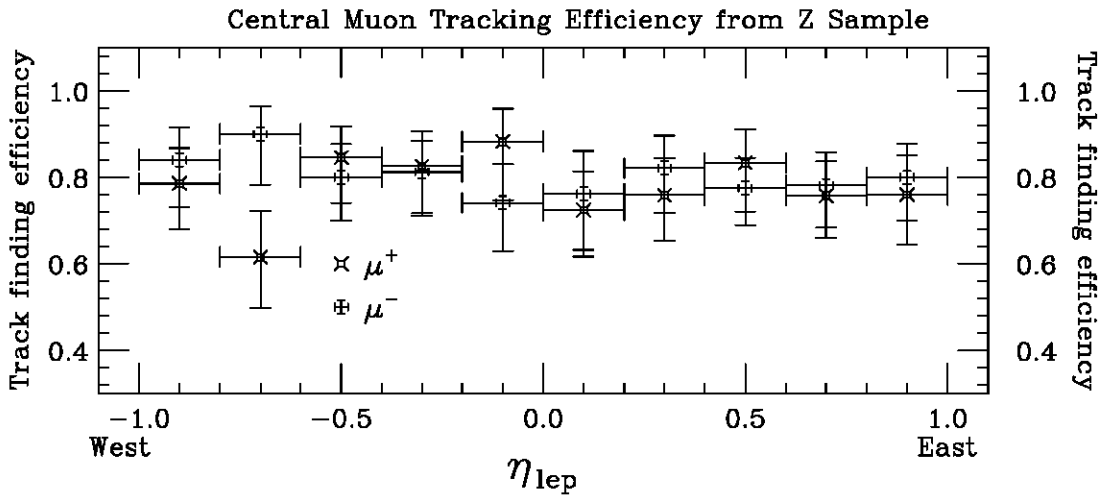

Figure 5.3: The charge independence of tracking in the central muon sample as determined using the second (unbiased) leg of central-central $Z \to ee$ events. The charge of the track is determined by the first leg. The average efficiencies are given in Table 5.1

	ϵ^+	ϵ^-	ϵ^{tot}
Track West	$78\% \pm 4\%$	$81\% \pm 4\%$	$80\% \pm 3\%$
Track East	$76\% \pm 4\%$	$79\% \pm 4\%$	$78\% \pm 3\%$
Track Total	$77\% \pm 3\%$	$80\% \pm 3\%$	$79\% \pm 2\%$
Stub Finding	$56.3\% \pm 3\%$	$58.6\% \pm 3\%$	$57.5\% \pm 2\%$

Table 5.1: (a) Central track finding efficiencies for the tracking cuts employed in the muon analysis. (b) The muon stub finding efficiencies (not corrected for the geometric acceptance of the muon chambers) are found using central-central $Z \to \mu\mu$ events. Only the relative differences between ϵ^+ and ϵ^- are relevant and none are found.

been systematically different.

To check for evidence of a charge bias in the muon stub reconstruction, a sample of $Z \to \mu\mu$ events were selected by requiring only one muon stub. The second muon was identified by a high P_T track pointing at a calorimeter tower which contained energy consistent with the passage of a minimum ionizing particle. The invariant mass of the two muon candidates was required to be within 15 GeV of the Z mass. The efficiency for finding a muon stub associated with the second high P_T track is shown in Table 5.1

	ϵ^+	ϵ^-	ϵ^{tot}
CMU $\lvert\delta X\rvert$	$97.5\%^{+.6\%}_{-.7\%}$	$97.9\%^{+.5\%}_{-.7\%}$	$97.7\%^{+.4\%}_{-.5\%}$
CMP $\lvert\delta X\rvert$	$99.1\%^{+.4\%}_{-.6\%}$	$98.9\%^{+.4\%}_{-.6\%}$	$99.0\%^{+.3\%}_{-.4\%}$
CMX $\lvert\delta X\rvert$	$98.3\%^{+1\%}_{-2\%}$	$97.5\%^{+1.4\%}_{-2.4\%}$	$97.9\%^{+0.9\%}_{-1.4\%}$
$\lvert D_0\rvert$	$99.3\%^{+.3\%}_{-.4\%}$	$99.6\%^{+.2\%}_{-.4\%}$	$99.4\%^{+.2\%}_{-.3\%}$
Isolation	$99.4\%^{+.3\%}_{-.4\%}$	$99.8\%^{+.2\%}_{-.3\%}$	$99.6\% \pm 0.2\%$
Total	$98.5\%^{+.4\%}_{-.5\%}$	$98.9\%^{+.4\%}_{-.5\%}$	$98.7\% \pm 0.3\%$
Cosmic Ray Cut	$99.5\%^{+.2\%}_{-.4\%}$	$99.4\%^{+.3\%}_{-.4\%}$	$99.5\% \pm 0.2\%$

Table 5.2: Central μ efficiencies from tight central $W \rightarrow \mu\nu$ events.

for the East and West halves of the detector. No evidence of a charge bias in track quality cuts or the track-stub matching is found.

5.3 Central Muon Efficiencies

As in the electron data, a sample of $W \rightarrow \mu\nu$ events satisfying tight kinematic cuts (see page 40) was selected from the stream 2 muon data set. Figure 5.4 shows the distributions of μ^+ and μ^- events before the cuts were applied. The matching cuts used in the creation of the data set from which these events were selected were very loose and do not bias the efficiencies. Table 5.2 lists the efficiencies for the muon i.d. cuts. No charge dependent effects are evident.

5.4 Central Muon Backgrounds

5.4.1 QCD

In general, muon candidates are required to pass through at least 5 absorption lengths of material and form a stub which matches a high P_T track in the CTC. Therefore the

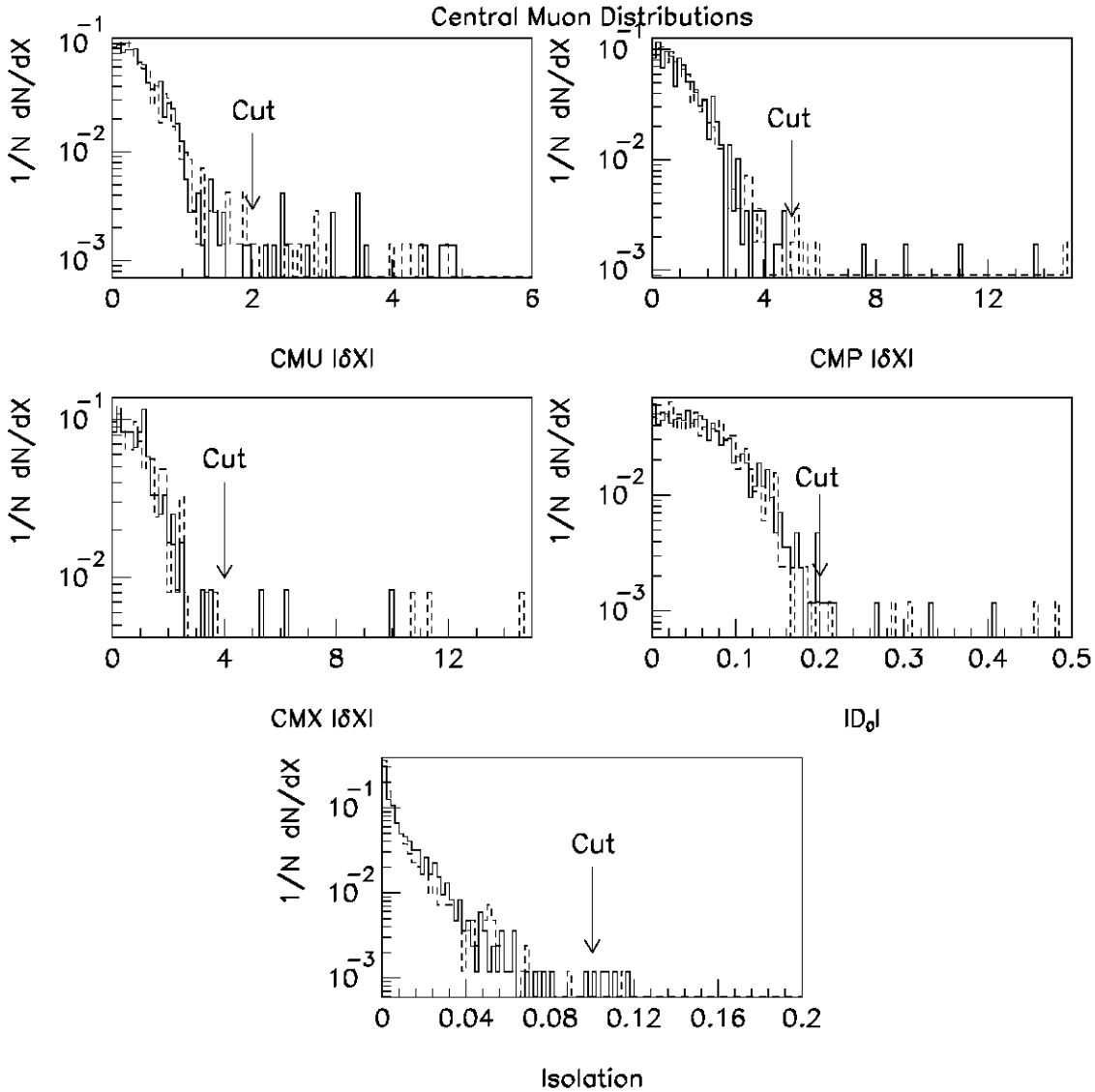

Figure 5.4: Distributions of the central μ i.d. variables from tight $W \rightarrow \mu\nu$ events. The solid histograms are for μ^+ and the dashed for μ^-. As expected the distributions are the same for the two charges. The arrows indicate the value at which the cuts were applied.

backgrounds from QCD jets are much smaller in the muon than in the electron data. The primary means by which QCD jets contaminate the $W \rightarrow \mu\nu$ data are: the "decay in flight" of a pion or kaon into a muon and the "punch-through" of a charged hadron into the muon chambers. Again the E_T^{jet} cut reduces these backgrounds, as does the impact parameter cut. The muon sample has less background from conversions because the higher muon mass suppresses γ ray and pair production processes.

The determination of the QCD background in the muon data was made using the identical method as was used in the electron sample (see page 42). Figure 5.5 shows the *Isolation* versus $\not\!\!E_T$ scatter plot for the high P_T muon data before these cuts were applied. Also shown is the average *Isolation* as a function of $\not\!\!E_T$. As is the case for electrons, the two variables are uncorrelated at low $\not\!\!E_T$ (where there are few W events), implying the extrapolation into the high $\not\!\!E_T$ region is valid. The QCD background estimates made using the two control samples are $(0.34 \pm 0.08)\%$ and $(0.30 \pm 0.08)\%$ for samples of type 1 and 2 respectively (see page 42). Taking the average and interpreting the difference as a systematic error, the QCD background is estimated to be $(0.3 \pm 0.1)\%$ of the $W \rightarrow \mu\nu$ sample.

5.4.2 Cosmic Ray

Unlike the case for electrons, cosmic rays are a potential source of background in the muon data sample. The second track cut ($P_T^{high} < 10$ GeV), the impact parameter cut ($|D_0| < 0.2$ cm) and the Z_0^{track} cut in combination help to reduce the cosmic ray background. In addition to these cuts, the standard CDF cosmic ray filter [35, 36] was run on the muon data sample. This filter rejected events which had a track,

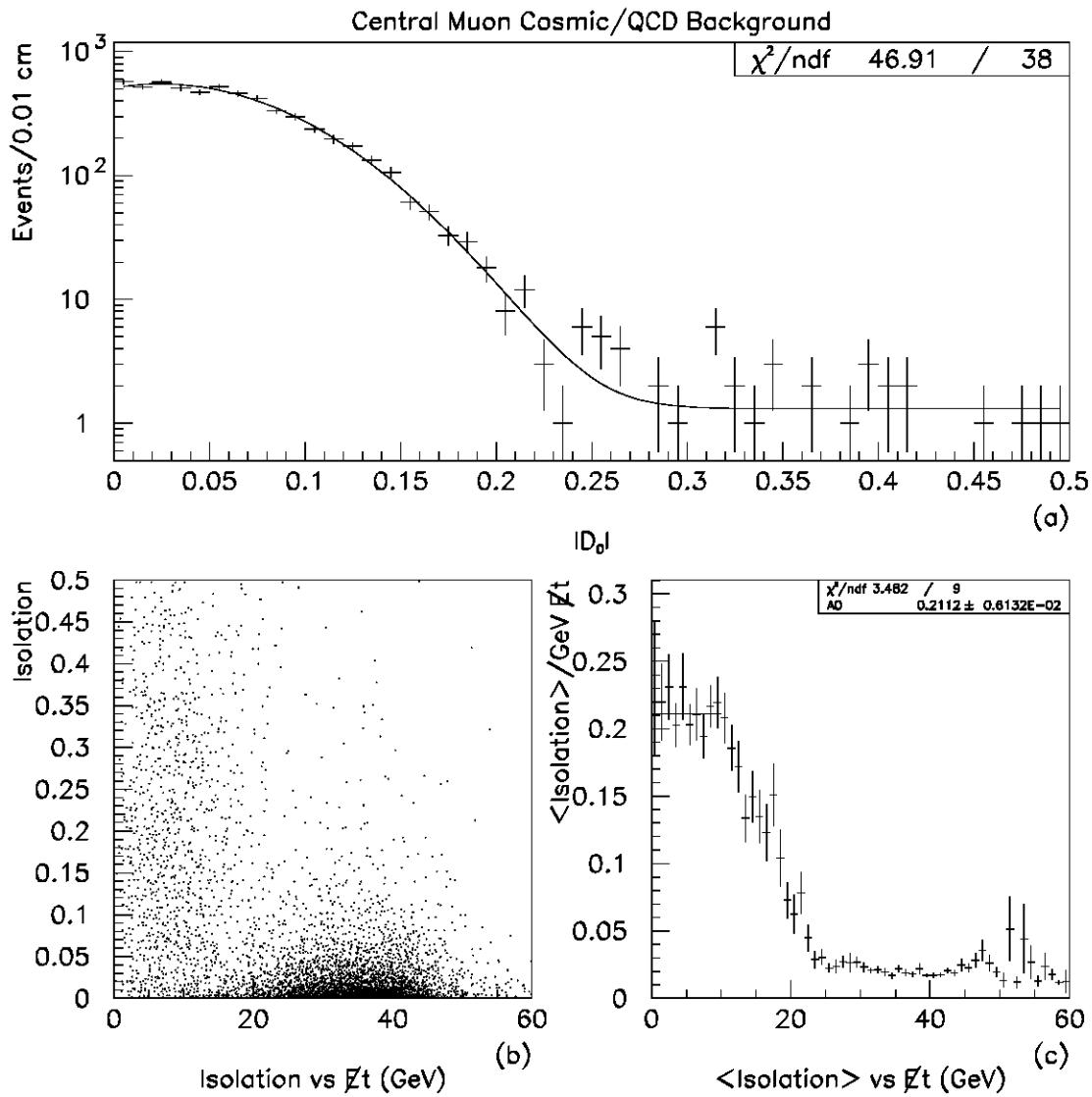

Figure 5.5: a) The impact parameter distribution is used to estimate the cosmic ray contamination in the region $|D_0| < 0.2$ cm. b) The isolation in a cone of 0.4 versus the corrected $\not\!\!E_T$, and c) the average isolation (per GeV) versus $\not\!\!E_T$. The isolation distribution in the region $\not\!\!E_T < 10$ GeV is used to extrapolate from the non-isolated region into the $Isolation < 0.1$ region for $\not\!\!E_T > 25$.

reconstructed in two (r-ϕ) or three dimensions, with $P_T > 10$ GeV and ϕ within 2° of being back-to-back with the identified muon track. These cuts removed the vast majority of cosmic ray events.

The impact parameter distribution is flat for cosmic rays; therefore one can use the tail of this distribution to estimate the contamination in the signal region ($|D_0| < 0.2$). Figure 5.5 shows the impact parameter distribution fitted to a *gaussian* + *constant*. Extrapolating the constant term into the signal region leads to an estimate of a cosmic ray contamination of $(0.5 \pm 0.1)\%$ of the $W \rightarrow \mu\nu$ data sample.

5.4.3 Vector Boson

The backgrounds due to $W \rightarrow \tau\nu$, $Z \rightarrow \mu^+\mu^-$ and $Z \rightarrow \tau\tau$ were determined using Monte Carlo calculations which were normalized to the $W \rightarrow \mu\nu$ data in an identical manner to that described for the central electron sample on page 46. The major difference between the muon and electron data is that the $Z \rightarrow \mu^+\mu^-$ background is larger than the $Z \rightarrow ee$ case.

$W \rightarrow \tau\nu$

As in the electron case, a fast Monte Carlo generator and detector simulation [27] was used to estimate the τ background in the muon sample. The background was found to be essentially identical to that in the electron data; $bg^\tau = (2.0 \pm 0.2)\%$ of the central muon data is estimated to originate from τ decays. The uncertainty was found by using different PDF's in the simulation (the statistical error in the Monte Carlo sample is very small).

$Z \rightarrow \mu^+\mu^-$

Unlike the electron case, this process produces a relatively large background to the W events. This is because only the P_T^{high} cut rejects this background. If the second muon's track is not reconstructed in the CTC, the muon remains essentially invisible in the plug and forward calorimeters and thus escapes and results in a fake $\not{E}_T$. Using the same fast Monte Carlo, which incorporates the plug tracking efficiencies (see Appendix C), the Z background was estimated to be $(4.7 \pm 0.7)\%$ of the $W \rightarrow \mu\nu$ data sample. The error is due to a $\pm 10\%$ uncertainty from the choice of PDF, and another $\pm 10\%$ is from the uncertainty in the tracking efficiency in the plug region.

$Z \rightarrow \tau^+\tau^-$

The HERWIG Monte Carlo generator plus the full detector simulation was used to estimate this background. As in the electron cases, it was found to be negligible, with $bg^{Z\rightarrow\tau\tau} = (0.07 \pm 0.01)\%$ of the central muon data sample. The error on this background is primarily from the statistics in the Monte Carlo samples.

Because the $Z \rightarrow \tau^+\tau^-$ background is very small it was ignored. The backgrounds due to $Z \rightarrow \mu^+\mu^-$, $W \rightarrow \tau\nu$, QCD and cosmic rays has been corrected for in the final W charge asymmetry determination. However, all of these corrections end up being very small when compared to the present statistical uncertainties.

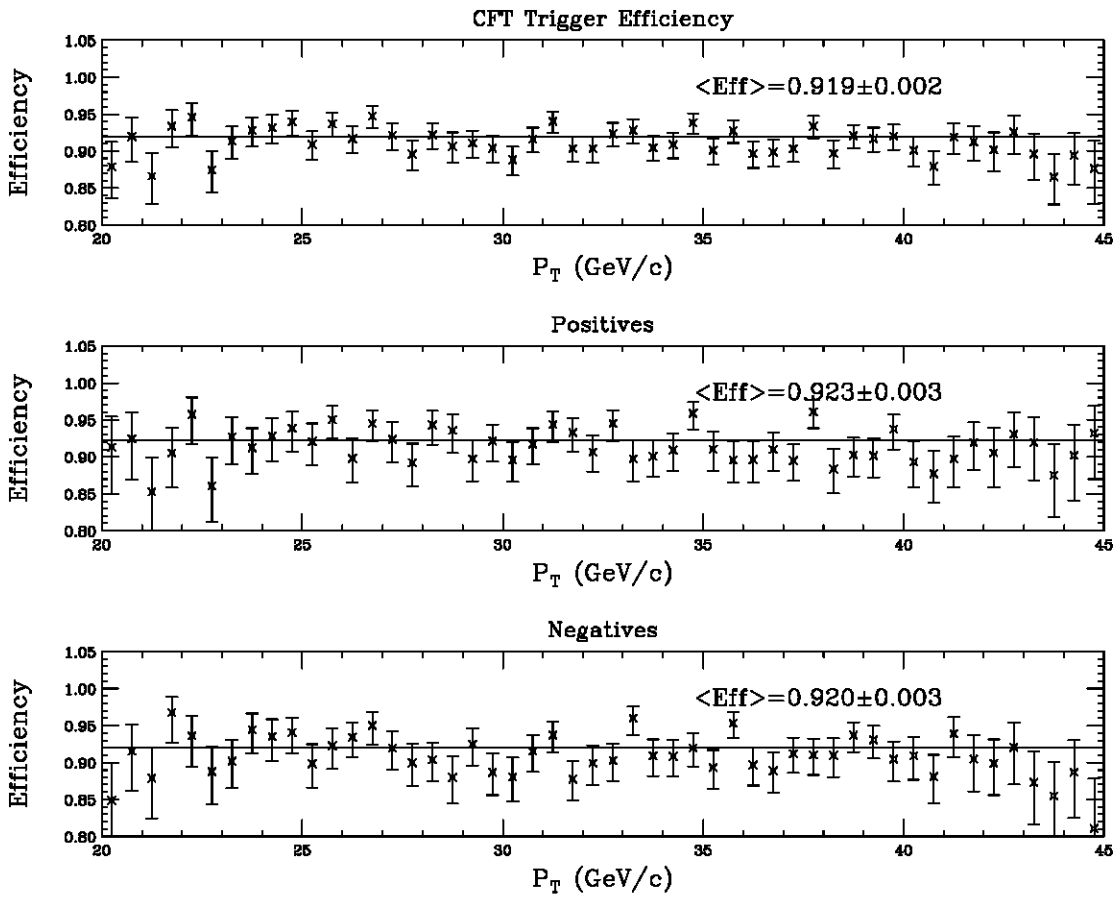

Figure 5.6: The efficiency of the CFT based trigger as a function of P_T and charge of the tracked lepton. The curves show that this trigger is flat in P_T and is charge independent for leptons with $P_T > 25$ GeV.

5.5 The High P_T Muon Trigger

The four drift planes of the muon chambers were located between two layers of scintillator. At trigger level one a coincidence was required between these scintillators. Also the timing from two of the drift chambers was used to determine if the trajectory was consistent with a 6 GeV (P_T) muon which originated from the beamline. If the muon passed through the CMU, coincident hits were required in the CMP, and if the muon was found in the CMX, the P_T threshold was raised to 10 GeV.

At level two a match, in the r-ϕ plane, between a CFT track with $P_T > 9.2$ GeV and the muon stub was required. Since the tracks produced by a muon and an electron are essentially identical, the central $W \rightarrow e\nu$ data are used to verify the charge and P_T independence of the CFT trigger above $P_T = 25$ GeV. These electrons were accepted by a $\not{E}_T$ trigger which is independent of the CFT. Figure 5.6 shows the efficiency of the CFT trigger as a function of lepton P_T and charge. The data points are well fit by a straight line and there are no differences between the positively and negatively charged leptons. Therefore no corrections to the asymmetry from possible biases in the muon trigger are needed.

Chapter 6

The $W \rightarrow l + \nu$ Charge Asymmetry

The charge asymmetry measurement is a very robust measurement once the charge independence of the various selection criteria has been established. One remaining source of systematic error is from detector effects and is related to the E_T (or P_T) cut used in the data selection. This error can come about if either the trigger has an E_T (P_T) dependence, or the energy (momentum) scale is incorrect. The second source of a systematic error in the asymmetry measurement is the presence of backgrounds in the data sample. Small corrections were made for each source of systematic error and the error included in the total systematic uncertainty. When all systematic errors are combined the total error is still dominated by the statistics available in the 1992-93 run of the Tevatron.

As shown in the previous chapters the efficiencies for l^+ and l^- ($l = e$ *or* μ) are equal; therefore Equation 1.5 can be written as:

$$A(y_l) = \frac{N^+(y_l) - N^-(y_l)}{N^+(y_l) + N^-(y_l)},$$

where N^+ (N^-) is the number positive (negative) W decay leptons found at a lepton rapidity of y_l. However, there are backgrounds in the W samples, and the plug data will require a correction for its trigger efficiency's E_T dependence. To account for the backgrounds and trigger correction, the charge asymmetry can be rewritten in terms of the asymmetries and fractional size of the backgrounds contained in the data as follows:

$$A = \frac{A^{obs} - A^{\tau} bg^{\tau} - A^{Z} bg^{Z} - A^{QCD} bg^{QCD} - A^{Cosmic} bg^{Cosmic}}{1 - bg^{\tau} - bg^{Z} - bg^{QCD} - bg^{Cosmic}}, \tag{6.1}$$

where the y_l dependence is assumed, and

$A^{obs} = A^{raw} + C^{trig}$ is the observed asymmetry after correcting for trigger effects,

$bg^x = N^x/N_{tot}$ is the fraction of background ($x = \tau$, Z, QCD or Cosmic rays) contained in N_{tot} $W \rightarrow e\nu$ candidates, and

A^x is the asymmetry of the background.

Therefore it is necessary to determine the shapes of all the backgrounds contained in the data as well as their fractional size. In this section, first the C^{trig} corrections and the uncertainty due to the energy/momentum scales are described, followed by a description of the asymmetries of the backgrounds. The background asymmetries when combined with the previously determined fractional backgrounds (bg^x's) yield the final fully corrected charge asymmetry.

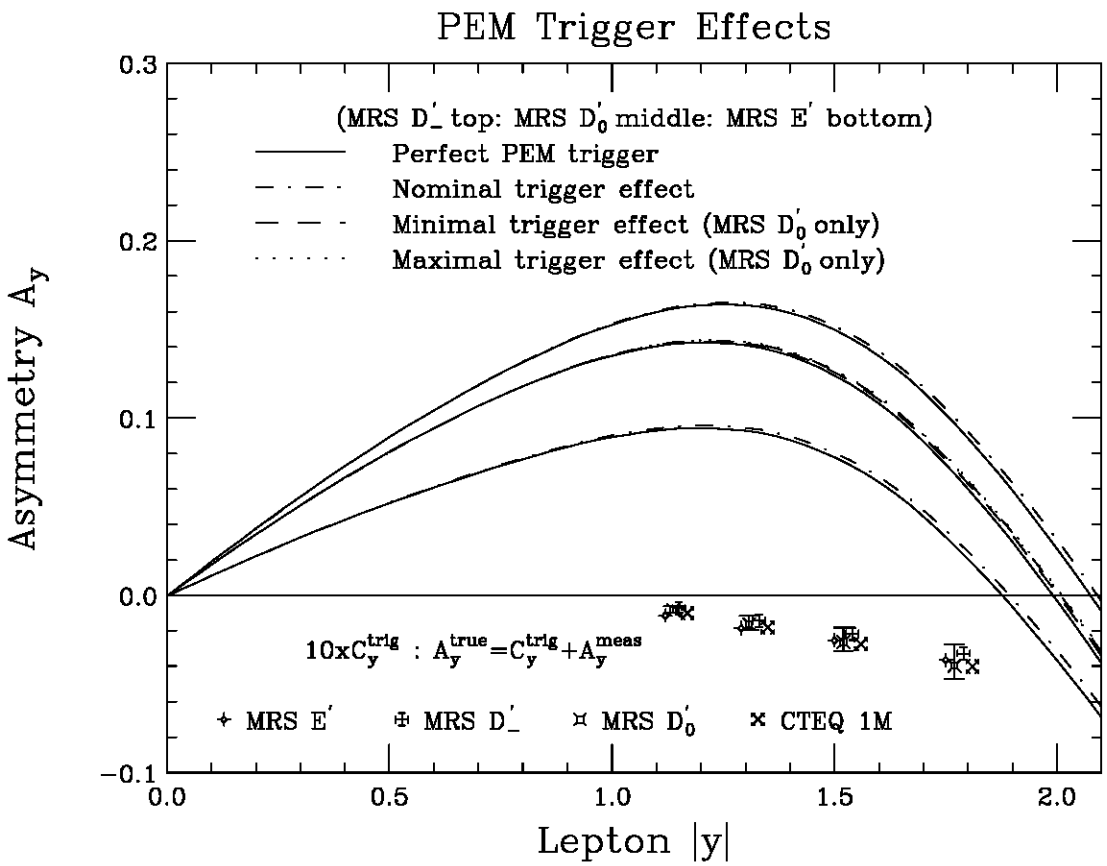

Figure 6.1: The effect of the plug trigger efficiency (the difference between the solid and dot-dash lines) as determined by several choices of PDF. The additive corrections (multiplied by 10) are shown in the bottom half of the plot.

6.1 Detector Related Systematic Errors

Trigger Effects

The first correction that was applied to the data was for trigger effects. As described earlier the central electron and muon triggers require no corrections (see pages 48 and 81), only the plug electron trigger exhibits an E_T dependence. Using the efficiency curve for the combined plug W triggers (see page 64) as a weighting function, the asymmetry was calculated and compared to the unweighted results. Figure 6.1 shows the

$\|\eta\|$	$\langle\eta\rangle$	$C^{trig}(y)$
1.0-1.2	1.14	-0.0008 ± 0.00024
1.2-1.4	1.31	-0.0016 ± 0.0005
1.4-1.7	1.52	-0.0026 ± 0.0008
1.7-2.0	1.77	-0.0040 ± 0.0012

Table 6.1: Asymmetry corrections (additive) for the plug electron trigger.

correction factors (multiplied by a factor of 10) that were added to the raw asymmetry in the plug region. Table 6.1 lists these same corrections, calculated at the average η of the data in each plug electron bin, which were added to the raw plug electron charge asymmetry. The uncertainties in the corrections were determined using the uncertainty in the efficiency curve. In addition different sets of parton distributions were used to check that the corrections were valid over a reasonable range of predicted A(y). We find that the correction is < 0.005 in units of A(y) and is only weakly dependent on the PDF's used in the calculation, as shown in Figure 6.1.

Energy/Momentum Scale Effects

Any uncertainty in the energy (momentum) scale translates into an uncertainty in the asymmetry determined using the electrons (muons) when compared with predictions. The electron energy scales in the central and plug calorimeters were known to better than $\pm 1\%$, and the momentum scale was determined to be better than $\pm 0.1\%$ for muons. However, the muon momentum measurement does not account for any loss of radiated photons, because the energy in the tower associated with the muon is removed before the final $\not{E}_T$ is calculated. A comparison of generated $W \to \mu\nu$ events where the muon is not allowed to radiate to events where the muon is allowed to radiate indicates that,

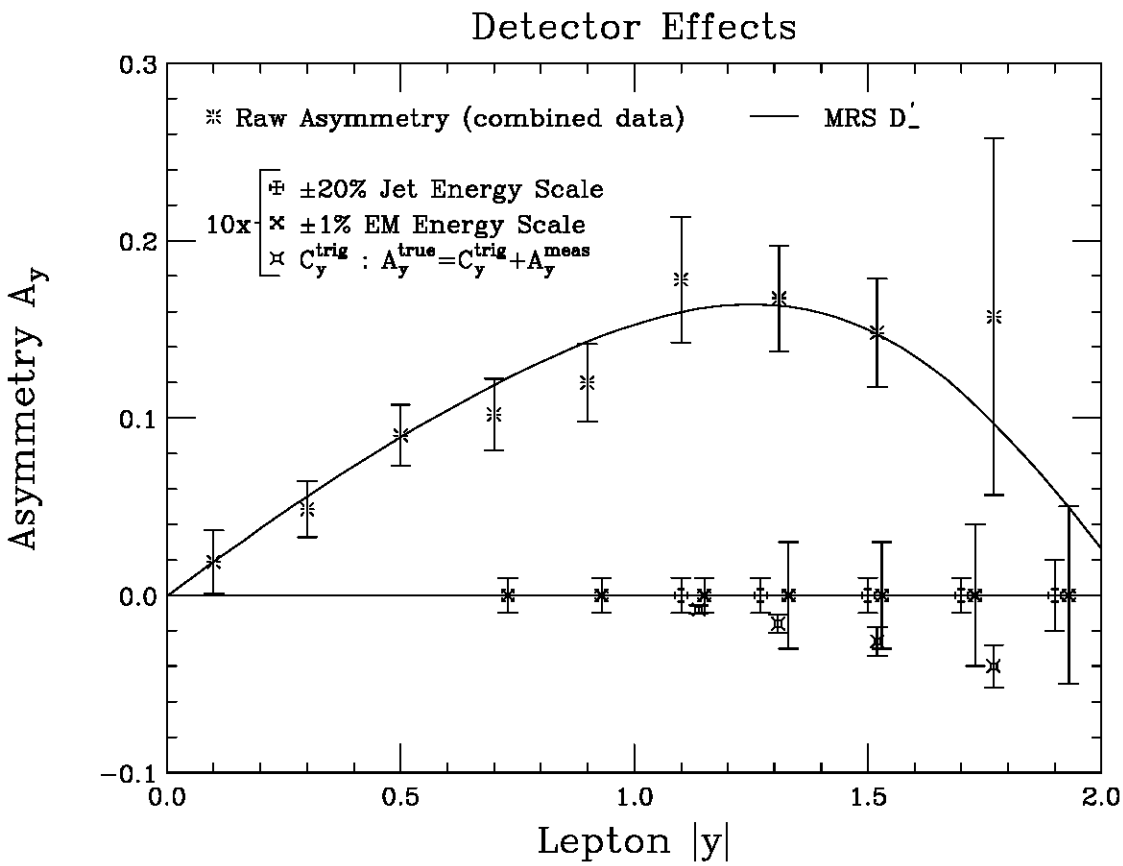

Figure 6.2: The uncertainties in the asymmetry due to the EM and Jet energy scales and the correction due to the plug trigger efficiency (all multiplied by a factor of 10) compared to the raw asymmetry (data) and its statistical errors.

on average, P_T^μ decreases by about 100 MeV. The exact value depends on the amount of material in the tracking volume. Therefore, if the 1% uncertainty used in the electron case is applied to the muon data for simplicity, it will more than cover this 100 MeV loss from the radiated photons.

To check that the asymmetry is only weakly sensitive to the jet E_T cut (essentially a P_T^W cut), it was varied by $\pm 20\%$ in the NLO calculation. This is a very conservative estimate of the uncertainty in the jet energy scale (thought to be good to about 10%).

Source	Central e	Plug e	Central μ
$W \rightarrow \tau\nu$	$\mathbf{2.0 \pm 0.2}$	$\mathbf{2.0 \pm 0.2}$	$\mathbf{2.0 \pm 0.2}$
QCD	$\mathbf{0.4 \pm 0.1}$	$\mathbf{4.1 \pm 0.9}$	$\mathbf{0.3 \pm 0.1}$
Cosmic Rays	—	—	$\mathbf{0.5 \pm 0.1}$
$Z \rightarrow e\ or\ mu$	< 0.2	< 0.2	$\mathbf{4.7 \pm 0.7}$
$Z \rightarrow \tau\tau$	< 0.1	< 0.1	< 0.1

Table 6.2: Backgrounds (%) in the $W \rightarrow e\nu$ and $W \rightarrow \mu\nu$ charge asymmetry event samples. The values in boldface were used to correct the measurement in conjunction with the background's charge asymmetry.

Even this conservative estimate was found to have very little effect on the asymmetry (< 0.001 in units of asymmetry), so this error was ignored. Figure 6.2 summarizes the detector related corrections and uncertainties (all multiplied by a factor of 10 to make them visible). To set the scale, the raw asymmetry from the data along with its statistical errors is also shown (the curve is the MRS D'_- prediction). These effects are found to be of order one tenth the statistical error.

6.2 Background Related Systematic Errors

To determine the effect of the backgrounds in the W samples one must estimate the backgrounds' charge asymmetry. Backgrounds due to $W \rightarrow \tau\nu$ and Z production are asymmetric. Backgrounds from QCD processes (see pages 42 and 75) and cosmic rays are charge symmetric, and therefore tend to dilute the measured asymmetry. Table 6.2 summarizes the various backgrounds and their errors.

QCD

The asymmetry in QCD type backgrounds is expected to be zero. To check this assumption the asymmetry was measured for electrons (i.e. an EM cluster passing all the electron i.d. cuts) found in the low $\not{E}_T$ jet sample. The average asymmetry was found to be 0.001 ± 0.01, confirming the assumed asymmetry, $A^{QCD} = 0$. Therefore the correction for the QCD background increases the asymmetry by $\approx bg^{QCD} * A(y)$ (Equation 6.1 is used to correct the asymmetry for all the backgrounds). The error due to this correction is dominated by the statistics in the bg^{QCD} determination.

Cosmic Ray

The muons selected for this analysis were all required to have P_T greater than 25 GeV; therefore it is not expected that the cosmic ray muons will exhibit a large charge asymmetry (at lower energies cosmic rays do exhibit a charge asymmetry). A sample of cosmic rays, which pass the asymmetry analysis cuts, was selected from the muon data using the standard CDF cosmic ray filter (see page 77). The charge asymmetry of 558 events was found to be -0.01 ± 0.04, consistent with zero. Therefore it was assumed that $A^{Cosmic} = 0$.

$W \rightarrow \tau\nu$

The largest background in the central $W \rightarrow e\nu$ data is due to $W \rightarrow \tau\nu$ followed by a τ decay to an electron. The charge asymmetry of the $W \rightarrow \tau\nu$ is identical to that for electrons and muons. The differences are caused primarily by the softening of the observed lepton's E_T; in essence a cut at $E_T = 25$ GeV on the e or μ from

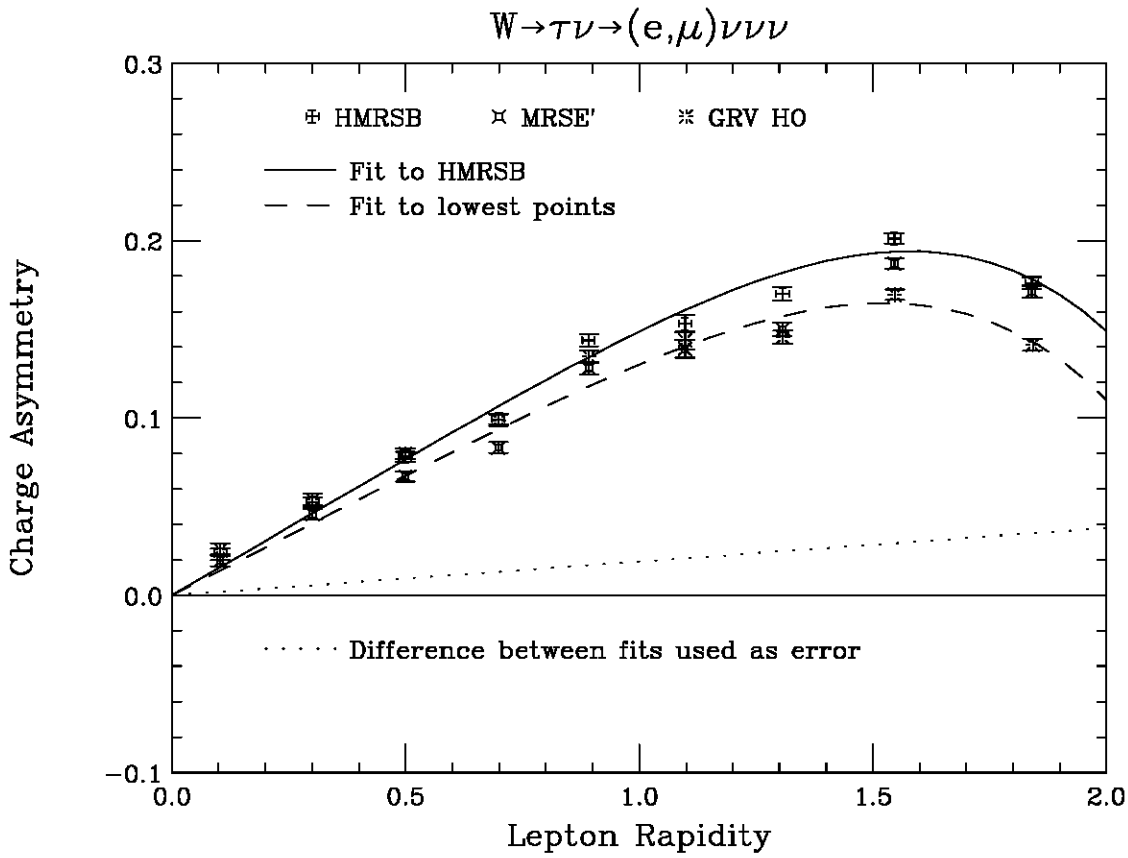

Figure 6.3: The asymmetry of the $W \to \tau\nu$ background. The uncertainty is determined by the difference between the HMRSB curve and the lowest set of points (a combination of GRV and MRSE).

the τ decay corresponds to a much higher cut on P_T^τ. Figure 6.3 shows a fit to the asymmetry from $W \to \tau\nu \to (e \ or \ \mu)\nu\nu\nu$ events calculated using the HMRSB parton distributions in conjunction with a LO Monte Carlo [27], which handled the W and τ polarizations correctly and added the appropriate P_T to the W. Also shown are asymmetry values calculated using the MRS E′ and GRV HO PDF's. The set of lowest predicted asymmetries was then fit to determine a conservative error on the HMRSB fit, which was used to correct the asymmetry. The size of the correction is $\approx bg^\tau(A(y) -$

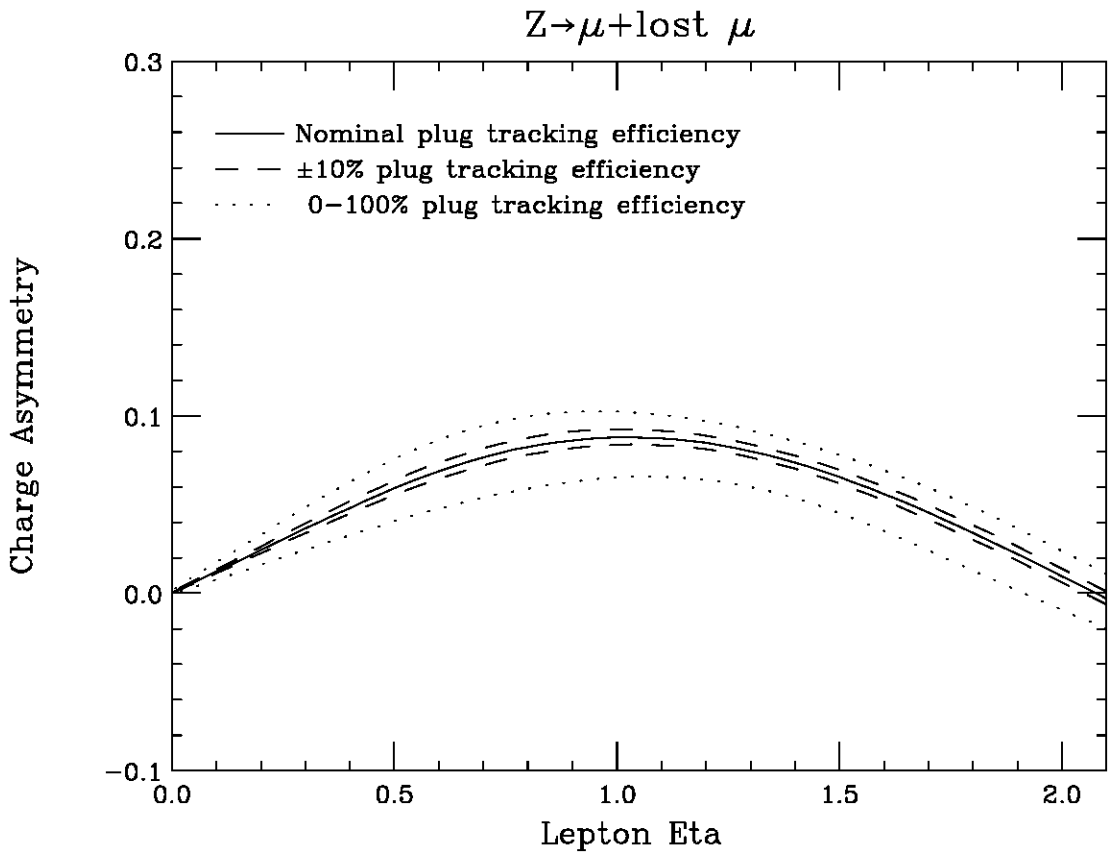

Figure 6.4: The charge asymmetry due to losing one leg of a $Z \to \mu^+\mu^-$. Varying the track finding efficiency $\pm 10\%$ changes the asymmetry $\pm 5\%$ for $|\eta| < 1.3$.

$A^\tau(y)$). It is found that $A(y)$ and $A^\tau(y)$ are very close until the V-A decay forces the asymmetry to turn over at $|\eta| \sim 1.0$ (see Figure 6.5). Thus the τ background will only have a very small effect on the central data.

$Z \to \mu\mu$

Z decays have a natural asymmetry which goes in the opposite direction to that of the W's, in the region where the measurement can be made. This is because the Z's charge asymmetry is due solely to its decay; PDF's do not contribute to the Z

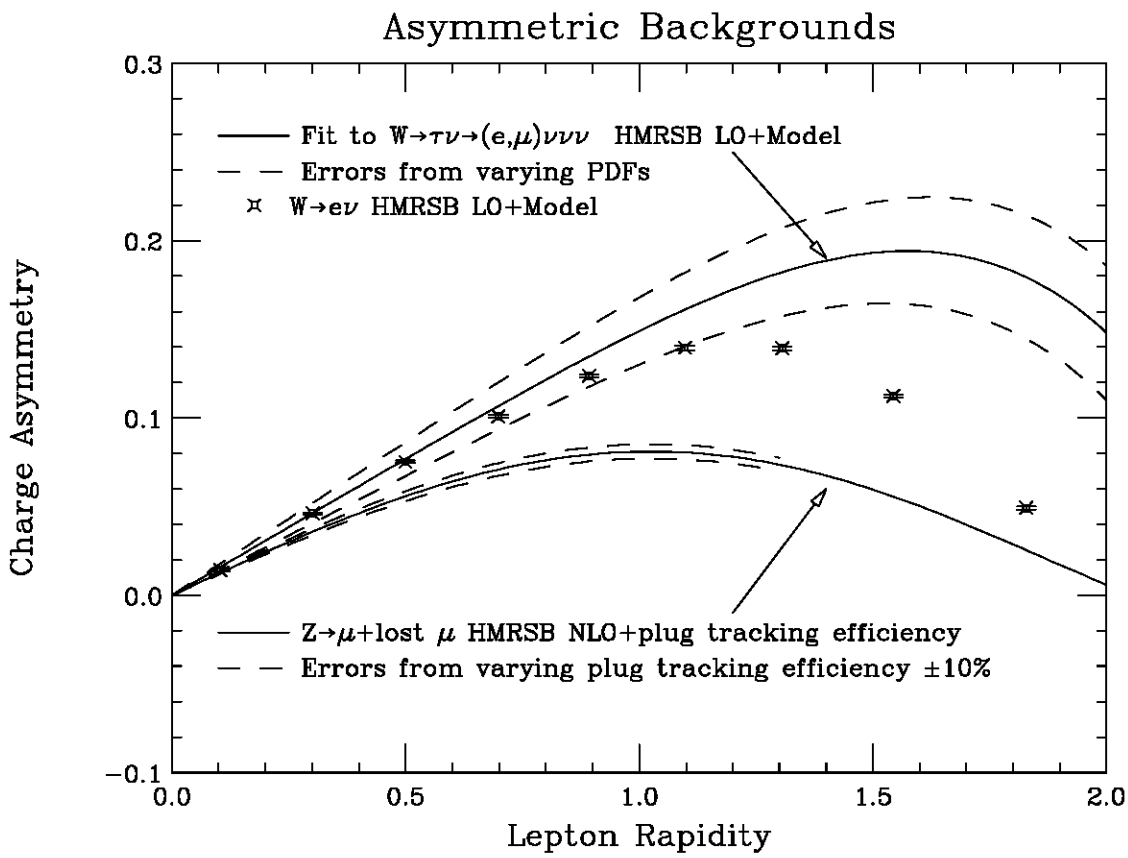

Figure 6.5: The charge asymmetries (and their uncertainty) of the backgrounds relative to that of $W \to e\nu$.

asymmetry. In the case of electrons, the background due to losing one of the Z decay electrons is very small and was ignored. However, in the μ channel it is the largest background. The effect of missing the second muon leads to an observed asymmetry in $Z \to \mu\mu$ events which is similar to that of the W events as shown in Figure 6.4. Therefore a correction of $\approx bg^Z * (A(y) - A^Z(y))$ was made to the muon data sample. The uncertainty in the Z asymmetry is due entirely to the tracking efficiency in the plug region (the variation in $A^Z(y)$ with choices of PDF is very small). Figure 6.4 shows the calculated asymmetry using the nominal plug tracking efficiency (see Appendix C).

Also shown are the effects of varying the efficiency by $\pm 10\%$ and of assuming the most extreme case, 100% and 0% efficiency for the second muon in the region $1.2 < |\eta| < 1.8$. The uncertainty in A^Z out to $|\eta| < 1.3$ is thus determined (using the $\pm 10\%$ efficiency curves) to be $\pm 5\%$. The variation of bg^Z with respect to the plug tracking efficiency is anticorrelated to that of A^Z, leading to an uncertainty in the product $A^Z bg^Z$ of only $\pm 5\%$ (the uncertainty on bg^Z alone from this source is $\pm 10\%$). Figure 6.5 summarizes the background asymmetries and uncertainties which were used to correct the observed charge asymmetry.

6.3 The Corrected Charge Asymmetry

The final corrections to the charge asymmetry have ended up to be very small. To calculate the charge asymmetry due to $W \rightarrow l\nu$, Equation 6.1 was used to correct the raw asymmetry on a bin-by-bin basis. The weighted mean of $+\eta$ and $-\eta$ for the various detectors contributing to a particular bin was calculated. The number of W candidates found in each η bin for the three detectors is shown in Table 6.3. The raw asymmetry calculated in each bin, and the asymmetry found after correcting for the plug trigger and the various backgrounds is given in Table 6.4. Also shown are the corresponding statistical and systematic errors. Note, that extraneous significant figures are kept to illustrate the small corrections and systematic errors. The measurement is clearly statistics limited at present.

Figure 6.6 shows the raw asymmetry found in each bin of the three detectors separately, the asymmetry after the various detectors' data are combined and the asymmetry

$\|\eta\|$ bin	$\langle\|\eta\|\rangle$	+Q/+Y	-Q/-Y	+Q/-Y	-Q/+Y	Total
Central Electrons						
0.0-0.2	0.105	427	446	405	407	1685
0.2-0.4	0.303	519	523	485	482	2009
0.4-0.6	0.500	566	597	461	498	2122
0.6-0.8	0.699	599	553	460	486	2098
0.8-1.0	0.895	456	547	352	417	1772
1.0-1.2	1.060	159	172	109	111	551
Central Muons						
0.0-0.2	0.112	421	394	410	403	1628
0.2-0.4	0.301	580	537	496	498	2111
0.4-0.6	0.479	417	351	304	348	1420
0.6-0.8	0.705	146	123	95	117	481
0.8-1.0	0.894	119	107	92	100	418
1.0-1.2	1.025	15	12	11.	10	48
Plug Electrons						
1.0-1.2	1.138	69	73	52	56	250
1.2-1.4	1.308	340	348	242	252	1182
1.4-1.7	1.520	352	304	238	249	1143
1.7-2.0	1.769	38	32	24	27	121

Table 6.3: Number of W candidates used in the charge asymmetry analysis. There are 10,237 central electrons ($|\eta| < 1.2$), 2696 plug electrons ($1.2 < |\eta| < 2.0$) and 6106 muons ($|\eta| < 1.2$) for grand total of 19,039 $W \to e, \mu + \nu$ candidates.

$\|\eta\|$ bin	$\langle\|\eta\|\rangle$	$A^{raw}(y_l)$	$A^{cor}(y_l)$	σ_{stat}	σ_{sys}	$\sqrt{\sigma_{stat}^2 + \sigma_{sys}^2}$
0.0-0.2	0.109	0.019	0.019	$\pm$0.0180	$\pm$0.0001	$\pm$0.0180
0.2-0.4	0.302	0.048	0.049	$\pm$0.0160	$\pm$0.0003	$\pm$0.0161
0.4-0.6	0.492	0.091	0.092	$\pm$0.0173	$\pm$0.0005	$\pm$0.0173
0.6-0.8	0.700	0.102	0.103	$\pm$0.0203	$\pm$0.0012	$\pm$0.0203
0.8-1.0	0.895	0.125	0.125	$\pm$0.0220	$\pm$0.0012	$\pm$0.0220
1.0-1.2	1.081	0.179	0.182	$\pm$0.0362	$\pm$0.0018	$\pm$0.0362
1.2-1.4	1.308	0.164	0.169	$\pm$0.0299	$\pm$0.0038	$\pm$0.0301
1.4-1.7	1.520	0.148	0.151	$\pm$0.0305	$\pm$0.0038	$\pm$0.0307
1.7-2.0	1.769	0.157	0.159	$\pm$0.1006	$\pm$0.0049	$\pm$0.1007

Table 6.4: Measured charge asymmetry in the combined e and μ channels.

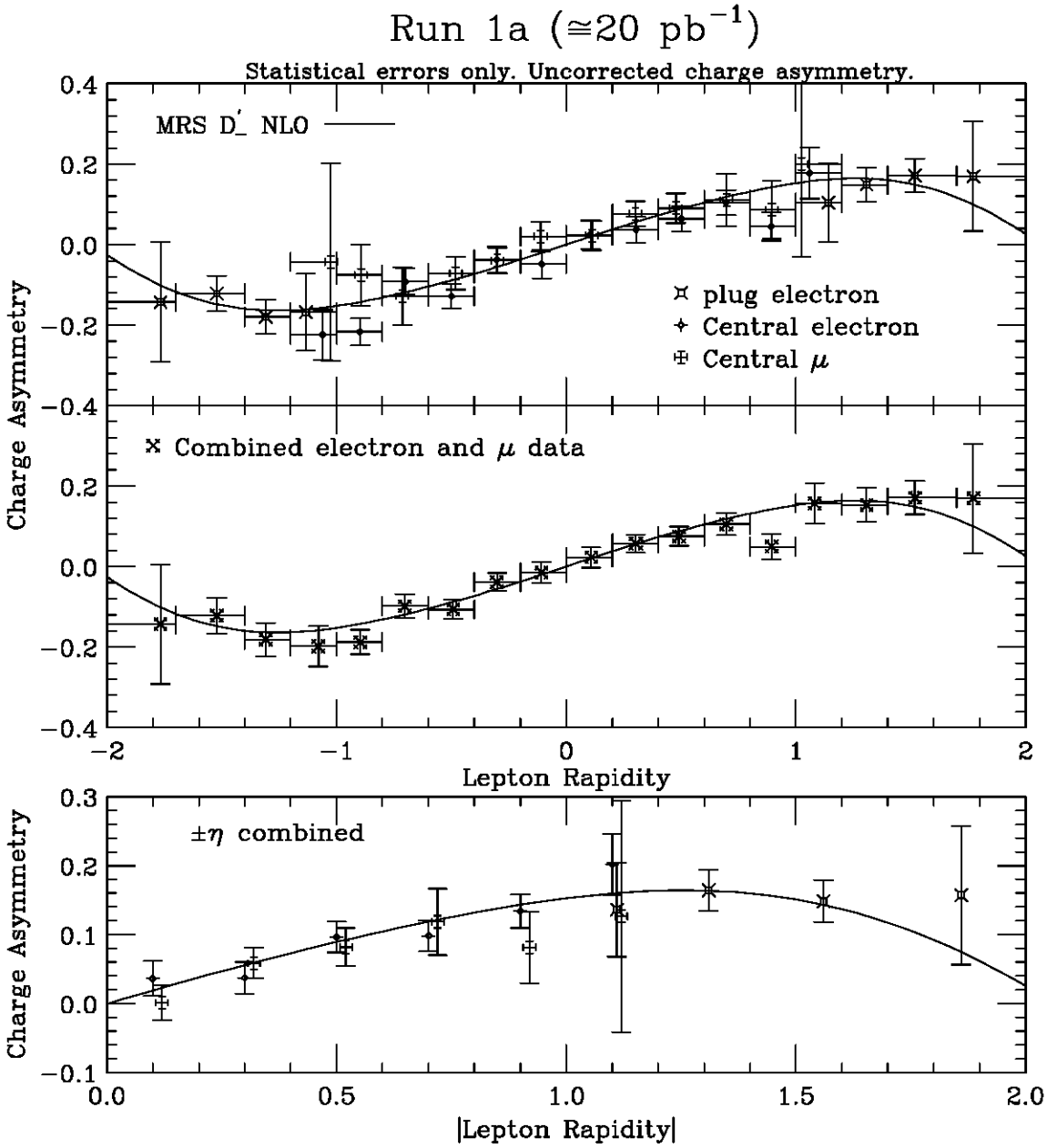

Figure 6.6: The raw (uncorrected) charge asymmetry before the data from the various detectors are combined and/or folded about $\eta = 0$.

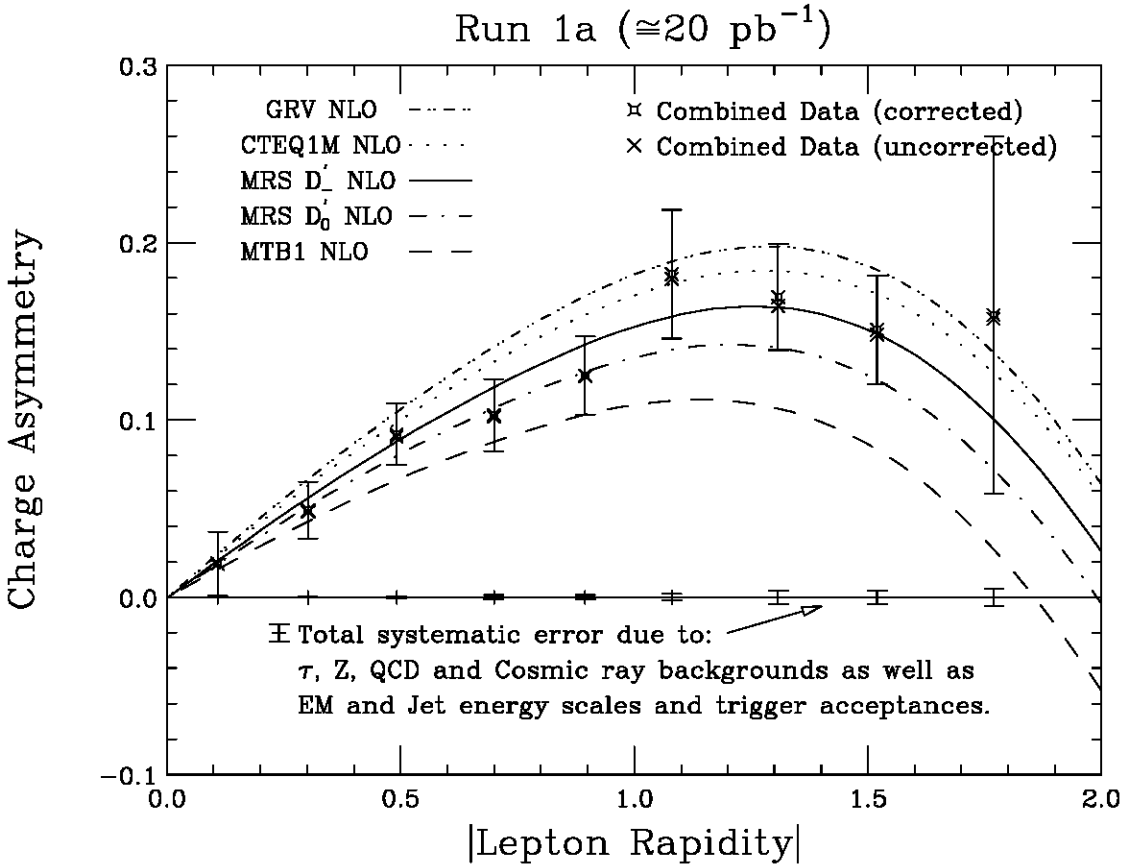

Figure 6.7: The fully corrected charge asymmetry (including tiny systematic corrections) after the data from the various detectors are combined and folded about $\eta = 0$. The error bars along the x-axis show the total systematic errors associated with each bin.

after $+\eta$ and $-\eta$ are combined for the detectors separately. The agreement between the raw asymmetries in the various detectors is very good even though no corrections have been made, and there is no overall shift in the asymmetry as one would expect if there were a difference in the efficiencies for l^+ and l^- (to first order such a shift is removed when $A(-y)$ is folded into $A(+y)$). Clearly the asymmetry is a robust measurement.

Figure 6.7 shows the corrected asymmetry as a function of lepton $|y|$ after all the available CDF data from the 1992-93 run of the Tevatron has been combined. Both

the corrected and uncorrected asymmetry values are shown; the corrections are indeed small. Also shown are the negligible systematic errors associated with each point. The dominant systematic error is due to the EM scale uncertainty. This uncertainty should decrease as more Z's are available to calibrate the PEM. Regardless, even with four times the data (as is expected from the 1994-95 Tevatron run) the measurement's uncertainty will still be dominated by the available statistics.

Chapter 7

What the Asymmetry Says about PDFs

7.1 Theoretical Predictions

When comparing the asymmetry data to predictions, the Dyrad W/Z Monte Carlo [21] has been used. This Monte Carlo calculation makes use of all next-to-leading order matrix elements for the process $p\overline{p} \rightarrow WX \rightarrow l\nu X$. At next-to-leading order (NLO) there can be a jet produced in conjunction with the W. The definition of a jet used in the asymmetry analysis (i.e. energy clustered in a cone of $R = 0.7$ of $E_T^{jet} > 20$ GeV) is included in the calculation. The calculation also reflects the geometric limitations of the detector in that $\not{E}_T$ is determined using only the energy contained in $|y| < 3.6$, and the jet is required to have $|y| < 3.5$. Finally, since the lepton charge asymmetry is sensitive to the kinematic cuts on the leptons, the calculation implements the E_T and $\not{E}_T$ cuts used in the data selection. Beyond these simple kinematic cuts, there is no detector

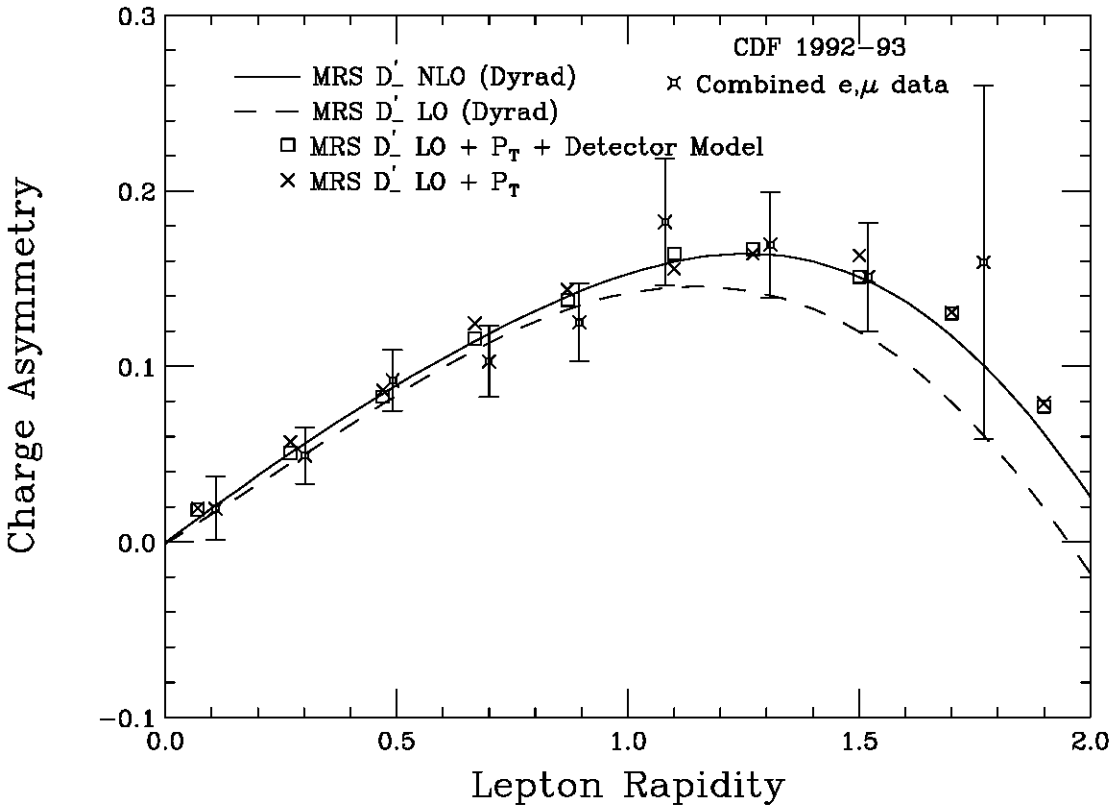

Figure 7.1: The Dyrad NLO charge asymmetry calculation compared with the strictly LO one, i.e. $P_T^W = 0$ (also calculated using Dyrad). The points are from the LO+P_T^W calculation, both with and without a detector model. The symbols are offset slightly in y to make them more visible.

simulation; the electron's (muon's) energy (momentum) is not smeared and there are no dead or inefficient regions and the vertex position is not offset or smeared. Another limitation of the NLO calculation is that, at very low P_T^W, it can not reproduce the observed P_T^W spectrum, which might lead to a bias in the charge asymmetry prediction.

To test the sensitivity of the predicted charge asymmetry to these limitations in the NLO Monte Carlo, a LO calculation [27] was used in which the correct P_T^W spectrum was added. This Monte Carlo included a detector model which incorporated the dead regions of the detector, the calorimeter and tracking resolutions, and it smeared the

interaction point along the z-axis. Figure 7.1 shows the predicted asymmetry found using the NLO calculation, the strict LO calculation ($P_T^W = 0$), the LO+P_T^W calculation and the LO+P_T^W+Detector Model calculation. The points calculated at LO with and without the detector simulation are almost identical, implying that detector resolutions, acceptances and the vertex smearing have little impact on the asymmetry measurement. The good agreement between the NLO and LO+P_T^W predictions also demonstrates that the shape of the P_T^W spectrum (at low P_T) does not influence the asymmetry. Only the strict LO calculation disagrees with the NLO calculation, but even this disagreement is fairly small. In all the calculations, including the LO, we have used the same NLO parton distribution functions (PDF's).

Figure 1.4 showed that the W couplings are known well enough that, in the context of the asymmetry analysis, the V-A assumption is very safe. These plots give one confidence that the calculations are as robust as the charge asymmetry measurement itself. Thus it is possible to draw conclusions on the accuracy of the $d(x)/u(x)$ ratio (see section 1.3) predicted by the various parton distributions from their predictions for the W decay lepton charge asymmetry.

7.2 Comparisons with Predictions

Parton distributions are usually determined by fitting all the existing data which contain information on the quark and gluon momentum distributions. This obviously makes it difficult to check the validity of the assumptions which go into the fits, as by construction, the extracted PDF's agree with all the data. This is where the charge

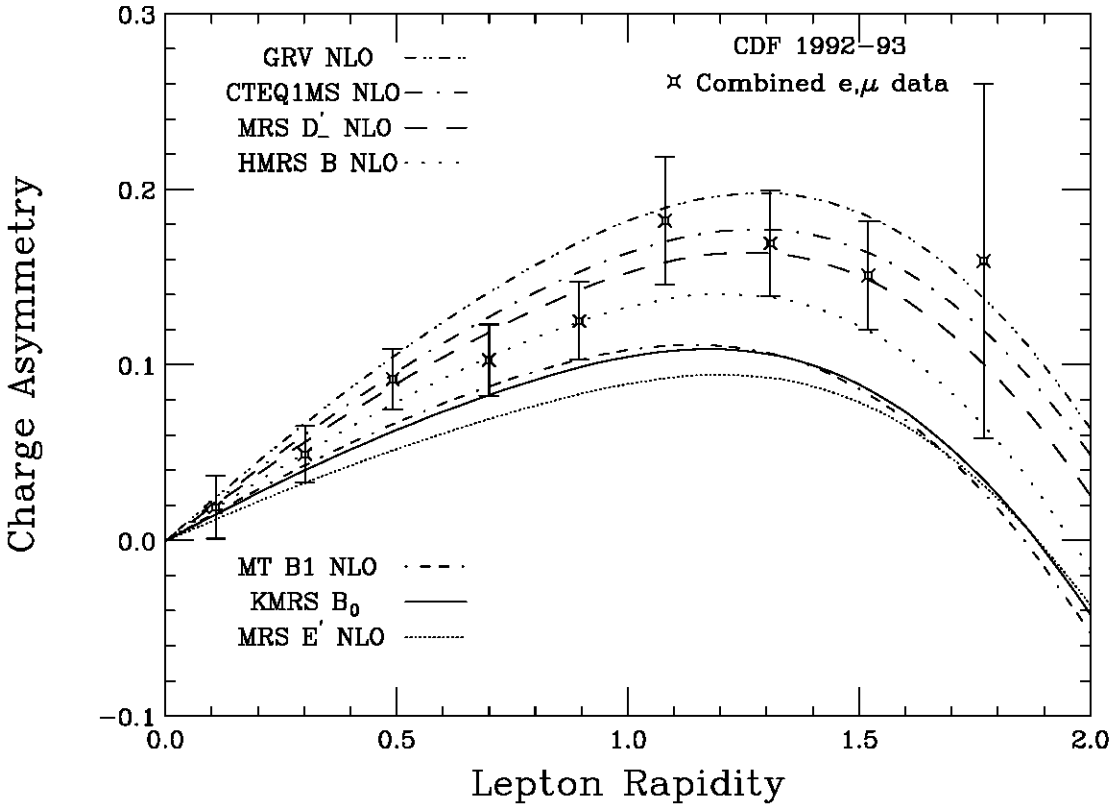

Figure 7.2: The older PDF's tend to predict lower asymmetries than do those which were fit using the recent NMC and CCFR data.

asymmetry is in a unique position; this data was not used in any of the fits, so it provides an independent check.

Figure 7.2 shows the large range of charge asymmetries predicted by the available PDF's. The most recent global analyses are those by Martin, Roberts and Stirling (MRS D'_-, MRS D'_0 [37] and the preliminary MRS H [38]) and the CTEQ collaboration [39]. The earlier sets such as HMRS B [40], MRS E' [41], KMRS B_0 [42] and MT B1 [43] tend to predict lower asymmetries, and most can be ruled out by this measurement. However, the earlier global fits did not have access to the recent DIS results from CCFR [44] and NMC [13], or the very recent *ep* collider data from Hera [45, 46]

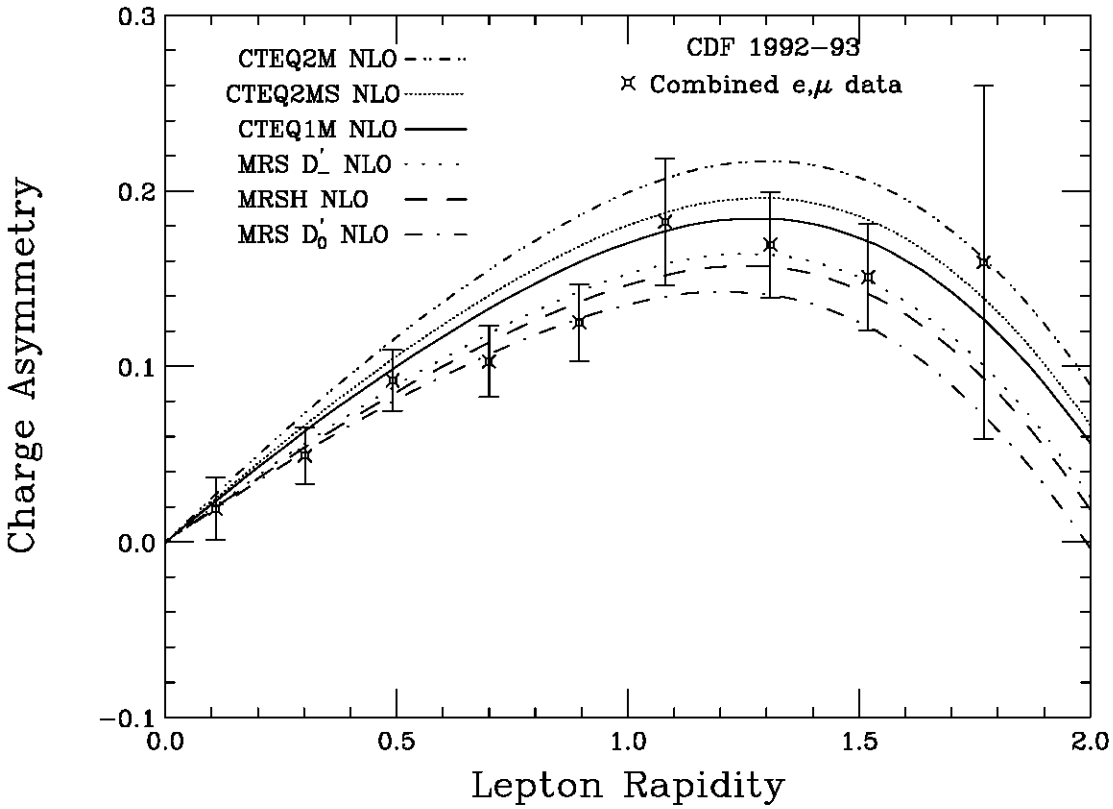

Figure 7.3: The charge asymmetry measured by CDF, compared to predictions of the latest PDF's. The data are fully corrected for trigger and backgrounds and the systematic errors are included.

(this data is at a very low $x \sim 10^{-4}$, so it only indirectly impacts the W charge asymmetry). As a result, most of these PDF sets have been declared obsolete and retracted by their authors.

The GRV NLO parton distributions [47] are in a class of their own. Rather than fitting the data directly, "valence-like" distributions at very low Q ($Q_0^2 = 0.3$ GeV^2) are evolved and then fitted to MRS distributions at a higher Q^2. The x and Q^2 dependencies are then determined by the renormalization group equations. This set of parton distributions has become of particular interest because they "predicted" the rise in the

F_2^{ep} structure function at $x \sim 10^{-4}$, and they fit the Hera data quite well. However, the GRV PDF's do not reproduce the observed W charge asymmetry (see Figure 7.2) very well.

Therefore it is of most interest to concentrate on the recent MRS and CTEQ fits. Both groups have had access to the same DIS data, but as Figure 7.3 shows, they differ considerably in their charge asymmetry predictions. To quantify the degree to which the various PDF's reproduce the data, Table 7.1 list the results of χ^2 tests of the goodness of fit. Because there is no differentiating power in the first and last η bins, the χ^2 is also calculated for the seven bins spanning $0.2 < |\eta| < 1.7$, and their weighted mean (the calculated asymmetries were weighted in the identical manner). The motivation for the last test is that the various predicted asymmetries tend to differ systematically from one another. All the modern PDF's predict essentially the same shape, just their overall magnitude differ.

As expected, almost all the older sets have poor χ^2's, though HMRS B is still marginally acceptable. Much more surprising is the inability of the CTEQ distributions to reproduce the observed charge asymmetry. The PDF set for which the CTEQ collaboration gets the lowest χ^2 when fitting the DIS data, CTEQ 2M, is ruled out by the asymmetry measurement. In contrast, the MRS distributions fit remarkably well; their latest, MRS H, reproduces the asymmetry perfectly. These two distributions are the result of fitting the same DIS data, including the Hera data, yet the asymmetry favors the MRS distributions and rules out CTEQ's. It is interesting to speculate on what causes the large differences between these two modern PDF sets.

PDF Set	$\lvert y\rvert < 2$ (9 dof) χ^2	$\mathcal{P}(\chi^2)$	$0.2 < \lvert y\rvert < 1.7$ (7 dof) χ^2	$\mathcal{P}(\chi^2)$	$\overline{A}(y)$ $0.2 < \lvert y\rvert < 1.7$ $\Delta\sigma$	$\mathcal{P}(\sigma^2)$
CTEQ 2M	24.63	0.003	24.37	0.001	4.56	0.000
CTEQ 2MS	11.02	0.274	10.84	0.146	2.94	0.003
CTEQ 2MF	16.99	0.049	16.77	0.019	3.76	0.000
CTEQ 2ML	14.94	0.093	14.70	0.040	3.51	0.000
CTEQ 1M	6.35	0.705	6.14	0.523	2.09	0.037
CTEQ 1MS	4.14	0.902	3.91	0.790	1.51	0.132
MT B1	18.54	0.029	16.77	0.019	-3.21	0.001
MRS H prelim.	2.22	0.988	1.76	0.972	-0.05	0.959
MRS D'_-	2.30	0.986	1.91	0.965	0.50	0.614
MRS D'_0	4.37	0.885	3.59	0.825	-0.94	0.349
HMRS B	5.12	0.824	4.23	0.753	-1.20	0.231
KMRS B_0	20.33	0.016	18.73	0.009	-3.59	0.000
MRS E'	32.15	0.000	30.46	0.000	-4.89	0.000
MRS B'	25.99	0.002	24.07	0.001	-4.10	0.000
GRV NLO	11.74	0.228	11.55	0.116	3.04	0.002

Table 7.1: The results of χ^2 comparisons between the predicted asymmetries (calculated at NLO) for several NLO PDF's including the most recent MRS and CTEQ distributions. The comparison of the weighted means ($\overline{A}(y)$) is sensitive to systematic shifts, and indicates the MRS H distributions fit the asymmetry data best.

7.3 Measuring the Proton Structure

The rapidity of the W's which contribute to each of the lepton η bins was determined using Dyrad. Of course this is very sensitive to the detector acceptances, which are not modelled perfectly. However, even the qualitative results are useful in the understanding of the relationship between the rapidity of the W and its decay lepton. Figure 7.4 shows the average rapidity of the W's which contribute to particular η_{lep} bin and the x values these rapidities correspond to. One sees that the lepton asymmetry carries much the same information as the W's.

As discussed in section 1.3, the W charge asymmetry is particularly sensitive to the slope of the $d(x)/u(x)$ ratio in the x range $0.007 - 0.27$ (see Figure 7.4), whereas the

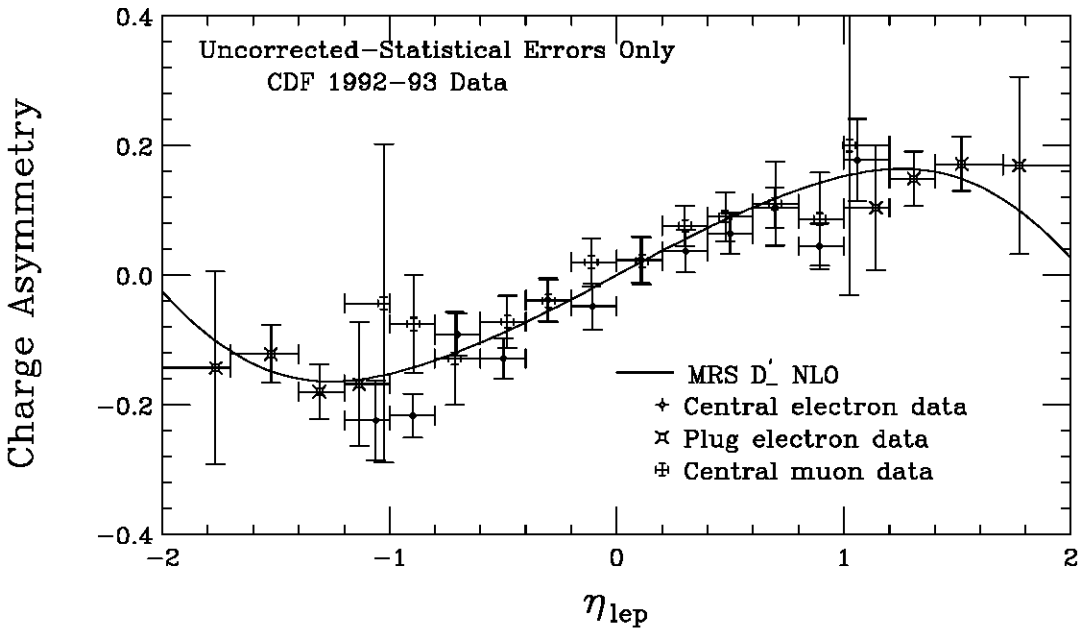

W^+<y>	~X_d	$-1.2^{0.15}$		$-0.6^{0.08}$		$.32^{0.03}$		$1.2^{0.01}$		$1.8^{0.007}$
	~X_u		$_{0.01}$		$_{0.02}$		$_{0.06}$		$_{0.15}$		$_{0.27}$
W^-<y>	~X_d	$-1.8^{0.007}$		$-1.2^{0.01}$		$-.32^{0.03}$		$0.6^{0.08}$		$1.2^{0.15}$
	~X_u		$_{0.27}$		$_{0.15}$		$_{0.06}$		$_{0.02}$		$_{0.01}$

Figure 7.4: The average W^+ and W^- rapidity and the corresponding x values of the u and d quarks are shown under the lepton η bin to which they contribute.

$F_2^{\mu n}/F_2^{\mu p}$ measurements are sensitive to the magnitude of this ratio. Recently NMC has measured $F_2^{\mu n}/F_2^{\mu p}$ [13] over an x range comparable to that accessible at CDF (though at a very different Q^2). Their data, both before and after correcting for shadowing effects [48, 14], are plotted in Figure 7.5 along with several NLO predictions [49]. Also shown are the d/u ratios after being shifted by a constant so they agree with MRS D_0' at $x = 0.2$. From the comparisons of the shifted ratios with the corresponding asymmetries (see Figure 7.2), we find that PDF's which predict the largest difference between the d/u ratio at small x and that at moderate x (i.e. the ones whose d/u ratio have the largest average slope over the x range 0.007-0.20), also predict largest charge asymmetries (as

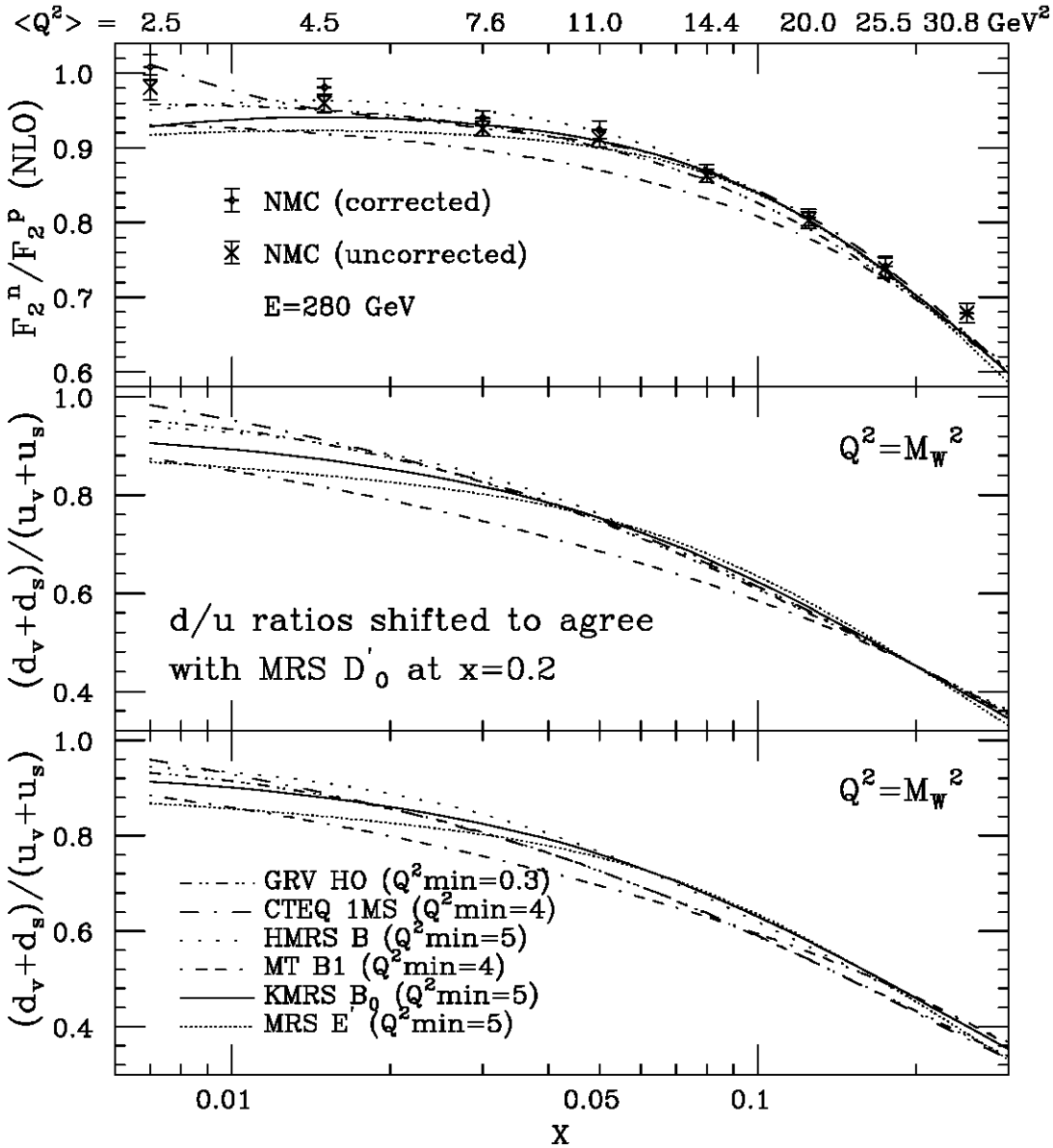

Figure 7.5: F_2^n/F_2^p derived from the NMC data, before and after correcting for shadowing in the deuteron [14] (top). The F_2^n/F_2^p predictions were done at NLO and take the different Q^2's at each data point into account. The predicted charge asymmetries for these PDF's can be found in Figure 7.2. Warning: For Q^2 values below the minimum Q^2 stated at the bottom of the figure, the parton distributions were logarithmically extrapolated.

anticipated by Equation 1.2).

Figure 7.6 compares only the latest fits performed by the MRS and CTEQ collaborations (see Appendix E). One sees that even though the MRS and CTEQ fits have very different d/u distributions (and thus very different charge asymmetry predictions) the $F_2^{\mu n}/F_2^{\mu p}$ predictions agree at the level of the shadowing corrections. This is because the $F_2^{\mu n}/F_2^{\mu p}$ ratio, which at LO is,

$$\frac{F_2^n}{F_2^p} = \frac{4d_v + u_v + 2(4\overline{d} + \overline{u}) + 4(c + \overline{c}) + (s + \overline{s})}{4u_v + d_v + 2(4\overline{u} + \overline{d}) + 4(c + \overline{c}) + (s + \overline{s})},$$

(c and s are the charm and strange distributions) is also sensitive to the differences in the $\overline{u}$ and $\overline{d}$ distributions, whereas the $A(y)$ asymmetry is not as sensitive. Thus the CTEQ's parameterization of the $\overline{u}$ and $\overline{d}$ sea distributions compensates for their steep d/u ratio and leads to a prediction for $F_2^{\mu n}/F_2^{\mu p}$ which is consistent with the NMC data but is inconsistent with our $A(y)$ asymmetry measurement.

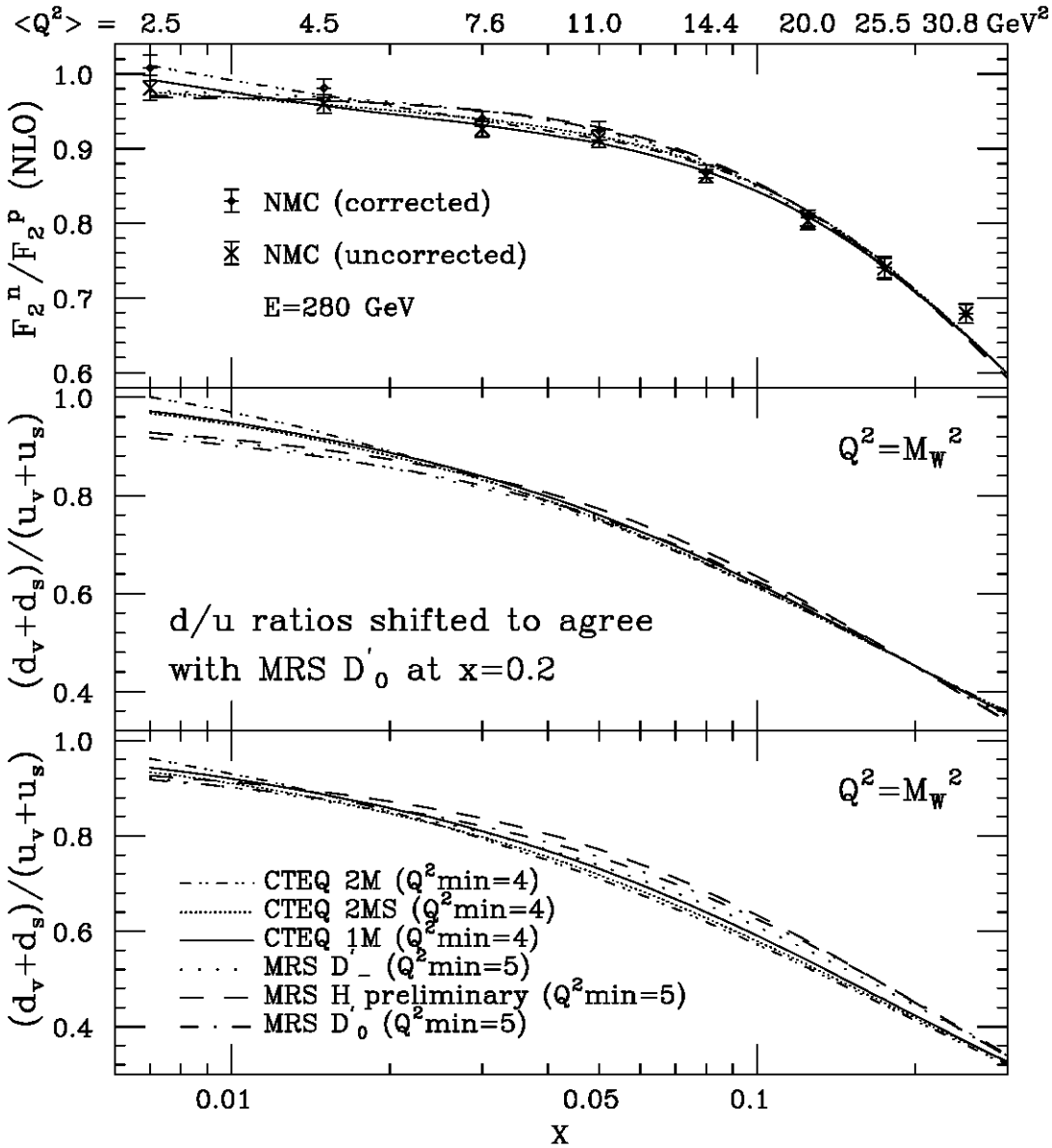

Figure 7.6: F_2^n/F_2^p for some of the most recent PDF's compared to the NMC data (as in Figure 7.5). The predicted charge asymmetries for these PDF's can be found in Figure 7.3. Warning: For Q^2 values below the minimum Q^2 stated at the bottom of the figure, the parton distributions were logarithmically extrapolated.

Chapter 8

Conclusions

The prior measurement of the charge asymmetry in W decays was severly hampered by statistics as well as detector problems, but even so, the measurement hinted that the predicted asymmetries were too low, thus implying that the d/u ratio was steeper than most parton distributions predicted. With the advent of recent high statistics, precision deep inelastic scattering experiments, the global fits to the proton structure all predict steeper d/u quark distributions. But as the x range probed in these experiments has decreased and the statistics increased, in the muon experiments on hydrogen and deuterium, the theoretical uncertainties in the extraction of the quark distributions due to higher twist effects, and shadowing corrections in the deuteron at low Q^2, have become very important. The fact that the charge asymmetry is able to distinguish between parton distributions which fit the NMC $F_2^{\mu n}/F_2^{\mu p}$ measurements, demonstrates that already its sensitivity to the d/u ratio at low x is approaching that of the muon scattering experiments.

The asymmetry data has also provided an independent means by which we can test

the series of assumptions about theory and experiment that go into a particular set of global fits to the proton's structure. It is evident that the CTEQ collaboration's approach of allowing all parton parameterizations to float does not produce the most accurate set of distributions. By imposing some constraints, the MRS collaboration has produced sets of parton distributions which not only provide a good fit to data in a Q^2 and x range of the DIS data to which they were fit, but also reproduce the CDF asymmetry data.

The systematic errors will remain negligible through the current run of the Tevatron and into the next. Even with four times the data (100 pb^{-1} of integrated luminosity) the W charge asymmetry's error will be dominated by the statistics available. In the future it is clear that the charge asymmetry will be able to play a much stronger role in the determination of the proton's structure.

Appendix A

False Curvature Corrections

Because of residual misalignment of the CTC wire positions there remained a "false curvature" which was added to the tracks. This effect was measured by studying the difference in E/P for positive and negative tracks. On average, the standard reconstruction code left no false curvature in the data, but as a function of η and ϕ there remained an effect which needed to be removed. The following equations were used to correct P_T and E/P:

$$\begin{aligned} P_T^{cor} &= P_T/(1 - charge * P_T * KdC(x)) \\ \left(\frac{E}{P}\right)^{cor} &= \frac{E}{P} * (1 - charge * P_T * KdC(x)) \\ KdC(x) &= \frac{1}{2\langle E_T \rangle} \Delta \langle E/P \rangle^{\pm}(x) \end{aligned} \tag{A.1}$$

where $\langle E_T \rangle = 34.5$ GeV, and $KdC(x)$ is a constant, $K = 1/(0.0000149898 * 14.116)$, times the false curvature, dC, which is a function of η and ϕ. The central electron data were used to determine the correction functions $KdC(\eta)$ and $KdC(\phi)$. Figure A.1

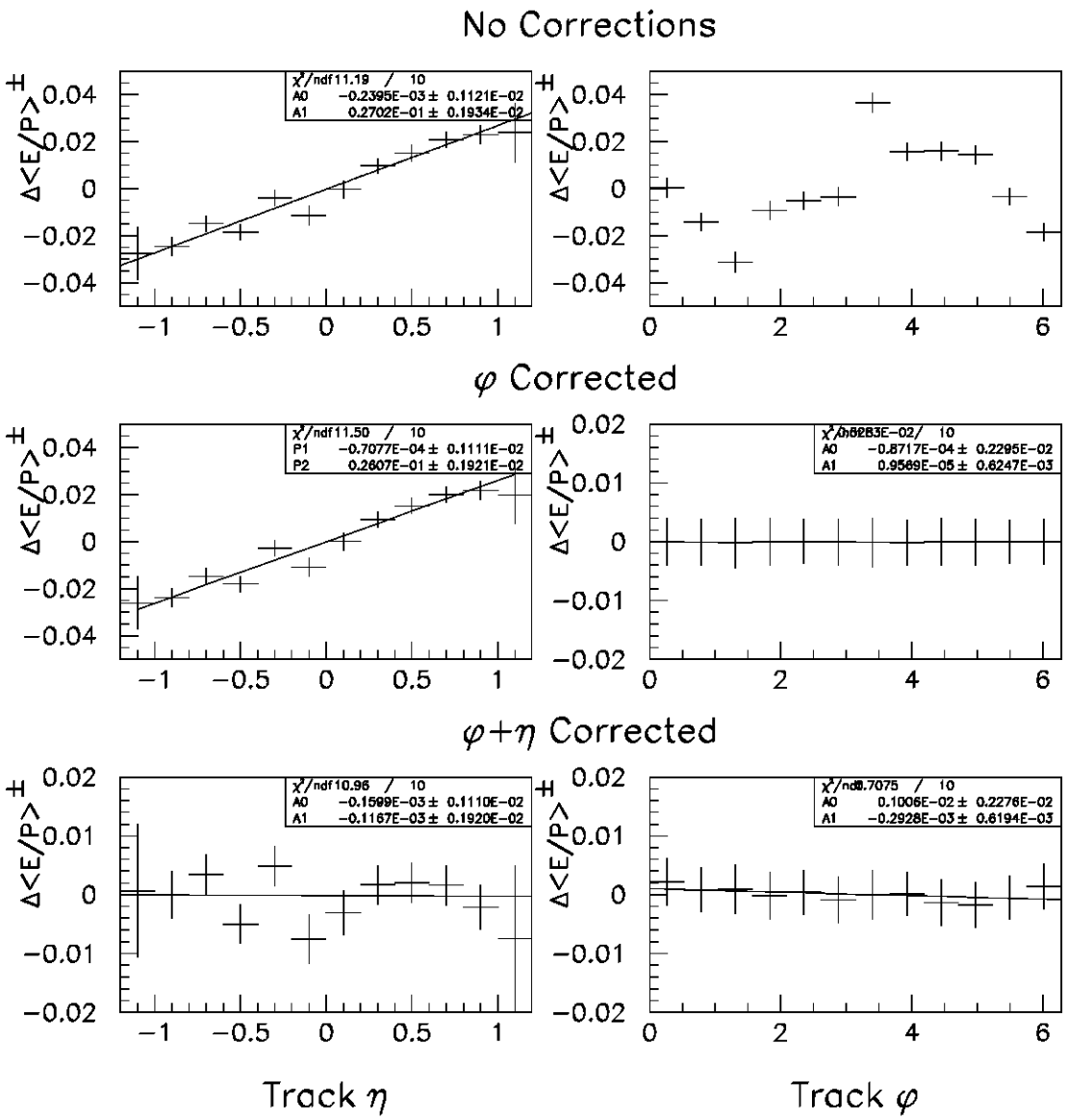

Figure A.1: The difference $\langle E/P^+\rangle - \langle E/P^-\rangle$, as a function of η and ϕ, is directly related to the false curvature introduced by the misalignment of the CTC wires. The figures show the false curvature before any corrections, after the ϕ and after $\phi + \eta$ dependent corrections.

ϕ°	$\Phi(\phi)$	ϕ°	$\Phi(\phi)$
0-30	0.0004	180-210	0.0365
30-60	-0.0142	210-240	0.0157
60-90	-0.0313	240-270	0.0160
90-120	-0.0092	270-300	0.0144
120-150	-0.0051	300-330	-0.0033
150-180	-0.0036	330-360	-0.0184

Table A.1: These coefficients were determined from the difference in the E/P distributions for central e^+ and e^-.

shows the false curvature as a function of η and ϕ before any corrections, after the ϕ dependent correction and after both ϕ and η dependent corrections. Comparing the η dependence of the false curvature before and after the ϕ dependent correction is applied clearly demonstrate that the two corrections are uncorrelated.

The ϕ dependent false curvature is most likely due to the CTC construction. Therefore no functional form was assumed and the correction was performed by a lookup table. The data was divided into 12 ϕ slices, because when the CTC was constructed it made use of 12 precision alignment holes spaced equally in ϕ. Table A.1 lists the coefficients for the following correction function,

$$K\,dC(\phi) = \frac{1}{2\langle E_T \rangle} \times \Phi(\phi),$$

which was used in the asymmetry analysis.

The η dependence is thought to be due to a twist in the CTC. This condition would explain the linear dependence seen in the data. The correction was performed using the

slope of the fitted line which gives:

$$KdC(\eta_{track}) = \frac{0.0261}{2\langle E_T \rangle} \times \eta_{track},$$

where η_{track} is the position (in detector η coordinates) of the track extrapolated to the central electromagnetic strip chambers (CES).

Appendix B

QCD Background Estimation

When defining the isolation region which is supposed to be free of signal, there is a large amount of arbitrariness. To try and rationalize the choice, the % background estimated (i.e. the fraction of the W candidates estimated to be QCD events) is plotted with respect to the isolation cut which defines the non-isolated region. It is expected that as this cut approaches that which defines the signal region, real W electrons will appear non-isolated, because the electron may radiate a photon, and will result in an overestimate of the QCD background. Because the plug isolation variable is weaker than the central (due to geometry), $2 \times Isolation(R = 0.4)$ is plotted for the plug and compared with the corresponding $Isolation$ distributions for the central in Figure B.1. From these plots it is evident that using a cut of $Isolation > 0.3$ in the central and $Isolation > 0.15$ in the plug regions yield a fairly stable result.

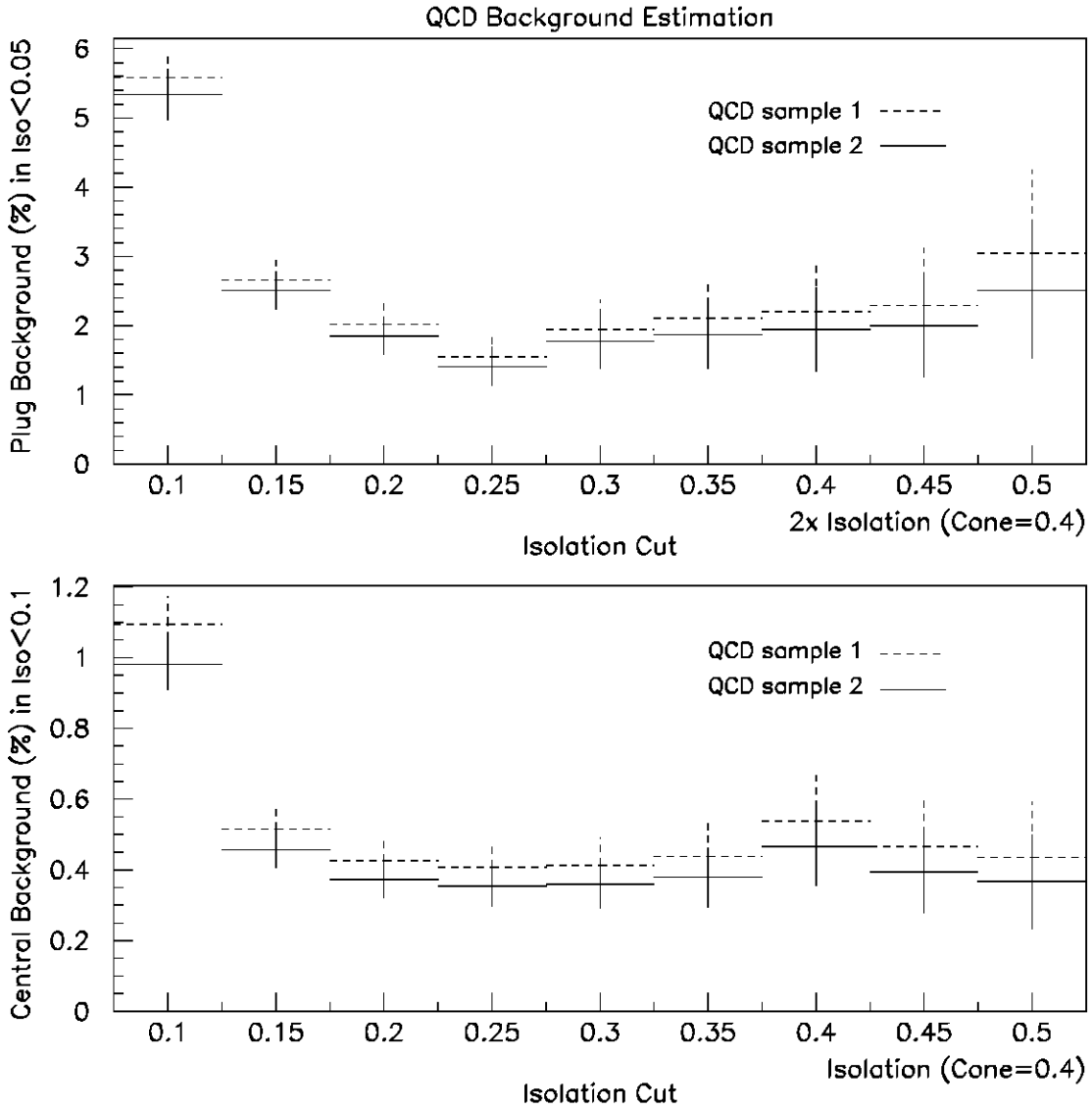

Figure B.1: The variation in the estimated QCD background (%) in the signal region (with $Isolation < 0.05$ in the plug and $Isolation < 0.1$ in the central) relative to the cut which defines the non-isolated region.

Appendix C

Plug Tracking Efficiency

It was necessary to know the tracking efficiency in the plug region in order to estimate the amount of background from losing one of the leptons from a Z decay. This is mainly of importance to the muon analysis because in the electron case the calorimeter usually identifies the electron. Even if the electron is misidentified as a jet, it will only result in $\not{E}_T$ if it strikes a calorimeter crack.

The efficiency was determined using the plug $W \rightarrow e\nu$ data set. In the asymmetry analysis, events containing a second track of P_T greater than 10 GeV are rejected. This cut defines what is meant by "tracking efficiency" as it relates to rejecting Z's. Because the W decay leptons have lower P_T than do the leptons from Z's, the P_T cut is lowered by a factor of $\approx M_W/M_Z$ to 9 GeV and varied by ± 2 GeV to determine how sensitive the efficiency estimation is to the exact value of the cut. Figure C.1 shows the fraction of plug W's which have a track of $P_T > 7, 9$ and 11 GeV associated with the calorimeter cluster. These events were selected with tight cuts on the jet energy (< 10 GeV) and the transverse mass $M_T^W > 60$ GeV in order to reduce backgrounds. The cuts were varied,

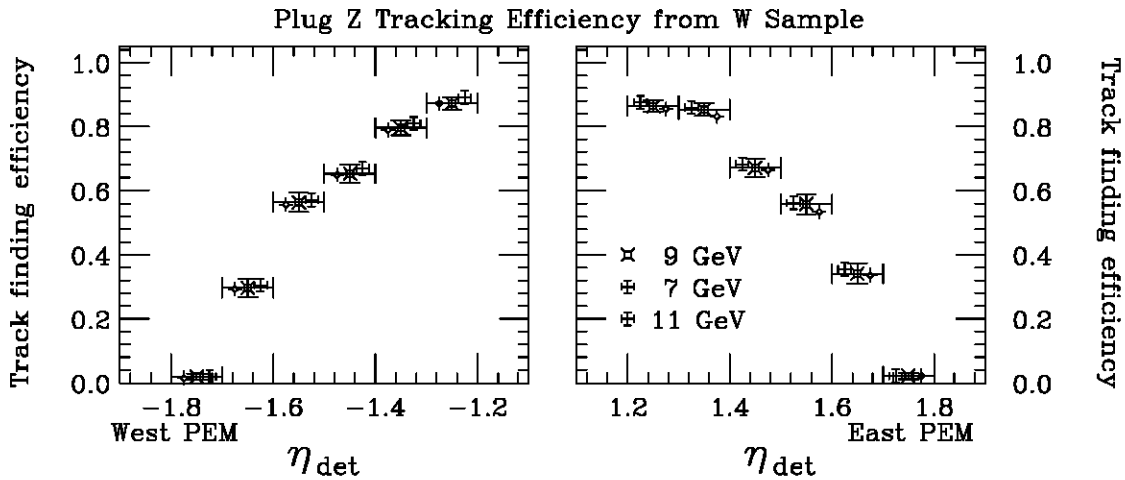

Figure C.1: The efficiency for identifying the second lepton from a Z decay as a function of detector η is determined using the plug W sample. The 10 GeV cut has been scaled to 9 GeV to account for the harder spectrum expected from Z decays. Efficiencies are shown for a 9 (nominal), 7 and 11 GeV P_T cut.

and no significant changes were seen in the efficiencies. The measured efficiencies are fairly independent of the exact value of the P_T cut as seen in Figure C.1. In the Z background estimates, both the size and the charge asymmetry will be calculated using the 9 GeV efficiency with a conservative error of $\pm 10\%$.

Appendix D

PEM Gas Gain Stability

In order to maintain a constant gas gain in the plug and forward calorimeters, the high voltage for each PEM quadrant was varied automatically in response to temperature and pressure changes. The 1992-93 run was the first time this "high-voltage feedback" technique was used.

As a check of the feedback system, Figure D.1 shows the average invariant mass of central-plug Z's as a function run number (i.e. time) and PEM quadrant. The $\langle Z\ Mass \rangle$ taken every 25 Z's (after the data was ordered by run number) shows that the high voltage feedback system maintained a constant gas gain at the 1% level, despite the variations in the temperature and pressure that invariably occurred throughout the year long run. The data from the gas gain tubes located inside the PEM also had a RMS of 1.2%, confirming that the feedback system had been successful. Also shown in Figure D.1 are the quadrant-to-quadrant variations in the Z mass. In the 1988-89 run this variation was as large as $\pm 10\%$. In the 1992-93 data (this sample) the new mapping corrections successfully removed these large variations.

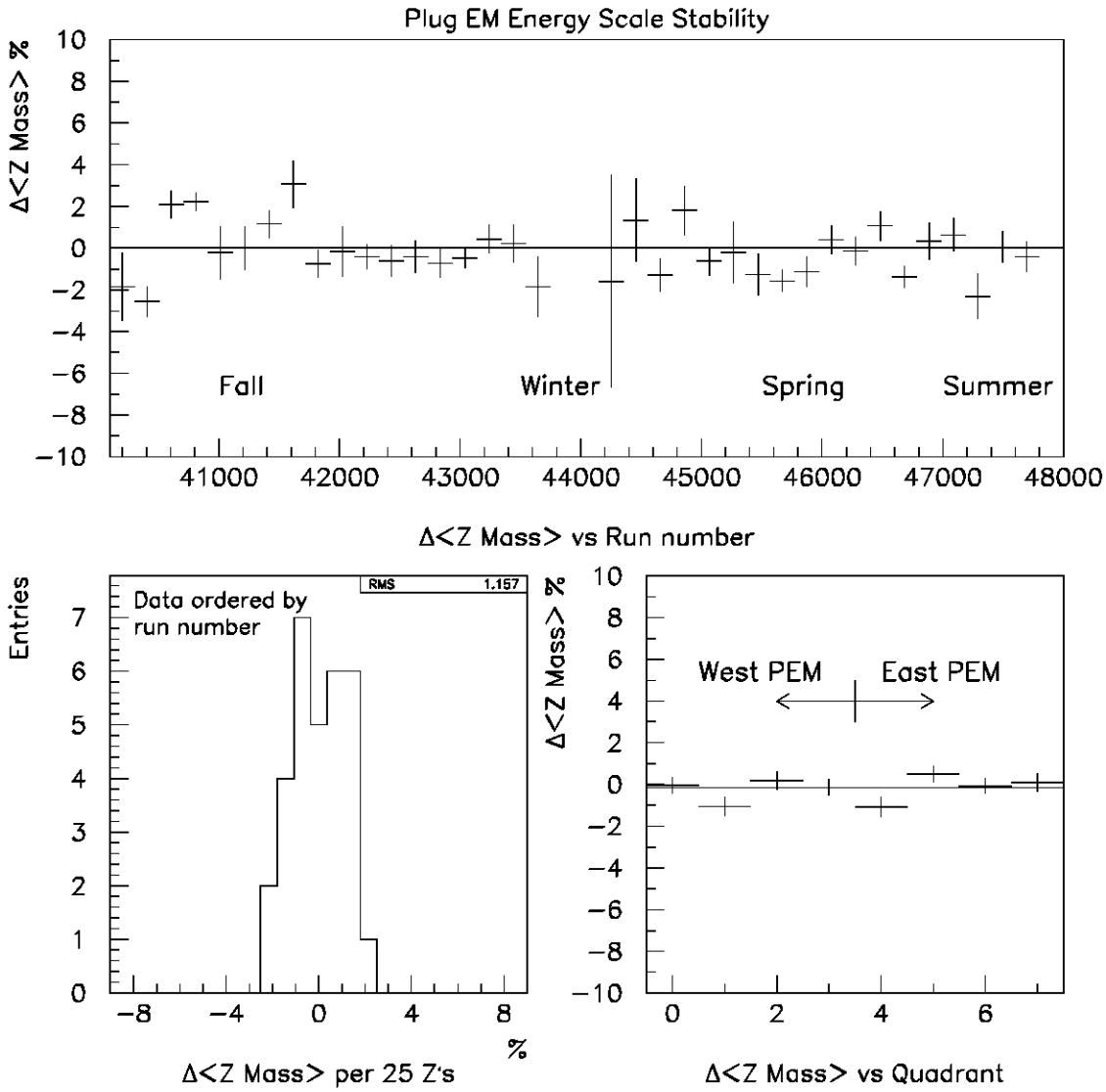

Figure D.1: The percent variation in the invariant mass of central-plug $Z \to ee$ events as a function of time, and PEM quadrant.

Appendix E

The CTEQ and MRS Distributions

The most recent sets of NLO parton distributions include the CTEQ [39] fits as well as the recent MRS fits (MRS D'_-, MRS D'_0 [37] and MRS H [38]). The primary difference between the two groups of fits are the assumptions under which they were performed. MRS tried to fit the data using a minimal set of parameters; extra parameters were included only when required by the data. The CTEQ collaboration chooses to minimize the theoretical bias by fitting all the favours to the same functional form simultaneously:

$$f(x, Q_0) = A_0 x^{A_1}(1-x)^{A_2}(1 + A_3 x^{A_4}),$$

subject to minimal restrictions in addition to the quark-number and momentum sum rules.

The following plots show the distributions of the valence u and d quarks (u_v and

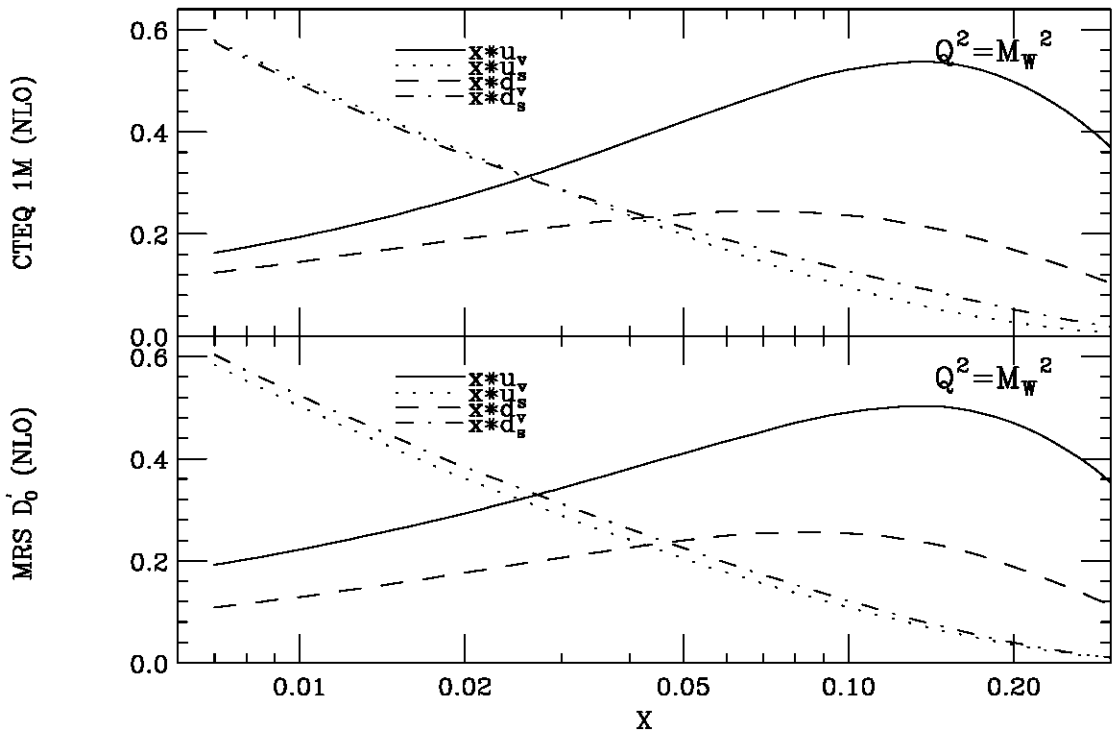

Figure E.1: Parton distributions MRS D_0' (bottom) and CTEQ 1M (top). Both MRS D_0' and CTEQ 1M were fitted before the Hera data was available and thus have non-singular gluon distributions. This CTEQ distribution was found to disagree with the CCFR dimuon measurement, which gives s(x), in addition to the W charge asymmetry. Both sets fail to fit the Hera data.

d_v) at $Q^2 = M_W^2$ for the x range which contributes to W production at the Tevatron.

Also shown are the "sea" contributions to the u and d quark distributions.

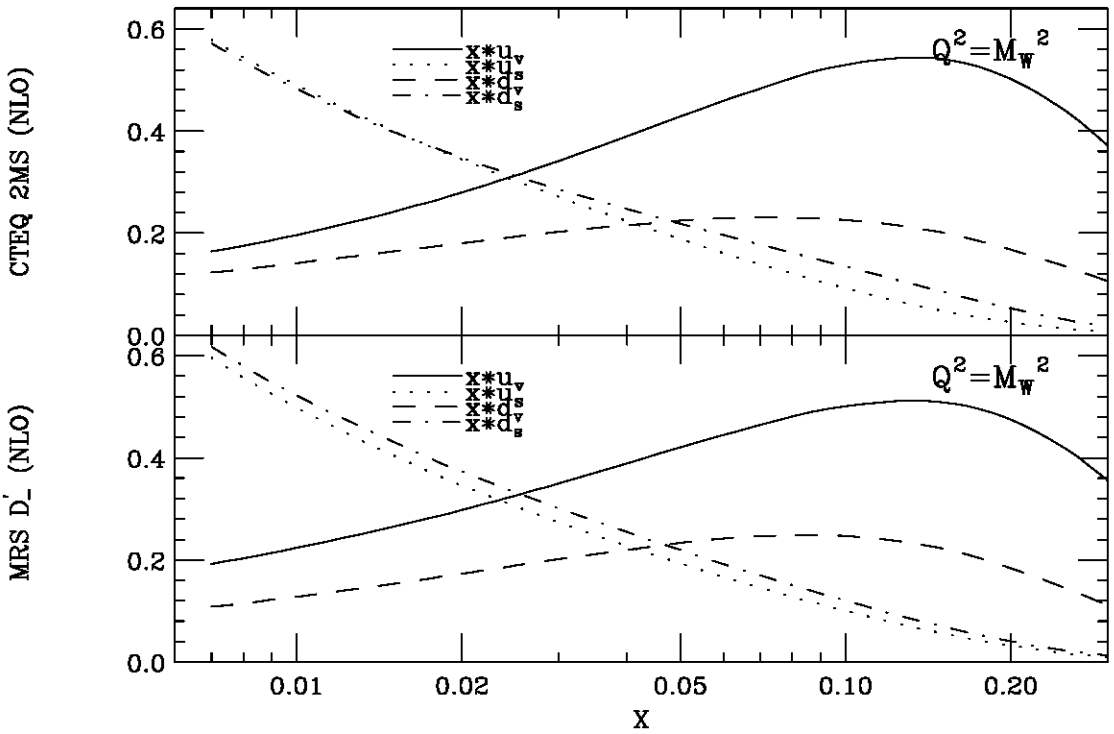

Figure E.2: Parton distributions MRS D′_ (bottom) and CTEQ 2MS (top). These distributions both have singular gluon distributions, though somewhat steeper than would be indicated by the Hera data. Again the MRS distribution is found to fit the asymmetry data better.

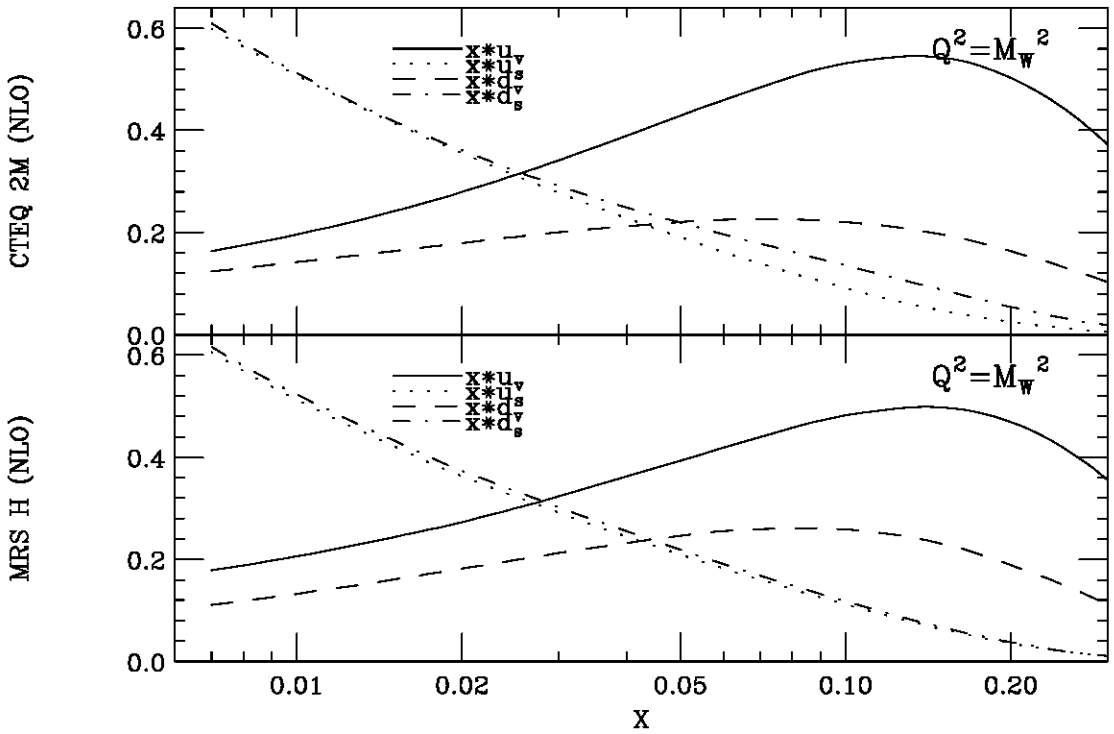

Figure E.3: Parton distributions MRS H (bottom) and CTEQ 2M (top). These two sets fit all the presently available DIS and Hera data equally well. However the W charge asymmetry strongly prefers the MRS fit over the CTEQ fit whose d/u ratio is much steeper (in the relevant x range).

Bibliography

[1] M. Gell-Mann, Phys. Rev. Lett. **8**, 214 (1964).

[2] G. Zweig, CERN Report 8419TH, 412 (1964).

[3] J. Lefrancois, in *Proc. Int. EPS Conf. on High Energy Physics*, Marseille 1993. The number of light neutrinos, $N_\nu = 2.980 \pm 0.027$ from the LEP experiments.

[4] H. Fritzsch and M. Gell-Mann, *Proc. 16th Int. Conf. High Energy Physics, Chicago, Vol. 2, p. 135, Batavia, Ill., Fermi Nat. Accel. Lab*, (1972).

[5] H. Fritzsch, M. Gell-Mann and H. Leutwyler, Phys. Lett. **47**, 365 (1973).

[6] Weinberg, S., Phys. Rev. Lett. **31**, 494 (1973).

[7] Gross, G.J. and Wilczek, F., Phys. Rev. Lett. **30**, 1343 (1973); Phys. Rev. **D8**, 3663; Phys. Rev. **D9**, 980 (1974).

[8] Glashow, S. L., Nucl. Phys. **22**, 579 (1961).

[9] Weinberg, S., Phys. Rev. Lett. **19**, 1264 (1967).

[10] Salam, A., Nobel Symposium #8, edited by W. Svartholm (1968).

[11] O. W. Greenberg, Phys. Rev. Lett. **13**, 598 (1964).

[12] J. Kuber, M. Le Bellac, J. L. Meunier and G. Plant, Nucl. Phys. **B175**, 251 (1980); G. Altarelli, R. K. Ellis, M. Greco and G. Martinelli, *ibid.* **B246**, 12 (1984).

[13] NMC Collaboration, P. Amaudruz *et al.*, Phys. Lett. **295B**, 159 (1992).

[14] B. Badelek, J. Kwiecinski, Nucl. Phys. **B370**, 278 (1992).

[15] A. D. Martin, R. G. Roberts and W. J. Stirling, Mod. Phys. Lett. **A4**, 1135 (1989).

[16] E. L. Berger, F. Halzen, C. S. Kim and S. Willenbrock, Phys. Rev. **D40**, 83 (1989).

[17] K. Gottfried, Phys. Rev. Lett. **18**, 1174 (1967).

[18] NMC Collaboration, P. Amaudruz *et al.*, Phys. Rev. Lett. **66**, 2712 (1991).

[19] TRIUMF Collaboration, B. Blake *et al.,* Phys. Rev. **D37**, 587 (1988).

[20] UA1 Collaboration, Phys. Lett. **166B**, 484 (1986); **185B**, 233 (1987).

[21] W.T. Giele, E.W.N. Glover, D.A. Kosower, Higher Order Corrections to Jet Cross Sections in Hadron Colliders, Fermilab-Pub-92/230-T (1992).

[22] Particle Data Group, Phys. Rev. **D45**, VI.16 (1992).

[23] For a detailed description, see F. Abe *et al.*, Nucl. Instrum. Methods Phys. Res., Sect. A **271**, 387 (1988), and references therein.

[24] K. Yasuoka, S. Mikamo, T. Kamon and A. Yamashita, Nucl. Instr. and Meth. **A267**, 315 (1988).

[25] D. Saltzberg, CDF NOTE #2085 (1993).

[26] The Working Group on LEP Energy and The LEP Collaborations, Phys. Lett. **307B**, 187 (1993).

[27] Kevin Einsweiler and Young-Kee Kim, private communication. The CDF implementation of the UA2 LO W/Z Radiative Monte Carlo.

[28] G. Marchesini and B. R. Webber, Nucl. Phys. **B310**, 461 (1988).

[29] F. Abe *et al.*, Phys. Rev. Lett. submitted February (1994).

[30] F. Abe *et al.*, Phys. Rev. Lett. **68**, 1458 (1992).

[31] M. Dickson, the Gas Calorimetry Group, CDF NOTE #1777 (1992).

[32] M. Dickson, CDF NOTE #2468 (1994).

[33] R. Keup, CDF NOTE #2262 (1993).

[34] Particle Data Group, Phys. Rev. **D45** (1992).

[35] M. Krasberg and T. LeCompte, CDF Note #2032 (1993).

[36] A. Byon-Wagner *et al.*, CDF Note #1260 (1990).

[37] A.D. Martin, R.G. Roberts and W.J. Stirling, RAL-92-021 (1992).

[38] A.D. Martin, R.G. Roberts and W.J. Stirling, RAL-93-077 (1993).

[39] J. Botts, J.G. Morfin, J.F. Owens, J. Qiu, W.K. Tung and H. Weerts, Phys. Lett. **304B**, 159 (1993).

[40] A.D. Martin, R.G. Roberts and W.J. Stirling, Phys, Rev. **D42**, 798 (1990).

[41] A.D. Martin, R.G. Roberts and W.J. Stirling, Phys. Lett. **206B**, 327 (1988).

[42] J. Kwiecinski, A.D. Martin, R.G. Roberts and W.J. Stirling, Phys. Rev. **D42**, 3645 (1990).

[43] Jorge G. Morfin and Wu-Ki Tung, Fermilab-Pub-90/74 (1990).

[44] CCFR collaboration: Phys. Rev. Lett., to be published.

[45] H1 collaboration: I. Abt *et al.,* preprint DESY-93-117 (August 1993).

[46] Zeus collaboration: M. Derrick *et al.,* preprint DESY-93-110 (August 1993).

[47] M. Glück, E. Reya and A. Vogt, Z. Phys. **C48**, 471 (1990), **C53**, 127 (1992); Phys. Lett. **B306**, 391 (1993).

[48] A.D. Martin, R.G. Roberts and W.J. Stirling, Phys. Lett. **B306**, 146 figure 2 (1993).

[49] W.J. Stirling, private communication. Code provided to calculate F_2 for distributions defined in the $\overline{MS}$ scheme.